(On the Spine)

DESIGN, MODELING AND CONTROL OF AN XYZ FLEXURE PARALLEL MECHANISM WITH LARGE MOTION RANGE AND DECOUPLED KINEMATIC STRUCTURE

TANG XUEYAN

2008

NANYANG TECHNOLOGICAL UNIVERSITY

DESIGN, MODELING AND CONTROL OF AN XYZ FLEXURE PARALLEL MECHANISM WITH LARGE MOTION RANGE AND DECOUPLED KINEMATIC STRUCTURE

TANG XUEYAN

SCHOOL OF MECHANICAL AND AEROSPACE ENGINEERING

2008

Design, Modeling and Control of an XYZ Flexure Parallel Mechanism with Large Motion Range and Decoupled Kinematic Structure

Tang Xueyan

School of Mechanical and Aerospace Engineering

A thesis submitted to the Nanyang Technological University
in fulfilment of the requirement for the degree of
Doctor of Philosophy

2008

Abstract

With the advantages of no backlash, no accumulative error and compatibility with vacuum and clean environment, flexure parallel mechanisms (FPMs) have been employed in high-precision positioning systems in optics, micro/nano scale metrology and manufacturing, semiconductor production and biology applications. This thesis focuses on the study of *XYZ*-FPMs with decoupled kinematic structure, large motion range and high positioning precision. A new type of prismatic joint is designed, with the advantages of having a large motion range, no parasitic motion, no stiffening, no buckling and a symmetric structure. An exact modeling method of the large-motion prismatic joints is proposed for the stiffness and dynamic models. Structure synthesis of *XYZ*-FPMs with large motion range and decoupled kinematic structure is studied. Different from the structure synthesis of rigid-body mechanisms, the possible configurations are proposed based on the Screw Theory, with the consideration of limitations and characteristics inherent in flexure mechanisms. In flexure mechanisms, the critical static performances include stiffness, workspace, stage size and parasitic motion. The stiffness models of these synthesized structures are formulated. The definition of motion range is proposed based on the workspace and the stage size. A dimension optimization approach based on these static performances is generalized. Based on these generalized study of flexure mechanisms, a 3-PPP *XYZ*-FPM with large motion range and decoupled kinematic structure is developed, covering structure design, dimension optimization, exact modeling and robust control. The experimental results show that the 3-PPP *XYZ*-FPM has a large workspace of $2.3mm \times 2.3mm \times 2.3mm$ and a large motion range of 7%. The decoupled kinematic structure is verified, with the maximum cross-axis error of 2% and the maximum parasitic rotation of $1.5mrad$. The hybrid position and vibration control algorithm using the H_∞-theory solves three common problems of flexure mechanisms, i.e., unmodeled uncertainties due to the difficulty of exact modeling of high-order mode shapes, high sensitivity to the external disturbances, and vibration caused by inherent

low damping. Using the designed controller and verified by the experiments, the positioning precision of $0.1\mu m$ is achieved, and the settling time is shortened to $0.1s$ after vibration suppression.

Acknowledgement

I am very grateful to my advisor, Professor Chen I-Ming, for his continuous interest, intellectual guidance, unlimited patience and constant encouragement during this research. His creative vision and broad knowledge play an important part in the fulfillment of this work. I also would like to give my sincere appreciation to my past advisor, Professor Li Qing, for her generous advice to my research and strong spiritual support.

Deepest gratitude is expressed to my parents who are constantly giving me their unconditional love and care.

I would like to thank Prof. Yeo Song Huat and Prof. Zhong Zhaowei, for their valuable comments during my confirmation examination.

I would like to thank my senior, Dr. Yang Guilin, for his constructive advice given to me. Dr Yang is always there to give me a helping hand and share with me his ideas in problem solving. I would also like to thank Prof. Gerald Seet, Mr. Lim Eng Cheng, Ms. Agnes Tan, Mr. Yow Kim San and Ms. Toh Yen Mei for providing me an excellent research environment at the Robotics Research Center (RRC). In addition, I would like to extend my gratitude to my friends, namely Dr. Chen Weihai, Dr. Theingi, Dr. Pham Huy Hoang, Dr. Lim Chee Kian, Dr. Yan Liang, Dr. Jin Yan, Dr. Pham Cong Bang, Dr. Mustafa Shabbir Kurbanhusen, Mr. Teo Tat Joo Daniel, Dr. Wang Xin, Dr. Wang Pin, etc.

Lastly, I would also like to acknowledge the financial support that I have received during the research from Nanyang Technological University. This project is partially supported by Ministry of Education, Singapore, under ARC project RG6/02.

Table of Contents

List of Figures

List of Tables

List of Symbols and Abbreviations

PRB	Pseudo-rigid-body
PPP	Prismatic-prismatic-prismatic
DOF	Degree of freedom
FPM	Flexure parallel mechanism
P	Prismatic
R	Revolute
U	Universal
S	Spherical
VCA	Voice coil actuator
PZT	Piezoelectric
EDM	Electric discharge machining
FEM	Finite element method

Chapter 1

Introduction

1.1 Motivation

As defined in Salamon [4] and Howell [5], a compliant mechanism is one which gains all or part of its mobility from the relative flexibility of its members unlike as in rigid-body mechanisms. The Webster's definition of the word "compliant" is "ready or disposed to comply: submissive". It is for this reason that the usage of "compliant mechanism" to refer to this class of mechanisms is deemed as appropriate [6]. Compliant mechanisms are desirable because, as noted by Her [7] and Sevak and McLarnan [8], they require fewer parts and have less wear, noise, and backlash than their rigid-body counterparts. Her and Midha [9] add that the field of compliant mechanisms will continue to grow as stronger and more resilient materials are developed. Since compliant mechanisms utilize their flexure hinges, in some studies, compliant mechanisms are also called flexure mechanisms [10] [11].

Studies and invasive surgeries of cells and tiny biological tissue are important for research in biology, physiology and biomechanics. They are critical to the health and functions of tissues and organs of the body. Therefore, the micro-instruments with high precision are needed. Flexure mechanisms with the advantages of no backlash, no accumulative error and high precision, provide a good solution. The Center of Research in Microengineering leaded by Menciassi [12] has designed a microgripper (shown in Fig. 1.1(b)), and applied it in microsurgery of microtubes (shown in Fig. 1.1(a)).

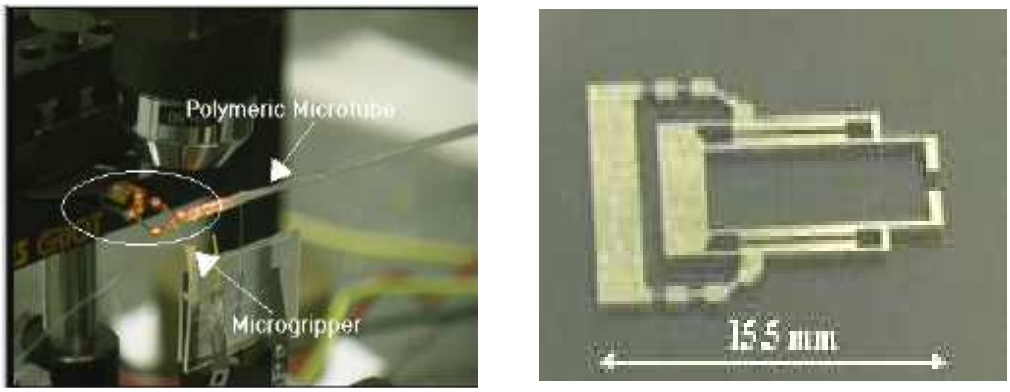

(a) Microsurgery under microscope (b) Flexure-based microgripper

Figure 1.1: Flexure mechanisms' application to microsurgery

Micro-manipulators have also been increasingly important in silicon cutting, wire bounding and chip assembly in the semiconductor industry. The positioning precision of flexure mechanisms can reach nano-scale, and they have been extensively utilized. The nano-scale cutting machine for silicon wafer has been worked out by Furutani [13] (shown in Fig. 1.2).

In the space operations, the gravity is approximately zero, which makes lubrication of devices impossible. Flexure mechanisms with the advantage of no need of lubrication can be extensively used in the field of aerospace. The Swiss Center for Electronics and Microtechnology (CSEM) [14] applied flexure mechanisms to the space meteorological interferometer (shown in Fig. 1.3).

Flexure mechanisms can also be applied to optical fiber alignment. The coaxial degree error of two connected optical fiber components affects the power transmission through the optical fiber. Usually, the requirement of the coaxial degree for a single-mode optical fiber is higher than $0.5\mu m$. Optics for Research (OFR) [15] has used flexure-based fine-tuning stage (shown in Fig. 1.4(b)) to mount the splitters.

Prompted by applications in micromanipulation, studies on high-precision flexure-based micromanipulators have been important. Development of the flexure-based micromanipulator covers mechanism design, modeling and control. However, there are several problems in the current research of flexure mechanisms, in the aspects of mechanism design, modeling and control.

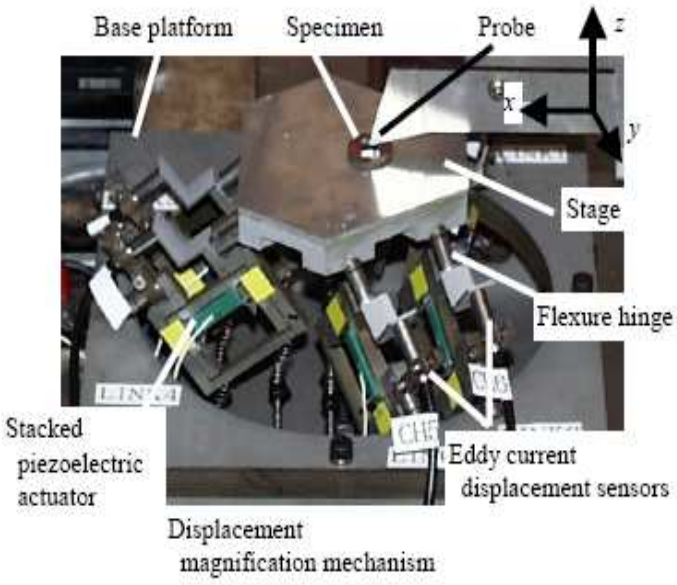

Figure 1.2: Flexure mechanisms' application to nano cutting machine

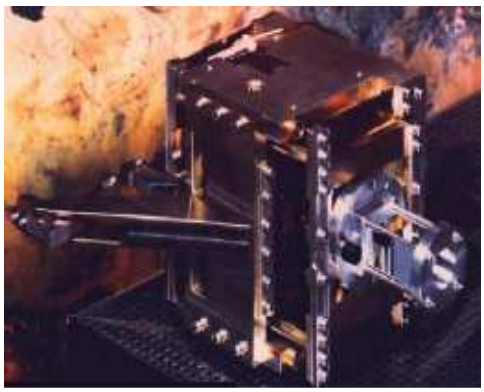

(a) Corner cube mechanism (CCM) for a space meteorological interferometer

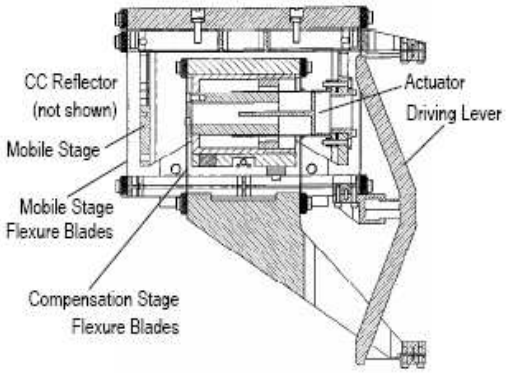

(b) Cross section of CCM

Figure 1.3: Flexure mechanisms' application to aerospace

(a) A walk-off polarizer application

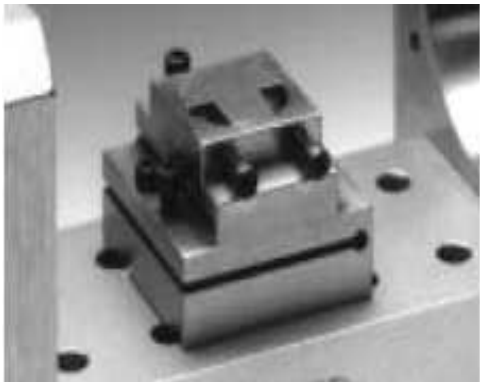

(b) Flexure-based 3-axis aiming base

Figure 1.4: Flexure mechanisms' application to optical fiber alignment

In the aspect of mechanism design, there are two problems. The first problem is the limited workspace. Most of the current 6-degree-of-freedom (DOF) and low-mobility flexure mechanisms have the limited workspaces in the scale of or below $100\mu m \times 100\mu m \times 100\mu m$. In some micro/nano-manipulations, such workspaces can meet the requirements, such as cell surgery, MEMS assembly, etc. However, in other micromanipulations, larger workspace is required, such as microscope, optical alignment, etc. The workspace near and more than $1mm$ is regarded to be large in the micromanipulation. The conventional rigid-body manipulator cannot achieve both the workspace in the scale of millimeter and the precision in the scale of submicronmeter. Thus, flexure mechanisms with large workspace in the scale of millimeter become important in the view of both research and practical applications. The second problem is the coupled kinematic structure. Most of the current multi-DOF flexure mechanisms possess the coupled kinematic structures. In high-precision flexure mechanisms, the coupled kinematic structure had better be avoided. It is because that it is difficult to exactly formulate multi-dimensional deformations of flexible components, and the errors due to coupling are not easy to be compensated. Study on flexure mechanisms with fully decoupled kinematic structures is critical to ensure the expected high positioning precision. Moreover, among the current decoupled *XYZ* flexure mechanisms, mechanism design is on case-by-case basis. Thus, the systematic study on decoupled *XYZ* flexure mechanisms becomes necessary.

In the aspect of modeling, exact modeling methods for flexure hinges have been formulated by Lobontiu [16], as well as an approximate modeling approach, pseudo-rigid-body (PRB) method [17], for flexure mechanisms. However, there is no exact modeling method for both statics and dynamics of complete flexure mechanisms.

In the aspect of control of flexure mechanisms, there are three problems needed to be solved, i.e., unmodeled uncertainties caused by modeling difficulty and omission of high-order mode shapes, vibration due to inherent low damping of flexure mechanisms, and high sensitivity to external disturbances. High positioning precision and fast dynamic response can be ensured simultaneously, if the above three problems are solved in one designed controller. The conventional and the current advanced control algorithms concentrate on either position control or vibration control of flexure mechanisms.

Thus, the hybrid controller with both position control and vibration control for flexure mechanisms becomes necessary.

1.2 Objective and Scope of Research

Inspired by the practical application and the research necessity, the study of *XYZ*-flexure parallel mechanisms (FPMs) with large motion range and decoupled kinematic structure becomes critical. The main issues in this research are illustrated in Fig. 1.5.

Structure synthesis

Low-mobility flexure mechanisms with decoupled kinematic structures have the advantages over multi-DOF and coupled flexure mechanisms, with the consideration of high precision. The current studies of decoupled *XYZ*-FPMs are based on the case by case. In this research, the configurations of decoupled *XYZ*-FPMs are synthesized, and the limitations common in flexure mechanisms are investigated. Simultaneously, the feature of large motion range is also what we are concerned. The large motion range is given a quantitative definition, balanced between the workspace and the stage size. A new type of prismatic joint with large motion range is designed and evaluated by the given definition. Applying the new type of prismatic joint, the synthesized *XYZ*-FPMs can achieve large motion range.

Dimension optimization

In flexure mechanisms, the static performances are critical. Many studies of optimal design aim at obtaining the satisfactory static performances. The main static performances can be summarized as stiffness, workspace, stage size and parasitic motion. These four parameters are all determined by or related to the dimensions of flexure mechanisms. The current studies of dimension optimization do not consider all of the static performances. Thus, the dimension optimization method considering all of these static performances is generalized, and the relationships of these four parameters are stated by the several given definitions in this research.

Exact modeling

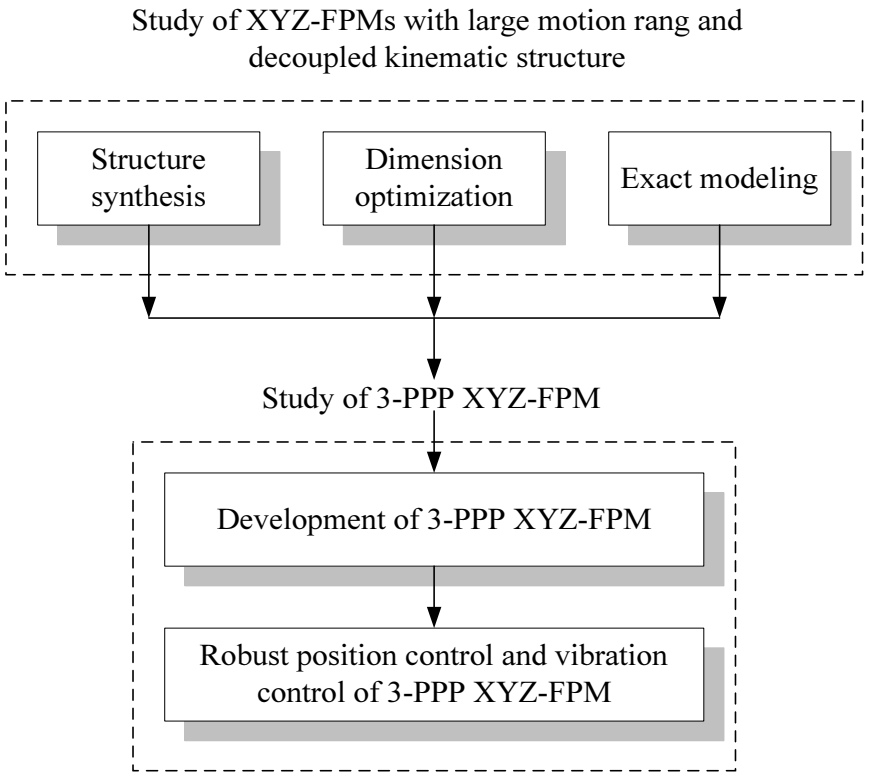

Figure 1.5: Main issues in this research

PRB method is a quick and approximate solution of modeling for derivation of stiffness and dynamics. It is quite convenient in design stage, such as used in dimension optimization for obtaining the optimal dimension values by giving a simplified formulation describing the target performance. However, PRB is not accurate enough for control usage. More accurate the analytical dynamic equation, higher precision the closed-loop system. The current exact compliance formulations only consider flexible hinges, not complete flexible structures, and are not yet easy to be applied to dynamics modeling. In this research, an exact modeling method is formulated for both static and dynamic analyses of the *XYZ*-FPMs.

Development of 3-PPP *XYZ*-FPM

Based on the systematic studies of *XYZ*-FPMs, i.e., structure synthesis, dimension optimization and exact modeling, a 3-prismatic-prismatic-prismatic (PPP) *XYZ*-FPM is designed, modeled and fabricated. The 3-PPP *XYZ*-FPM has the advantages of large motion range, decoupled kinematic structure and small parasitic motion. The mechanism design, optimal design and exact modeling are verified by the experimental results of the

3-PPP *XYZ*-FPM.

Hybrid position and vibration control with high robustness

The three common problems in flexure mechanisms, unmodeled uncertainties, sensitivity of external disturbances and small damping, deteriorate the positioning precision and fast response. They are expected to be solved simultaneously in one controller. The current controllers solve either position control or vibration control. In this research, the hybrid controller is designed, with position control to ensure the tracking performance and vibration control to suppress oscillation. In the meanwhile, high robustness of the controller is achieved. The hybrid controller with robustness solves the above three common problems, and is implemented in the developed 3-PPP *XYZ*-FPM.

1.3 Overview of Chapters

The remaining chapters of this thesis are organized as follows.

- Chapter 2 reviews some previous studies in the areas of structure design, modeling method and control algorithm.
- Chapter 3 addresses structure synthesis of the large-displacement and decoupled *XYZ*-FPMs. Moreover, the fundamental components of large-motion prismatic joints are investigated, and a new type is designed.
- Chapter 4 formulates the stiffness models of the synthesized *XYZ*-FPMs in Chapter 3. An exact modeling method for the designed large-motion prismatic joint is proposed for both static and dynamic analyses.
- Chapter 5 proposes a generalized dimension optimization approach based on the static performances of flexure mechanisms. The structure design of a 3-PPP *XYZ*-FPM with large motion range and decoupled kinematic structure is conducted. Dimensions of the 3-PPP *XYZ*-FPM are determined using this approach. The exact model of the 3-PPP *XYZ*-FPM is also formulated using the exact modeling method proposed in Chapter 4.

- Chapter 6 discusses the prototype of the 3-PPP *XYZ*-FPM and the experiments. The experimental results show that the proposed 3-PPP *XYZ*-FPM is large-motion and decoupled, and the nonlinear modeling method is more accurate than the PRB method.

- Chapter 7 presents design and implementation of the robust control algorithm to achieve a high positioning precision of $0.1\mu m$ and less vibration.

- Chapter 8 addresses conclusions, contributions and future works.

Chapter 2

Literature Review

This chapter surveys the current research on the flexure-based micromanipulators, in terms of mechanism design, modeling and control. The necessity of this research work is also elaborated.

2.1 Flexure Hinge

In rigid-body mechanisms, the desired motions at the end-effector are achieved by function of assembled prismatic (P) joints, revolute (R) joints, universal (U) joints and spherical (S) joints. As the counterparts of these joints in rigid-body mechanisms, flexure hinges are most flexible components in flexure mechanisms, and motions of flexure mechanisms can be achieved mainly through deformations of flexure hinges. In flexure mechanisms, single- and multi-axis flexure hinges can function as revolute joints and spherical joints, however, there are no flexure hinges that can be directly used as prismatic joints. Prismatic joints are achieved utilizing the parallelogram structures, which will be introduced Section 2.2.

2.1.1 Single-Axis Flexure Hinge

Leaf springs are earliest studied and applied among flexure hinges. Leaf springs under different loads and different constraints are studied by Smith [18]. Its sensitive axis is

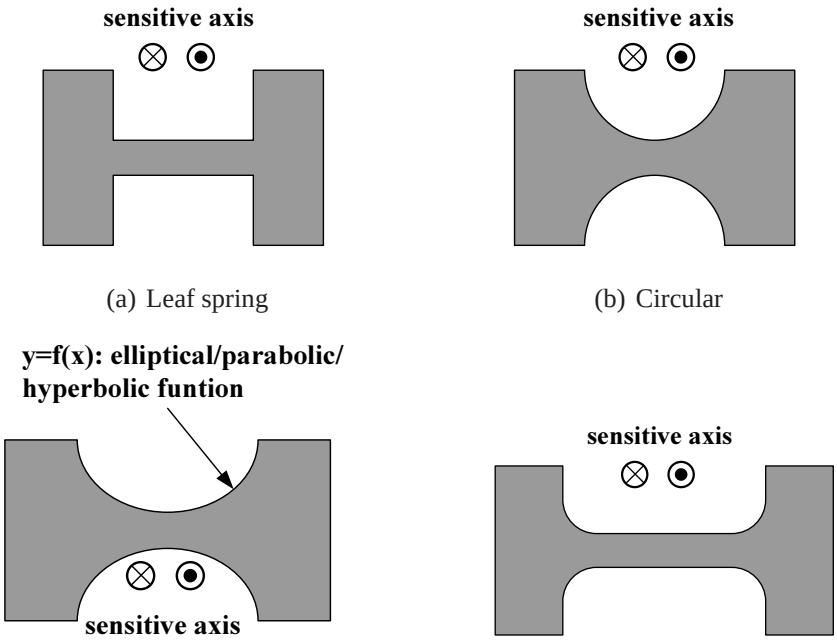

(a) Leaf spring (b) Circular

(c) Conic (d) Corner-filleted

Figure 2.1: Single-axis flexure hinges

perpendicular to the plane in Fig. 2.1, and its sensitive motion is bending about the sensitive axis. The sensitive axis is defined as the axis along or around which the stiffness is minimum. The nonsensitive axis is defined as the axis along or around which the stiffness is relatively large. In design of flexure mechanisms, the sensitive-axis deformation should be utilized to achieve the desired motion, and the nonsensitive-axis deformation should be avoided. The advantage of leaf springs is that they can achieve large motion range. Nevertheless, their lengthwise axis stiffness is large, prone to buckling under the axial compressive load and stiffening in the presence of the axial tensile load.

To increase the stiffness ratio of the nonsensitive axis to the sensitive axis, many researchers develop and study new flexure hinges with elliptical, parabolic, hyperbolic and corner-filleted cross sections [16]. Their sensitive axes are also perpendicular to the plane in Fig. 2.1, and the sensitive motions are bending about the sensitive axes. Stress concentration usually occurs at the surface of the thinnest portion, which limits the maximum bending.

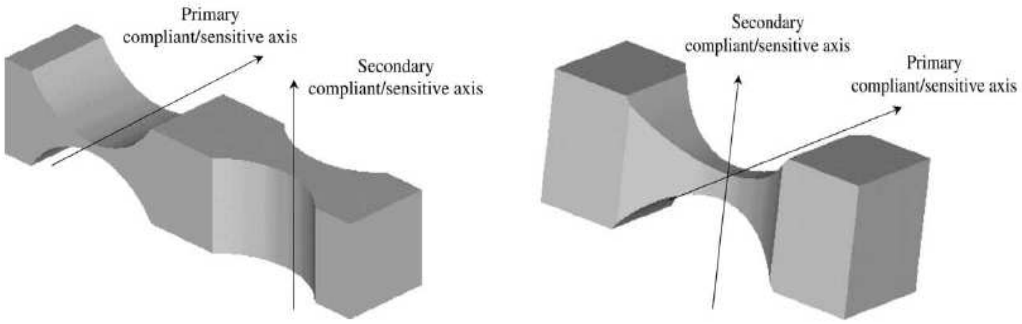

(a) Two-axis eccentric flexure hinge (b) Two-axis concentric flexure hinge

Figure 2.2: Two-axis flexure hinges

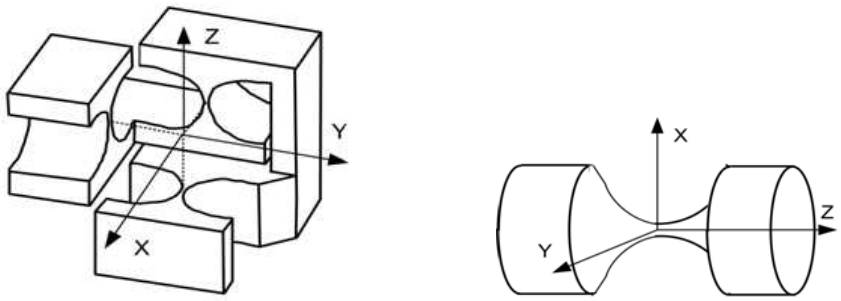

(a) Three-axis eccentric flexure hinge (b) Three-axis concentric flexure hinge

Figure 2.3: Three-axis flexure hinges

2.1.2 Multi-Axis Flexure Hinge

Multi-axis flexure hinges can be categorized into two types, eccentric and concentric. As illustrated in Fig. 2.2, universal flexure hinges have eccentric and concentric structures [19]. The first type is a serial combination of two single-axis flexure hinges. For compactness required in some applications, the second type, with concentric structure is developed. Similarly, spherical flexure hinges also have eccentric and concentric structures [19, 20], shown in Fig. 2.3. Usually, concentric structures are complicated to be fabricated.

2.2 Flexure Mechanism

There are many flexure mechanisms in the current research. Flexure mechanisms can be categorized as different types according to different classification viewpoints. Classified by the principles of the actuation manner, the contact manner and the structure type, the

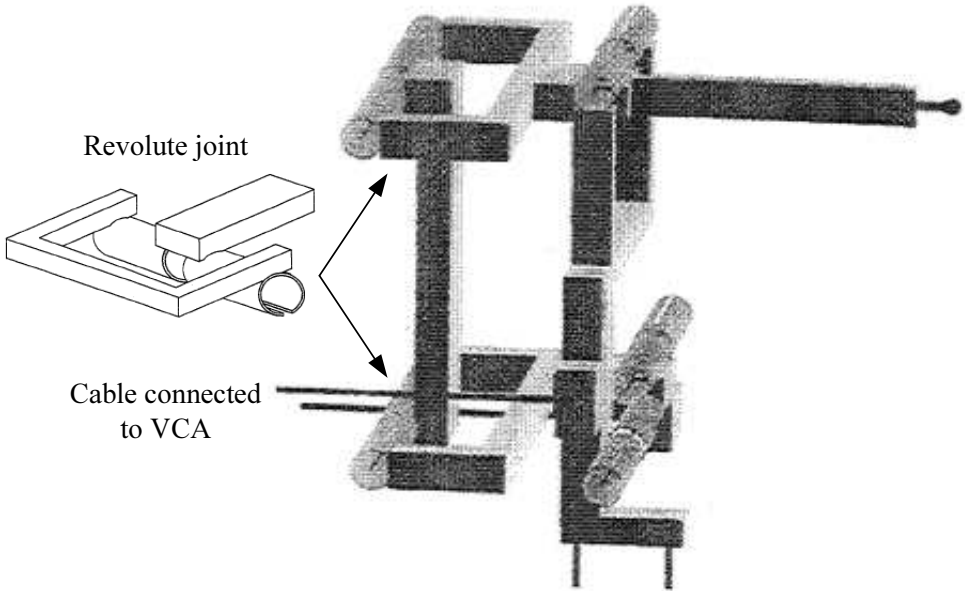

Figure 2.4: 2-DOF five-bar mechanism

current studies of flexure mechanisms are introduced as follows.

2.2.1 Flexure Mechanism Classified by Actuation Manner

According to the actuation manner, flexure mechanisms can be categorized as the linear-actuated and the rotary-actuated types. In linear-actuated flexure mechanisms, actuation forces are applied at the ends of mechanisms, and all of flexure hinges are passive. For example, the 2-DOF five-bar micromanipulator, designed by Goldfarb [21] (shown in Fig. 2.4), is linearly driven via cables pulled by voice coil actuators. The 3-DOF bridge-type manipulator, designed by Kim [22] (shown in Fig. 2.5), is linearly actuated by the piezoelectric (PZT) tube. The workspaces of these flexure mechanisms are limited by maximum elastic deformations of all passive flexure hinges.

Another type is rotary-actuated flexure mechanisms, developed by Ceccarelli [23] (shown in Fig. 2.6). In the 3-RRU manipulator, two revolute flexural joints in each limb are rotarily actuated by two SMA lines. Thus, the two revolute flexural joints are active. Compared to the above type of flexure mechanisms in which all of flexure hinges are passive, the active-flexure-hinge mechanism has the feature of large workspace. It is because that the rotary actuators mounted on flexure hinges reduce stress concentration by enforcing change of elastic deflection of flexural joints.

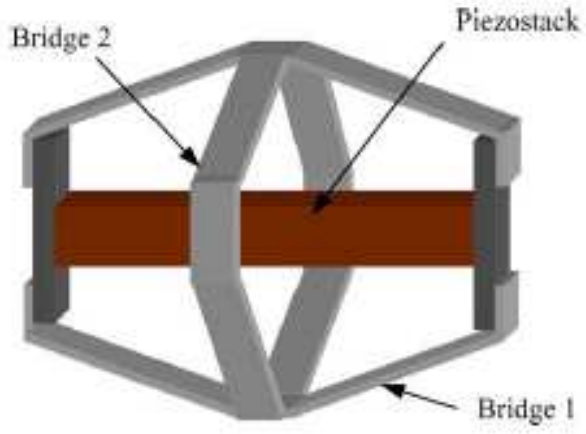

Figure 2.5: 3-DOF bridge-type mechanism

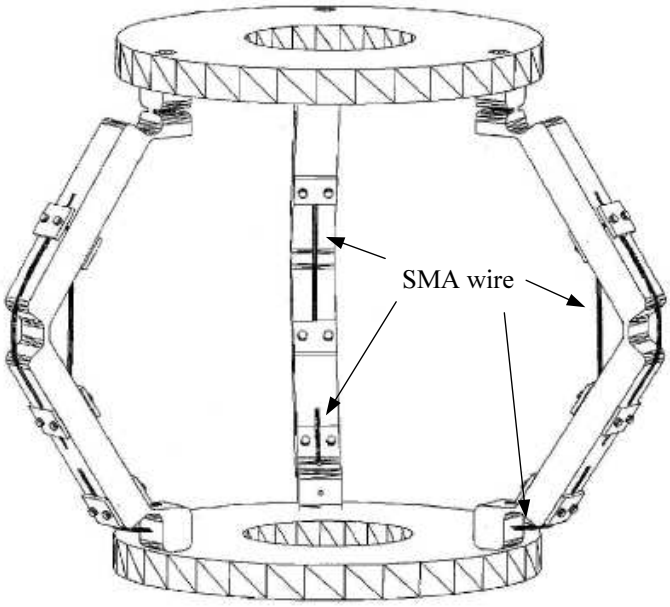

Figure 2.6: Binary actuated parallel mechanism

2.2.2 Flexure Mechanism Classified by Contact Manner

According to the contact manner, flexure mechanisms can be classified as the contact-aided and the non-contact types. Most of flexure mechanisms are usually designed and used in their linear areas, in which the input of force or displacement and the output of displacement can be approximated using a straight line. Examples can be found in the platforms mentioned in the next section.

In another situation, the relationship between the input and the output is not required to be linear, and nonlinear relationship is demanded. Nonlinearity can be achieved by contact-aided flexure mechanisms, e.g. Fig. 2.7 [24].

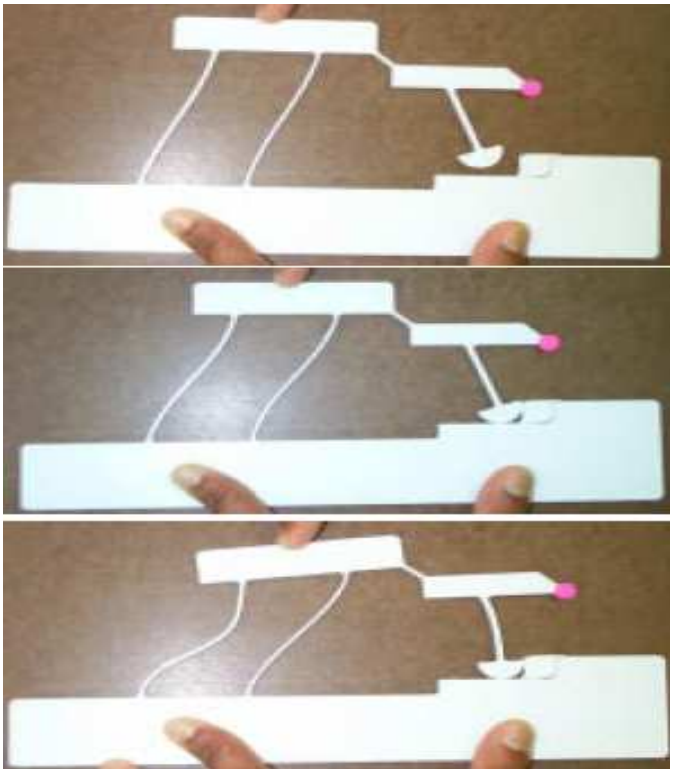

Figure 2.7: Contact-aided planar mechanism

2.2.3 Flexure Mechanism Classified by Structure Type

Similar to rigid-body mechanisms, flexure mechanisms have several commonly used structures, i.e., 6-DOF, $XY\theta_Z$, $\theta_X\theta_Y Z$ and *XYZ*, *XY*, and 1-DOF platforms.

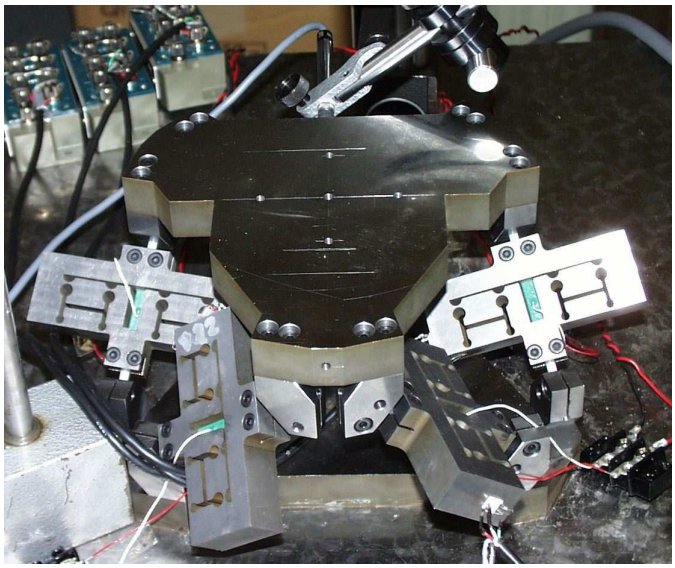

Figure 2.8: 6-DOF fine-motion Stewart platform

6-DOF Platform

A 6-DOF fine-motion platform (shown in Fig. 2.8) developed by Oiwa [25] is the compliant counterpart of the rigid-body Steward platform . The similar six-SPS-limb structure is used. The prismatic joint is actuated by the built-in PZT actuator.

The 6-DOF nano-manipulation platform designed by MIT research group [26] is a serial combination of two parallel stages, $XY\theta_Z$ and $\theta_X\theta_Y Z$ platforms (shown in Fig. 2.9). The translational workspace can reach $140\mu m \times 140\mu m \times 140\mu m$, and the orientational workspace can achieve $2.4^\circ \times 2.4^\circ \times 7.6^\circ$.

The 6-DOF nano-manipulator with planar structure (shown in Fig. 2.10) is designed by Culpepper et al. [27]. The two-axis magnetic actuators are used to accomplish in-plane and out-of-plane actuation. The nano-manipulator was experimentally proved to possess the resolution of $5nm$ in the small-scale range of $100nm \times 100nm \times 100nm$, and the motion error less than 0.2% in the large-scale range of $100\mu m \times 100\mu m \times 100\mu m$.

3-DOF Platform

$XY\theta_Z$ **Platform**

Most of $XY\theta_Z$ platforms have planar structures. For example, Yi [28] has designed a planar $XY\theta_Z$ platform, which has the workspace of $100\mu m \times 100\mu m \times 0.1^\circ$ (shown

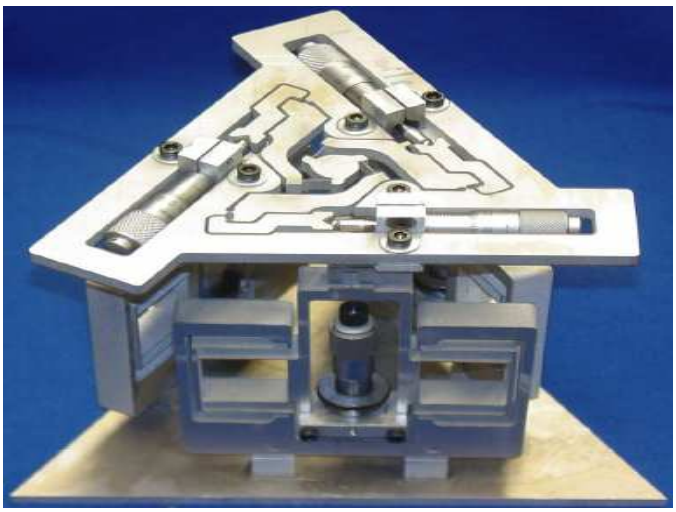

Figure 2.9: 6-DOF hybrid nano-manipulator

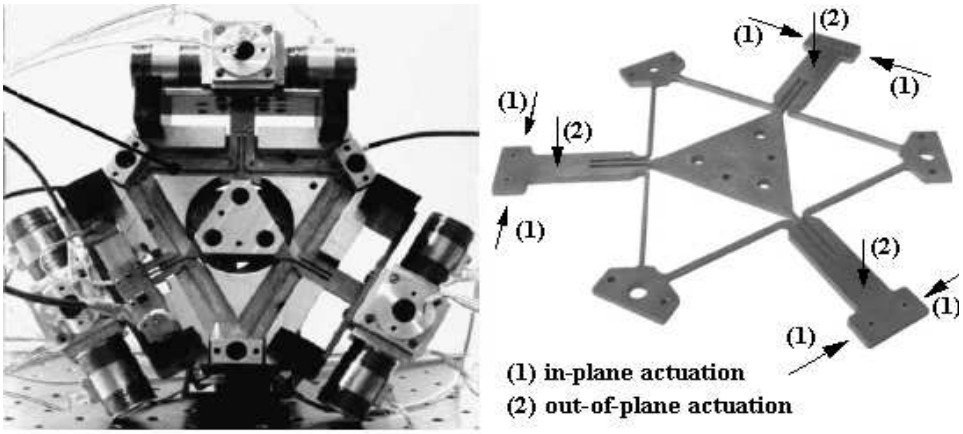

Figure 2.10: 6-DOF nano-manipulator with planar structure

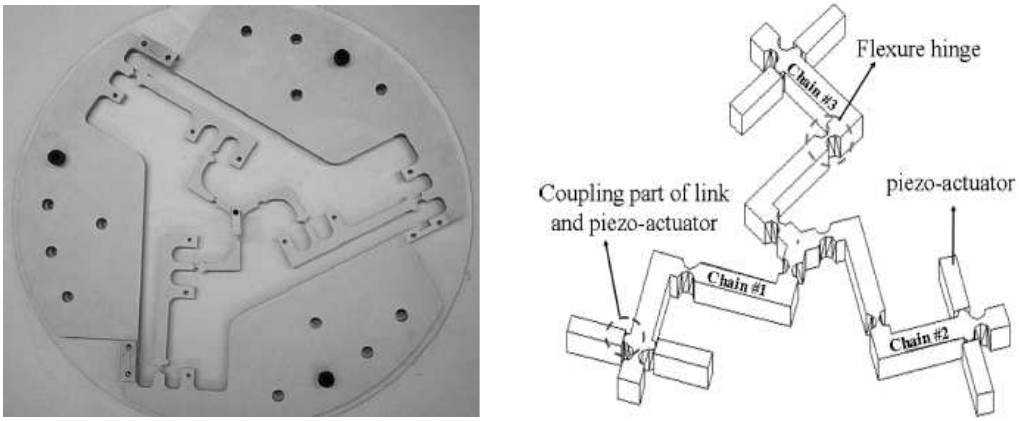

(a) Prototype of 3-RRR $XY\theta_Z$ platform (b) Schematic of 3-RRR $XY\theta_Z$ Stage

Figure 2.11: 3-RRR $XY\theta_Z$ platform

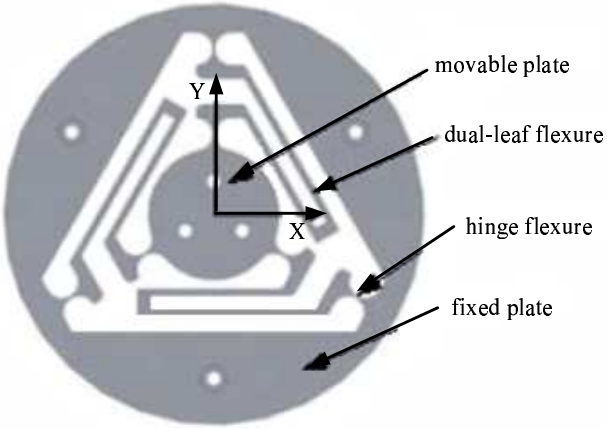

Figure 2.12: Leaf-based $XY\theta_Z$ platform

in Fig. 2.11). The stiffnesses of the translational motions along the X- and Y-axes are $9.50N/mm$ and $9.45N/mm$, and the stiffness of the rotation about the Z-axis is $0.062N \cdot m/deg$.

A planar $XY\theta_Z$ platform (shown in Fig. 2.12) using three folded leaf spring has been worked out by Chen [29]. Within the range of $15\mu m$ in translation and $0.07°$ in rotation, the deformation shows a good linearity to the applied force. The stiffness of the translational motion is $19.38N/mm$ and that of the rotation is $11.62mN \cdot m/deg$. This flexure platform is experimentally proved that it has a potential application to the optical switch assembly.

A spatial $XY\theta_Z$ platform (shown in Fig. 2.13) using leaf springs is developed by Chen [30].

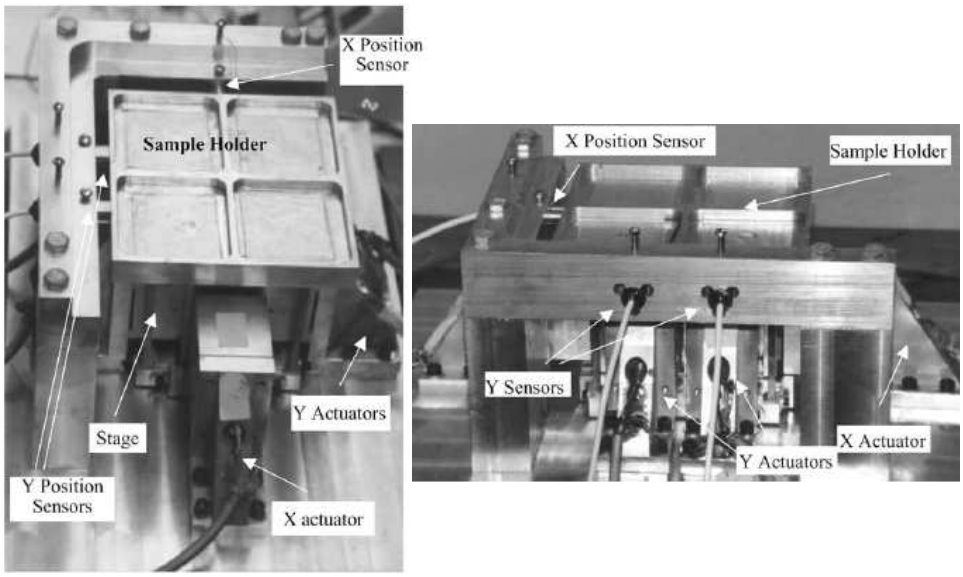

(a) Prototype of spatial $XY\theta_Z$ platform

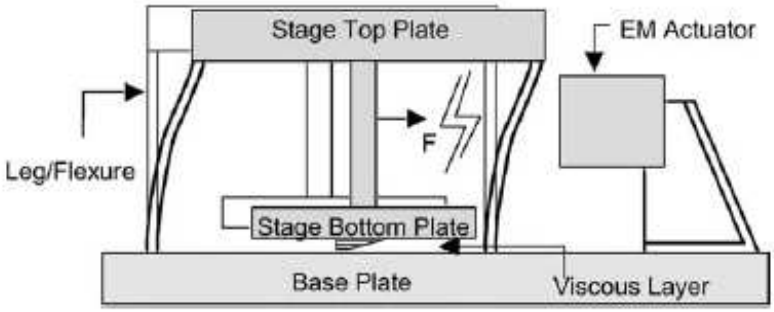

(b) Schematic of spatial $XY\theta_Z$ platform

Figure 2.13: Spatial $XY\theta_Z$ platform

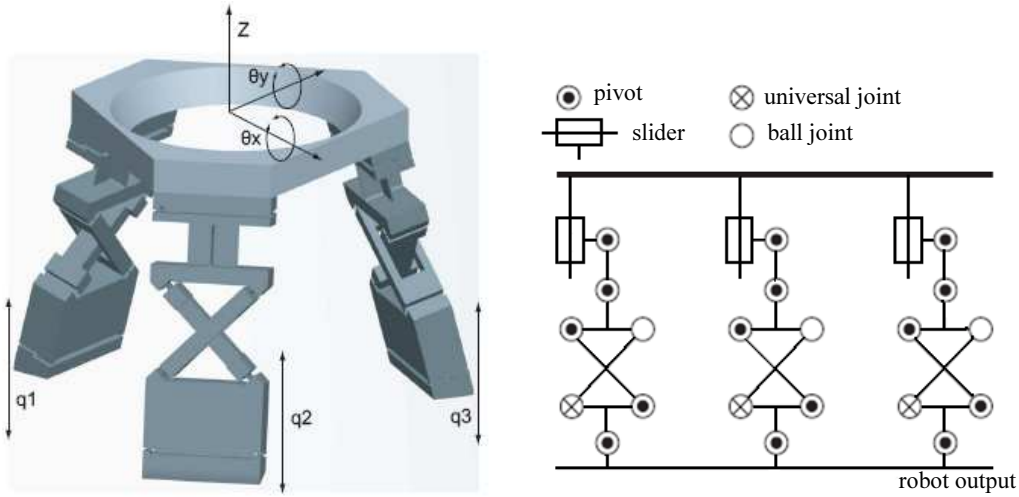

(a) Prototype of Orion miniangle platform (b) Schematic of Orion miniangle platform

Figure 2.14: Orion minangle $\theta_X\theta_Y Z$ platform

This spatial structure avoids the problem of flexure buckling. The translational workspace is $\pm 50\mu m \times \pm 50\mu m$, and the rotary range is $4.4mrad$. The X-axis translational motion is activated by one electromagnetical actuator along the X-axis, and the Y-axis translational motion is pushed synchronously by the two electromagnetical actuators along the Y-axis. The rotation about the Z-axis is actuated asynchronously by the two same electromagnetical actuators along the Y-axis.

$\theta_X\theta_Y Z$ Platform

Limited by manufacturing technology and with the consideration of time-exhaustive computation for coupled kinematics, multi-DOF flexure mechanisms are replaced by low-mobility flexure mechanisms arranged in serial. $\theta_X\theta_Y Z$ platforms are one common type of low-mobility structures. Most of $\theta_X\theta_Y Z$ platforms have spatial parallel structures. For example, EPFL group [31] has worked out a $\theta_X\theta_Y Z$ platform (shown in Fig. 2.14) with the rotation range of $\pm 15°$. The three pivot sliders are connected to the linear actuators.

***XYZ* Platform**

XYZ platforms are another type of low-mobility structures. Liu [32] worked out a 3-RRPR compliant micromanipulator (shown in Fig. 2.15) for gene injection. The workspace is about $200\mu m \times 400\mu m \times 400\mu m$, and the repeatability reaches $0.1\mu m$.

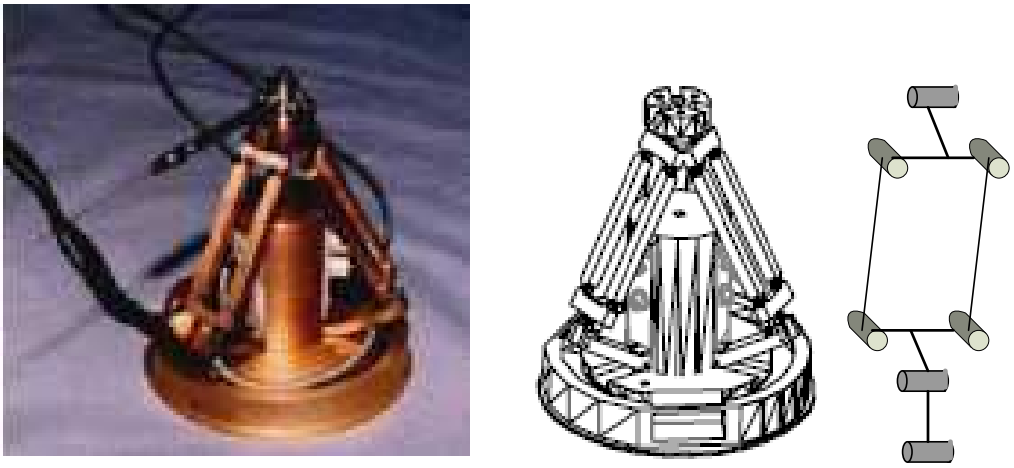

(a) Prototype of 3-RRPR compliant micromanipulator

(b) Schematic of 3-RRPR compliant micromanipulator

Figure 2.15: 3-RRPR compliant micromanipulator

However, the kinematics of this structure is coupled.

Koseki [33] proposed a 3-limb parallel structure (shown in Fig. 2.16) for a translational 3-DOF flexure mechanism. Three PZT actuators are mounted to push the middle plate of the limb. However, this structure is also coupled.

The *XYZ* Delta platform (shown in Fig. 2.17) with the dimension of $200mm \times 200mm \times 200mm$ studied by Clavel et al. [34] has a large workspace more than $1mm \times 1mm \times 1mm$ and a high positioning precision of $10nm$, and the linear stiffness is $30N/mm$. The *XYZ* platform utilizes an isotropic structure to achieve the three decoupled translational motions, and this characteristics simplifies the control algorithm without complex decoupling calculation.

2-DOF Platform

XY platforms have planar structures, and are actuated in-plane. The main problems are the cross-axis error and the rotation error in-plane. Through synthesis and with the consideration of small cross-axis error and small rotation error, Awtar [10] designed a large-displacement and small-parasitic-motion *XY* platform with the dimension of $300mm \times 300mm$ (shown in Fig. 2.18). The workspace can reach $5mm \times 5mm$. This platform is of symmetric structure and under symmetric constraints, therefore its cross-axis error is on the order of one part in one thousand and yaw error is on the order of a

(a) Prototype of translational 3-DOF micro-parallel mechanism

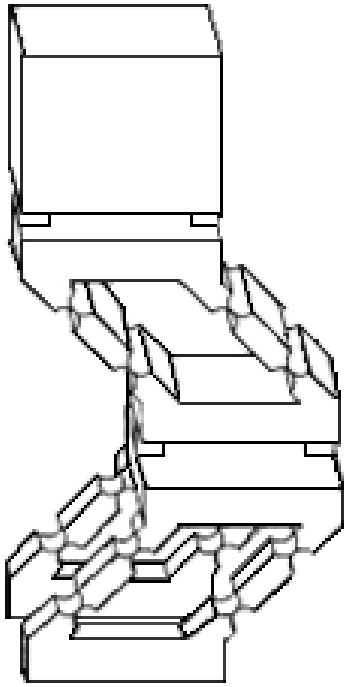

(b) Limb of translational 3-DOF micro-parallel mechanism

Figure 2.16: Translational 3-DOF micro-parallel mechanism

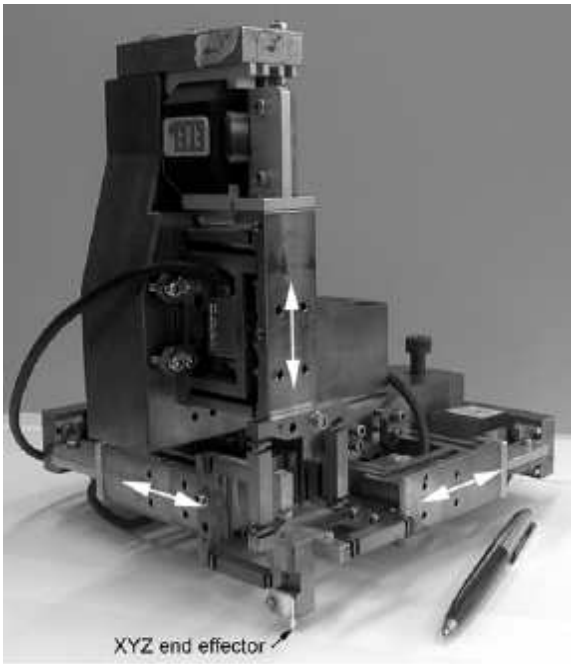

(a) Prototype of *XYZ* Delta platform

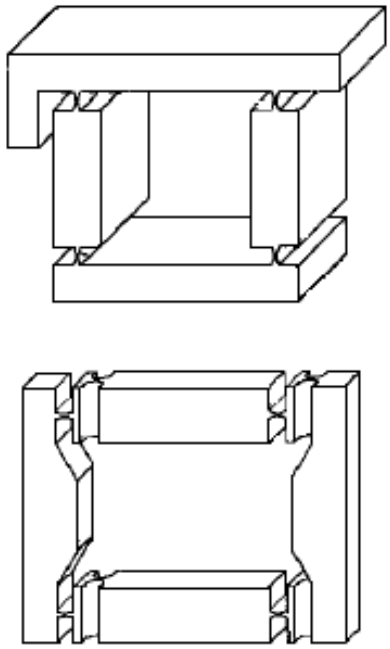

(b) Prismatic joints of *XYZ* Delta platform

Figure 2.17: *XYZ* Delta platform by EPFL

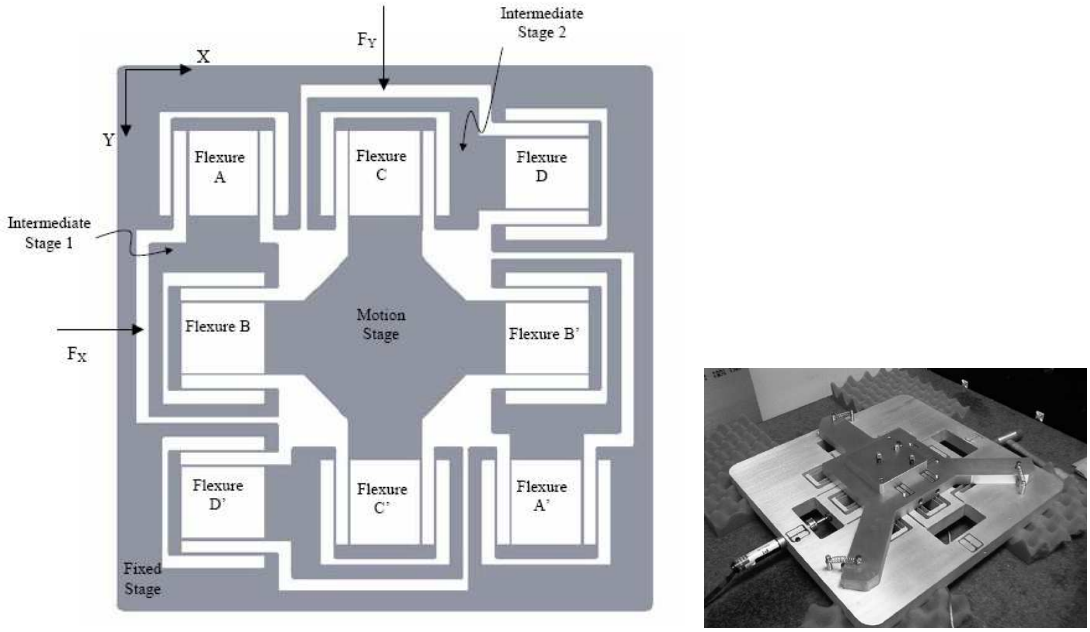

(a) Schematic of *XY* Platform (b) Prototype of *XY* Platform

Figure 2.18: *XY* platform

few arc second.

Single-DOF Prismatic Joint

The prismatic joint is expected to generate a linear motion without parasitic motions, when a linear force is applied. The parasitic motion in the prismatic joint is defined as the cross-axis coupling between the two translational motions. The conventional prismatic joint [35] is shown in Fig. 2.19(a). The drawbacks of this type of prismatic joint are parasitic motion and small motion range. When there is no DOF-constraint perpendicular to the actuation direction, the parasitic motion along this direction will occur. When the DOF-constraint perpendicular to the actuation direction is applied, the axial tensile load will be generated in flexure hinges, which leads to linear stiffness increasing of the prismatic joint. The improved prismatic joint [35, 36] in Fig. 2.19(b) solves these two problems. However, its drawback is the asymmetric structure without uniform thermal expansion. To solve the asymmetry problem, such two identical joints can be combined to form a symmetric prismatic joint (shown in Fig. 2.19(c)), and the linear stiffness is doubled.

Another type of prismatic joint (shown in Fig. 2.20) was designed by Kota [37]. This

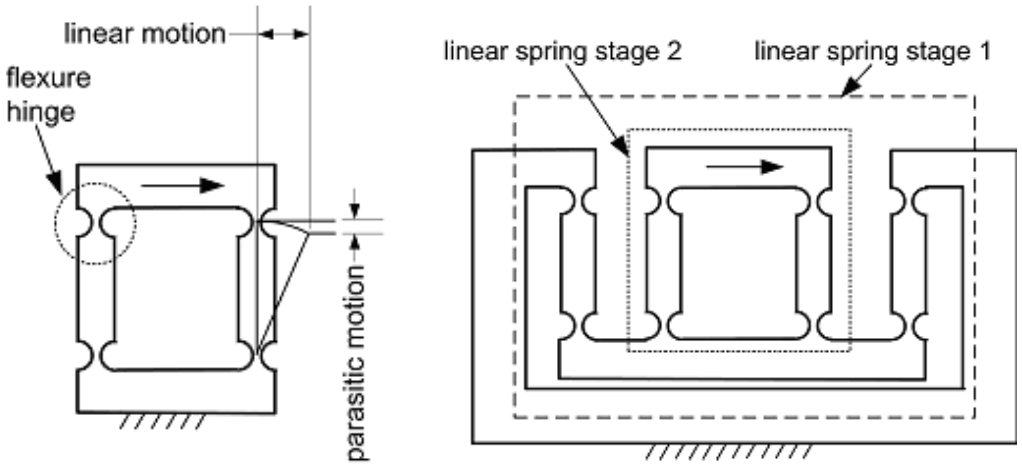

(a) Conventional prismatic joint

(b) Improved large-motion prismatic joint

(c) Symmetric large-motion prismatic joint

Figure 2.19: Prismatic joints

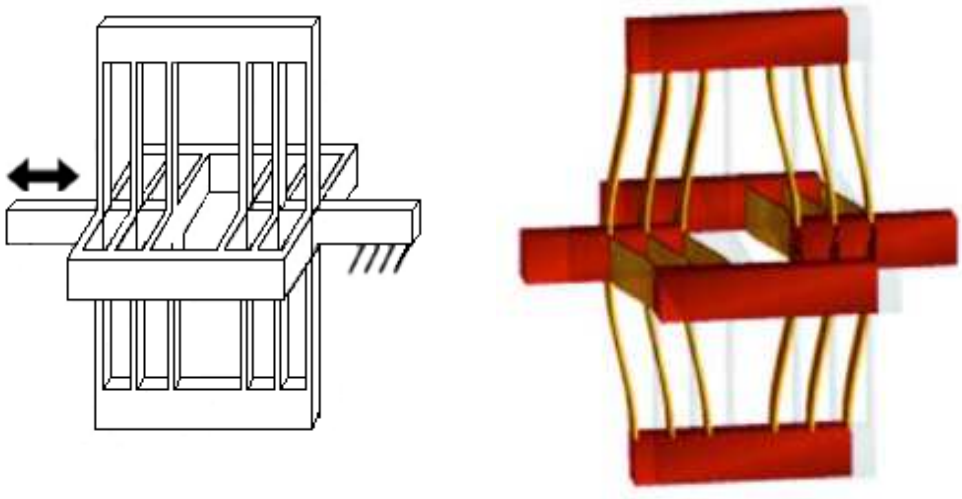

Figure 2.20: Large-motion prismatic joint by Kota

type of prismatic joint has the advantages of large motion range, small axis drift, less stress concentration, high off-axis stiffness and compactness. The drawback is difficulty of fabrication using metal material cutting by wire electro-discharge machining (EDM) as described in [37], and it was fabricated using plastic injection molding. Hence, the stiffness of the mechanism will be limited by its material.

Lobontiu [38] designed a new type of prismatic joint (shown in Fig. 2.21) that can be easily fabricated. However, the prismatic joint cannot produce large motion, because the notch hinges will bear the axial compressive loads when the forces are exerted on the two lateral stages. Moreover, the large axial compressive loads may lead to buckling in the notch hinges, when the axial compressive loads increase to a critical value.

2.2.4 Contributions to Mechanism Design

In the above sections, design of flexure mechanisms has been investigated. However, there are several problems summarized from the current research.

Problem of Single-DOF Prismatic Joint

In Section 2.2.3, five types of prismatic joints have been investigated, the advantages and disadvantages of the five prismatic joints are evaluated in the aspects of buckling, stiffening and parasitic motion, listed in Table 2.1. Before addressing the advantages and

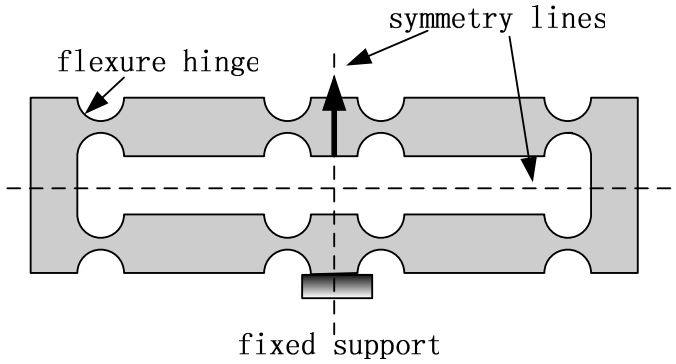

(a) Structure of prismatic joint

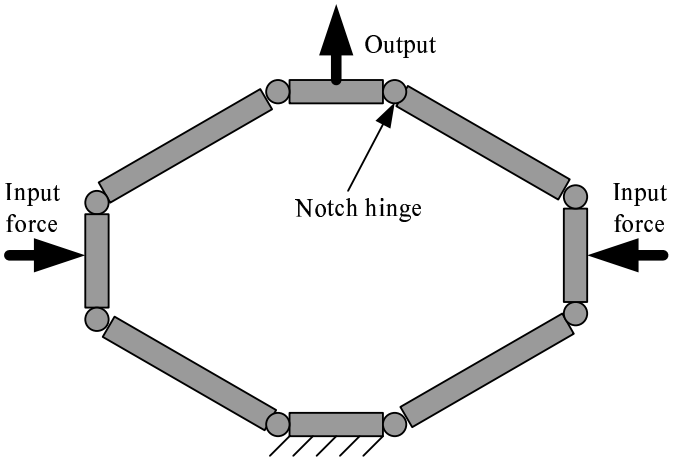

(b) Deformation of prismatic joint

Figure 2.21: Large-motion prismatic joint by Lobontiu

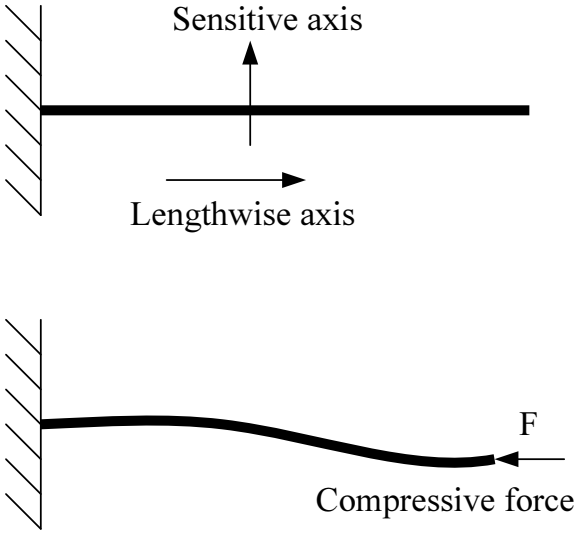

Figure 2.22: Buckling

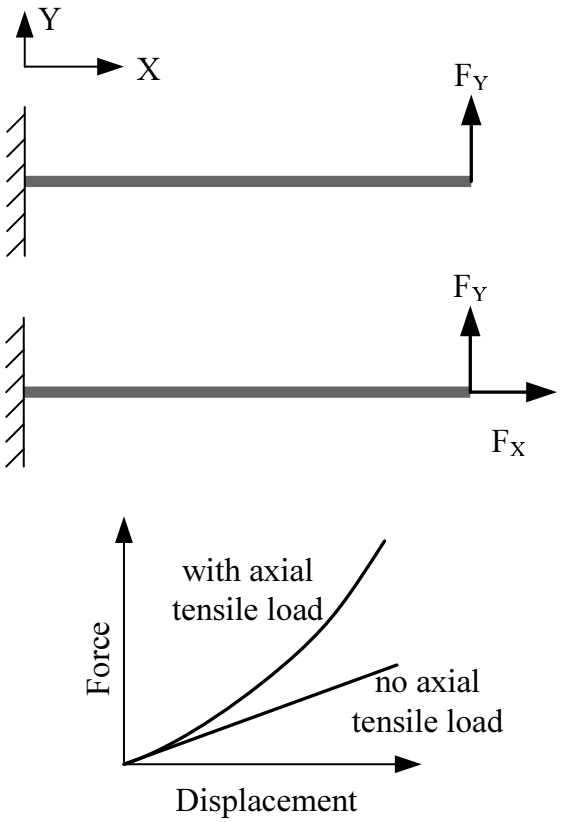

Figure 2.23: Stiffening

disadvantages, here the definitions of buckling, stiffening and parasitic motion are given to facilitate understanding the problems.

Buckling is defined as a phenomenon of structural instability characterized by loss of the equilibrium state when the external load reaches a critical value [16]. The external load mentioned here is specifically referred to the external compressive force along the lengthwise axis. The buckling phenomena is shown in Fig. 2.22. The fifth prismatic joint suffers the problem of buckling, because the input forces are applied along the lengthwise axes of the flexure hinges.

When the slender flexure hinge is subject to the combined moment and the axial tensile load, the axial tensile load will enlarge the angular-moment stiffness about the sensitive axis. Stiffness increasing under the heavy tensile load is called as stiffening [18] (shown in Fig. 2.23). The first prismatic joint suffers the problem of stiffening, if the movable stage is constrained along the axis perpendicular to the actuation direction.

Parasitic motions are generally defined as the undesirable motions. The undesirable

Table 2.1: Evaluation of prismatic joints

	Advantages	**Disadvantages**
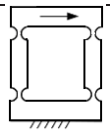	easy to fabricate	parasitic motion, stiffen (small motion range)
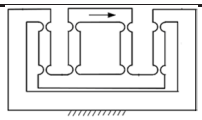	large motion range, no parasitic motion	asymmetric structure (non-uniform thermal property)
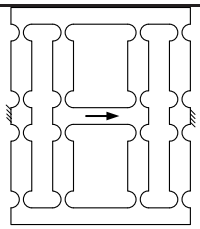	large motion range, no parasitic motion, uniform thermal property	doubled stiffness
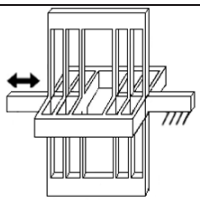	large motion range, no parasitic motion, uniform thermal property	low stiffness in non-sensitive axis, hard to fabricate
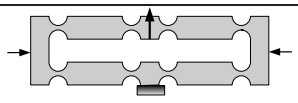	no parasitic motion, uniform thermal property	buckling

motions can be categorized as many different types. For example, if the translational motion of one subject is desired, the motions along or around other axes are regarded as parasitic motions. The first prismatic joint suffers the problem of parasitic motion, if the movable stage is not constrained along the axis perpendicular to the actuation direction, as shown in Fig. 2.19(a).

Therefore, in this research work, it is necessary to design a new type of prismatic joint which has no the above problems. Design of the new type of prismatic joint will be addressed in Chapter 3.

Coupling Problem of Multi-DOF Platform

From the investigation in Section 2.2.3, it can be concluded that the 6-DOF platforms have a common problem of coupling. In rigid-body mechanisms, the analytical models are possible to be exactly formulated and decoupling control algorithms can be implemented. However, these studies cannot be directly utilized to model and control the flexure mechanisms. The first reason is that in rigid-body mechanisms, the DOFs along or around the different axes of the joints are independent, whereas, in flexure mechanisms, the deformations of flexure hinges are interactional. Hence, it is difficult to derive the exact model of the coupled flexure mechanism. The second reason is that the expected precision of flexure mechanisms is much higher than that of rigid-body mechanisms, and usually the error caused by coupling may be much larger than the expected precision in flexure mechanisms. In control algorithm implementation, it is complicated to compensate the coupling error limited by the resolutions of the hardwares. Thus, coupling in flexure mechanisms should be avoided to ensure the expected high precision. Multi-DOF motions in flexure mechanisms can be achieved by serial combination of several low-mobility and fully decoupled flexure stages. In general, the low-mobility and fully decoupled flexure mechanisms are needed to be studied.

Motion Range Problem of Platform

Motion range is another critical problem in flexure mechanisms. Concluded from the flexure mechanisms mentioned in this chapter, most of them have the limited workspace below the scale of millimeter, for example the platforms [26] [27] [28] [30] [32] . Few

platforms can possess the workspace in the scale of millimeter, for example the ones [34] [10]. However, the large-workspace platforms possess the large stage size. In the micro-manipulation applications, the platform is expected to be compact limited by the mounting space. Usually, if the dimensions of flexure mechanisms increase, the workspace will increase accordingly. Thus, in miniature flexure mechanisms, the motion range should be defined related to not only the achievable workspace but also the stage size. Here we give the definition of the motion range as follows.

Definition 2.1: Motion range is defined as the ratio of the achievable workspace to the stage size,

$$\beta = \frac{workspace}{maximum\ dimensionof\ stage\ size}.$$

The maximum workspace is determined by the yielding limit of the material. For a certain stage size, a larger value of β means that the motion range is larger. The flexure mechanisms with a large value of β is regarded to be large-motion.

The low-mobility platforms, introduced in Section 2.2.3 and 2.2.3, are evaluated with the workspace, the stage size and the motion range (listed in Table 2.2). From Table 2.2, it can be seen that the workspaces of most flexure mechanisms are limited within several hundred micrometer, and the motion ranges are mostly below $1/500$. It is important to develop flexure mechanisms with large workspace and large motion range as well. This thesis focuses on this issue, and the dimension optimization in Chapter 5 is based on these criteria.

Table 2.2: Evaluation of flexure mechanisms

Stages	**Workspace**	**Stage size**	**Motion range** β
XY [10]	$5mm \times 5mm$	$300mm \times 300mm$	$1/60$
6-DOF [27]	$100\mu m \times 100\mu m \times 100\mu m$	$> 100mm \times 100mm$	$< 1/1000$
$XY\theta_Z$ [28]	$100\mu m \times 100\mu m \times 0.1°$	$> 200mm \times 200mm$	$< 1/2000$
XYZ [32]	$200\mu m \times 400\mu m \times 400\mu m$	$> 100mm \times 100mm \times 100mm$	$< 1/500$

2.3 Structure Synthesis of Decoupled *XYZ* Flexure Mechanisms

As explained in Section 2.2.4, the coupling problem of multi-DOF flexure mechanisms leads to difficulty of exact modeling and compensation. Thus, the study on low-mobility and fully decoupled flexure mechanisms is important. Among low-mobility flexure mechanisms, the *XYZ* platform is a fundamental type. The *XYZ* platforms can be designed to be fully decoupled, and in such fully decoupled structures, exact modeling and precise position control become possible. The *XYZ* platform can be easily incorporated with other type of low-mobility platform to form a multi-DOF platform, and it also has the extensive applications in the micromanipulation, including the fine-tuning platforms in microscope and fiber alignment.

In Section 2.2.3, several *XYZ* flexure mechanisms have been introduced, but they are studied on case-by-case basis. Structure synthesis of *XYZ* flexure mechanisms has been studied by Arai using Lie Group Theory [39], and 3-3R1P and 3-2R2P configurations are proposed. Nevertheless, these synthesized structures are coupled. Currently, there is no research focused on structure synthesis of decoupled *XYZ* flexure mechanisms. Thus, the study on structure synthesis of decoupled *XYZ* flexure mechanisms in this research work is meaningful.

Structure synthesis of decoupled *XYZ* flexure mechanisms can be studied referring to the approaches for rigid-body mechanisms, i.e., the constraint synthesis approach based on the screw theory [40, 41, 40, 42, 43, 44], and the Lie sub-group approach based on the algebraic properties of a Lie group of the Euclidean displacement set [45, 46, 47].

Nevertheless, structure synthesis of flexure mechanisms is not totally the same as that of rigid-body mechanisms. Due to limitation of fabrication, maximum elastic deformation, buckling, stiffening and so on, flexure mechanisms have more constraints on structural configurations. The methodologies suitable to rigid-body mechanisms cannot be directly applied to flexure mechanisms. The issue of structure synthesis of flexure mechanisms will be addressed in Chapter 3.

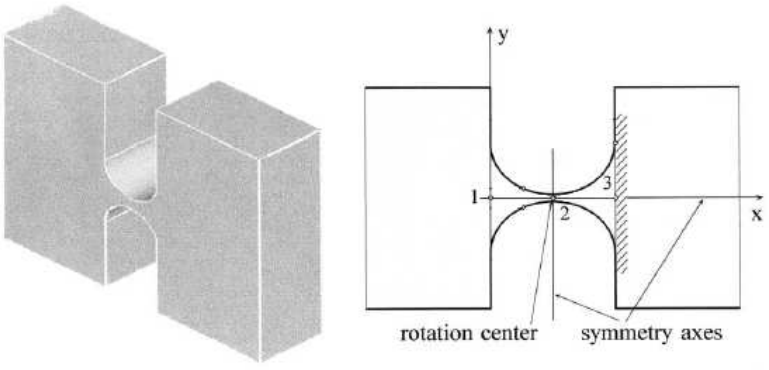

Figure 2.24: Notch hinge

2.4 Modeling Method

Flexure mechanisms are composed of flexure hinges and relatively rigid connection links. The modeling approaches can be categorized into two types. In the first method, the lumped-compliance type, all deformations are regarded to be concentrated in flexure hinges, and the connection links are considered as rigid. In the second method, the continuous-compliance type, flexure hinges and connection links are both regarded to be flexible.

In the first method, modeling of flexure hinges is critical. As mentioned in Section 2.1, flexure hinges have four types classified by the cross section, i.e., leaf spring, circular, conic and corner-fillet. Smith [18] has formulated deflections of leaf springs under different loads and different constraints, including the axial compressive forces, the combined axial and tangential loads, and the combined axial and tangential loads plus a moment applied to the free end. Modeling of circular-, conic- and corner-fillet-sections flexure hinges is more difficult than that of leaf springs, because the cross-section area of notch hinges is variant. Paros and Weisbord [19] used basic beam theory to derive deflection of the circular-section notch hinge (shown in Fig. 2.24). The notch hinge is assumed to possess 5 DOFs, i.e., three translational DOFs along the X-, Y- and Z-axes, and two rotational DOFs about the Y- and Z- axes. The compliance matrix (5×5) of the 5-DOF motions has been derived, and can be used to calculate deflections at the free end. Based on Paros and Weisbord's study, Lobontiu [16] extended compliance study to notch hinges with tdifferent cross sections. Flexure hinges with circular-, conic- and corner-filleted-sections are studied, and the compliance matrices of flexure hinges

are formulated. However, these three methods have limitations. The exact compliance formulations of flexure hinges can be used to the stiffness models of entire flexure mechanisms, but it is difficult to derive the dynamic equations of flexure mechanisms. In order to obtain both the static and dynamic models of flexure mechanisms, Howell [17] proposed an approximate method, the PRB method. The PRB method assumes notch hinges as single- or multi-axes center-fixed revolute joints, and links connecting the centers of every two notch hinges as rigid components. The method has been extensively used to approximately formulate static stiffness and dynamics of flexure mechanisms using notch hinges, for example [48, 49, 50, 51, 52, 53, 54]. However, as this method is an approximate solution, there is some difference from the experimental results.

In the second method, both flexure hinges and connection links are assumed as flexible components. Finite element method (FEM) is based on this assumption. The principle of FEM is that the flexible components are divided by some nodes, and the divided portions are formulated and connected by the constraint conditions. Du [55] proposed a nonlinear FEM model, which considered geometric nonlinearity due to large deflection. Chen [56], Maute [57] and Farid [58] used FEM to formulate the exact dynamic models of flexure mechanisms. Whereas, the computation work will be heavy if the flexible component has a variant section area, and the accuracy mainly depends on the density of meshing nodes. Currently, some commercial softwares such as ANSYS, ABAQUS, etc. have been used for numerical analysis of flexure mechanisms.

Therefore, an exact analytical modeling method is required for both stiffness and dynamic models of flexure mechanisms. In this thesis, such method is proposed for modeling of the large-displacement prismatic joints addressed in Chapter 4.

2.5 Control Algorithm

In order to develop the flexure-based micromanipulator with high positioning precision and fast response, the control algorithm is critical. The control algorithms for flexure mechanisms are required to solve the following problems.

- Unmodeled uncertainty

In the actual operation, high-order mode shapes which are not desired and difficult to be modeled are also stimulated. The current modeling methods are also difficult to formulate completely exact models of flexure mechanisms. The difference between the analytical model and the actual plant is called as unmodeled uncertainty. The control algorithm is required to possess robustness to unmodeled uncertainties.

- Vibration due to low damping

  Damping in flexure mechanisms is caused by thermal dissipation during elastic deformations, and the value of thermal dissipation is small. Small damping leads to vibration of flexure mechanisms. The control algorithm is also required to suppress vibration.

- External disturbance

  Since the desired positioning precision of flexure mechanisms is high at micro- or nano-scale, the external disturbances, i.e., the electric noise, the external vibration, etc., will reduce the precision. The control algorithm should possess robustness to the external disturbances.

In current research, there are several control algorithms designed for flexure mechanisms, including PID control, state feedback control, neural network control, sliding mode control and H_∞-control.

PID and State Feedback Control

An improved PID controller was designed for 3-DOF micropositioning tower by Jouaneh [59]. Different from the conventional PID controller, the improved PID controller possesses partial robustness, achieved by a 6th-order dynamic model using system identification, combined with a 4th-Chebyshev filter for high-order uncertainties. State feedback [60] was used to the controller of a micropositioning tool by Okazaki [61].

However, these two control algorithms are not fully robust, because robustness to unmodeled uncertainties mainly depends on the accuracy of dynamic models obtained from system identification. Moreover, robustness to external disturbances and vibration suppression are not solved by these two control algorithms.

Neural Network Control

Yesildirek [62] proposed a neural network controller for joint-position tracking of flexible-link manipulators using the singular perturbation techniques. The key feature of the approach is that no exact knowledge of the dynamics of the robot arms is assumed for the controller, and no off-line training is required for the neural network.

Talebi [63] developed the neural-network based controllers for tip-position tracking of flexible-link manipulators utilizing the modified output redefinition approach. The neural controllers have no need for a priori knowledge of the payload mass. The performance of the controllers is demonstrated by simulations for a two-link planar flexible manipulator and by experiments for a flexible single-link testbed.

In the system designed by Cheng [64], the neural network technique was introduced to the stable tracking control of a flexible macro-micro manipulator system. A two-layer neural network is utilized to approximate the nonlinear robot dynamic behavior of this system, and the controllers for the macro and micro arms are developed without any need for prior knowledge of the dynamic model. A learning algorithm for the neural network using the Lyapunov stability theory is derived. Both the tracking error and the weight-tuning error are uniformly bounded under this new control scheme.

Sliding Mode Control

Sliding mode control [65, 66] is a systematic approach for the flexure-based system. The expected performances can be designed as the sliding surfaces, and the boundaries are estimated with the consideration of unmodeled uncertainties and external disturbances. All the states within the boundaries tend toward the surface and slide on the surface ultimately. Therefore, robustness of the flexure-based micromanipualtor can be ensured, even without an exact dynamic model.

In the mechanism developed by Woronko [67], a flexure slider was used to establish a piezoelectric tool actuator, and this actuator was for precision machining on the conventional CNC turning centers. Uncertainties are from the cutting force disturbances during precision machining and piezoelectric nonlinearity . A sliding mode controller is implemented which provides wide bandwidth and high tool positioning precision, and at the

same time rejects the uncertainties mentioned above.

Another example of the sliding mode control is for position control of a compliant mechanism based micromanipualtor which has the three translational DOFs [68]. The compliant mechanism possesses a large motion range, and thus structural nonlinearity occurs. The unmodeled uncertainties result from the parameter variations of the inertias and the masses of both the flexible and rigid components, and the stiffnesses associated with the split-tube flexures. The sliding controller verifies the tracking performance and the desired bandwidth, with the consideration of the structural nonlinearity and the unmodeled uncertainties.

H_∞-Control

Another robust control algorithm [69, 70] that can be used for flexure mechanisms is H_∞-control. Briefly, the theory of H_∞-control is to design a controller to minimize the H-norms of transfer functions from the unmodeled uncertainties, the external disturbances or positioning error to the external outputs.

An H_∞-controller using μ-synthesis is designed by Karkoub [71] for a flexible rotary beam. The H_∞-controller is designed for tracking performance, robust to unmodeled dynamics, input and actuation uncertainties and noise.

Low damping is a common problem in flexure mechanisms. Damping of flexure mechanisms is due to energy dissipation during deformation, and thus the value is quite small. Low damping will lead to vibration, and the dynamic response will be slow. Vibration suppression is required to be considered in design of control algorithm. H_∞-robust controllers can achieve vibration control, such as [72, 73, 74].

In this thesis, a hybrid controller is designed based on the H_∞-theory. Hybrid position and vibration control realizes both tracking performance and vibration suppression, with robustness to unmodeled uncertainties and external disturbances.

Chapter 3

Structure Synthesis of Large-Motion and Decoupled *XYZ*-FPMs

The three-translational rigid-body parallel mechanisms have been synthesized and analyzed by Jin [75], Gao [76], Huang [40], Frisoli [77], Huang [78] and Gosselin [79, 80]. A new group-decoupled parallel mechanism, which can also achieve the three decoupled translational motions, is studied by Jin [81, 82]. However, these studies are related to rigid-body mechanisms. Structure synthesis of flexure mechanisms is different from that of rigid-body mechanisms. In this chapter, structure synthesis of large-motion and decoupled *XYZ*-FPMs is systematically studied. Section 3.1 summarizes the characteristics of flexure mechanisms, which are different from those of rigid-body mechanisms, and represents these characteristics as the constraint conditions of structure synthesis of flexure mechanisms. To configure large-motion *XYZ*-FPMs, the fundamental component, the prismatic joint, is designed in Section 3.2. Subjected to the summarized constraint conditions and using the new type of prismatic joint, decoupled *XYZ*-FPMs are synthesized in Section 3.3. The mobilities of the synthesized large-motion and decoupled *XYZ*-FPMs are also analyzed in Section 3.3.

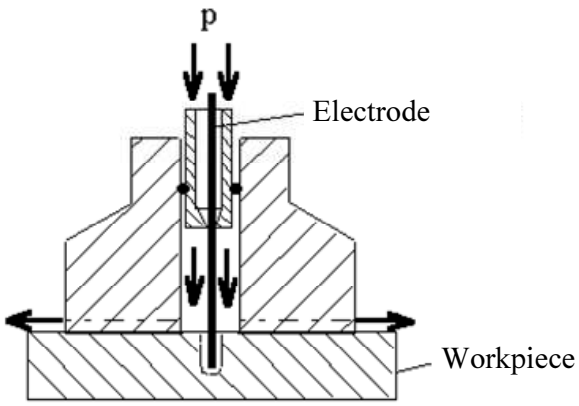

Figure 3.1: EDM manufacturing process

3.1 Characteristics of Flexure Mechanisms

Structure synthesis of flexure mechanisms is not totally identical to that of rigid-body counterparts. Differences include workspace, available joint types, actuated joint types, and phenomena of stiffening and buckling. These differences limit the configurations of flexure mechanisms. The main limitations are summarized as follows.

Limitation of Available Joint

In rigid-body mechanisms, all of prismatic joints, revolute joints, universal joints and spherical joints can be assembled to configure the structures. Whereas, in flexure mechanisms, types of available joints used in flexure mechanisms are limited because of manufacturing techniques. The common manufacturing method is EDM, the manufacturing process being shown in Fig. 3.1. The workpieces manufactured by EDM method possess the uniform thickness. Leaf springs and flexure hinges introduced in Section 2.1.1 are produced by cutting the extra materials, and uniform-thickness flexure blades are produced. The multi-DOF flexure hinge with a concentric axis introduced in Section 2.1.2 is seldom used because the thickness is not uniform and fabrication is complicated. Therefore, in flexure mechanisms, only revolute joints and prismatic joints are available. Short leaf springs and flexure hinges can function as revolute joints. Prismatic joints have no direct counterparts, and are replaced by flexure hinge-based parallelogram chains. The structure of prismatic joints has been introduced in Section 2.1.3, and a new type will be addressed in Section 3.2.

Limitation of Actuation Joint

There are two types of commercial high-precision actuators commonly used in flexure mechanism, PZT actuators and VCAs. Both of them are linear actuators, which produce forces to push flexure mechanisms. Correspondingly, in flexure mechanisms, the actuation joint is the prismatic joint, and all revolute joints are passive. Thus, each kinematic limb of the flexure mechanism possesses at least one prismatic joint closely connected to the base, which is actuated by PZT actuators or VCAs.

Avoidance of Stiffening and Buckling

The definition of buckling has been given in Section 2.2.4. Briefly speaking, it is caused by the axial compressive load exerted on the slender beam. Thus, in order to avoid the phenomenon of buckling, the structure constraint of flexure mechanisms can be described that, the actuation force should not be collinear with or parallel to the lengthwise axes of flexure hinges.

The definition of stiffening has also been given in Section 2.2.4. Briefly speaking, it is caused by the axial tensile load exerted on the slender beam. Therefore, this structure constraint can be represented that, for structure design of flexure mechanisms, extension along the lengthwise axes of flexure hinges should be compensated and nullified, to avoid the phenomenon of stiffening.

Limitation of Manufacturing

The common fabrication method for flexure mechanisms has been mentioned in Fig. 3.1. For single flexure hinges, those with uniform thickness (shown in Fig. 2.1) can be manufactured by the current techniques such as EDM. However, for concentric flexure hinges (shown in Fig. 2.2(b) and Fig. 2.3(a)), it is quite difficult to be manufactured. Thus, in the kinematic limb, only one-DOF joints can be integrated. Furthermore, the sensitive-axes of revolute joints in one kinematic limb are parallel.

3.2 Design of Large-Motion Prismatic Joint

In Section 2.2.3, several types of conventional prismatic joints are investigated, and in Section 2.2.4, their problems are studied. Thus, it is necessary to design a new type of prismatic joint with large motion range, no parasitic motion, no buckling and no stiffening. The new type of prismatic joint is designed, as shown in Fig. 3.2.

Its linear stiffness is the same as that of the prismatic joint in Fig. 2.19(b), if the radius R of the flexure hinges, the thickness t, the length L and the width b are identical to those of the prismatic joint in Fig. 2.19(b). Their working principles are also identical. The main difference is the secondary stages. If the secondary stage in Fig. 2.19(b) is divided into two pieces, and the two separated portions are rotated $+90^\circ$ and -90° respectively, the structure becomes that in Fig. 3.2. Since the structure is symmetry, two secondary stages in Fig. 3.2 behave identically, like that of one monolithic workpiece. When a force F_Y along the Y-axis is exerted, the motion stage produces a linear displacement along the Y-axis. In the meanwhile, two secondary stages produce half of displacement along the Y-axis at the motion stage, and move slightly along the X-axis to nullify the axial load of the flexure hinges. No tensile or compressive axial loads of the flexure hinges means that no buckling and no stiffening occur. The deflection under the load of F_Y is illustrated in Fig. 3.2(b). This type of prismatic joint can be used as the fundamental module to configure large-motion flexure mechanisms.

This type of prismatic joint is not the same as that designed by Lobontiu [38] in Fig. 2.21. The differences are the input and output stages. As shown in Fig. 2.21, the input forces are exerted on the lateral stages, and the output displacement is generated from the central upper stage. Differently, the new type of prismatic joint has the same input and output stage.

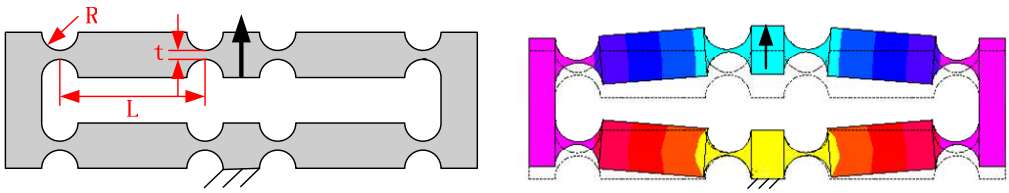

(a) Structure (b) Deformation

Figure 3.2: New large-motion prismatic joint

3.3 Structure Synthesis of Decoupled *XYZ*-FPMs

3.3.1 Preliminary of Screw Theory

As mentioned in Section 2.3, the general methods previously used for structure synthesis can be divided into two types, the constraint synthesis approach based on the screw theory [40, 41, 40, 42, 43, 44], and the Lie sub-group approach based on the algebraic properties of a Lie group of the Euclidean displacement set [45, 46, 47]. The screw theory is selected as the method of structure synthesis of decoupled *XYZ*-FPMs. The fundamental of the screw theory is briefly introduced.

A screw is represented as

$$\$ = \begin{cases} \left[\begin{array}{c} s \\ r \times s + hs \end{array} \right] & \text{if h is not infinite} \\ \left[\begin{array}{c} 0 \\ s \end{array} \right] & \text{if } h = \infty \\ \left[\begin{array}{c} s \\ r \times s \end{array} \right] & \text{if } h = 0 \end{cases}, \tag{3.1}$$

where s is an unit vector along the axis of the screw \$, r is the vector directed from any point on the axis of the screw to the origin of the reference frame O-*XYZ*, and h is a scaler which is the pitch of the screw. When h is zero, the unit screw is associated with a revolute joint or a force, and is given by $\$ = (s,\ s \times r) = (l\,m\,n\,;\,a\,b\,c)$. When h is infinite, the unit screw is associated with a prismatic joint or a moment, and is given by $\$ = (0\,;s) = (0\,0\,0\,;\,l\,m\,n)$ [83].

A screw \$, is called as a twist, if the first vector represents the instant angular velocity and the second vector represents the linear velocity. A screw \$, is called as a wrench, if the first vector represents the resultant force and the second vector represents the moment. ξ_0, ξ_∞, ζ_0 and ζ_∞ are used to represent a twist of 0-pitch, a twist of ∞-pitch, a

wrench of 0-pitch and a wrench of ∞-pitch. Physically, they represent an allowed rotary motion, an allowed translational motion, an constrained translational motion and an constrained rotary motion.

An m order screw system is associated with a reciprocal $(6-m)$ screw system. The twist system of a kinematic connection represents all motions by the connection in a given position. The wrench system of the connection represents all constraints that can be transmitted by the connection. The twist system and the wrench system of the connection are uniquely related by reciprocity [77, 83, 84].

The twist system of two connections acting in series is the combination of the systems of the individual connection. The twist system of two connections acting in parallel is the intersection of the systems of the individual connection. The reciprocal system, i.e., the wrench system of two connections acting in series, is the intersection of the reciprocal systems of the individual connection. The reciprocal systems of multi-connection acting in parallel is the combination of the reciprocal system of the individual connection [83].

For a parallel manipulator, the end-effector is constrained by several limbs, i.e., its DOF is determined by the combination of all the contact wrenches. The constraint-synthesis method proposed by Huang [40] is based on this theory.

3.3.2 General Procedure of Structure Synthesis of Decoupled *XYZ*-FPMs

According to the screw theory briefly introduced above, in any general configuration, the twist system of the *XYZ*-FPM is a 3-ξ_∞-system. Since the virtual power developed by any ζ_∞ along any twist within the 3-ξ_∞-system is zero, the wrench system of the *XYZ*-FPM is thus a 3-ζ_∞-system. As the wrench system of a parallel kinematic structure is the linear combination of those of all its legs in any configuration, it is then concluded that the wrench system of any leg in a parallel kinematic structure is a c^i $(0 \leq c^i \leq 3)$-ζ_∞-system in any general configuration.

In Pham's thesis [85], the concept of the selective-actuation mechanism is proposed. The selective-actuation mechanism is defined as a mechanism possessing a diagonal-form

Jacobian matrix. That means that a mechanism is considered as a selective-actuation mechanism when the infinitesimal end-effector motion along every DOF is driven by only one specified actuator. The stiffness matrices of selective-actuation mechanisms are diagonal. Based on the concept, the structures of the decoupled *XYZ*-FPMs are designed to be the parallel combinations of three limbs in orthogonal configuration.

Thus, the general procedure of structure synthesis of the decoupled *XYZ*-FPMs can be summarized as follows.

- Step 1: Perform structure synthesis of the 3-ζ_∞-system kinematic limbs.
- Step 2: Generate the decoupled *XYZ*-FPMs using the kinematic limbs in Step 1.
- Step 3: Check the mobilities of the decoupled *XYZ*-FPMs.

3.3.3 Structure Synthesis of Kinematic Limbs

The kinematic limbs of the decoupled *XYZ*-FPMs should satisfy the following conditions.

1. The wrench system of the kinematic limb is a c^i ($0 \leq c^i \leq 3$)-ζ_∞-system.
2. The kinematic limb possesses at least one prismatic joint, and one prismatic joint closely connected to the base is actuated by the linear actuator.
3. All the lengthwise axes of flexure hinges are not collinear with or parallel to the actuation axis, in order to avoid stiffening and buckling.

Table 3.1 lists the kinematic limbs satisfying the above conditions. The structures of the kinematic limbs are shown in Fig. 3.3. Among the synthesized kinematic limbs, all the axes of the prismatic joints are perpendicular to each another. The kinematic limbs of PPRR and PRRP are prone to the problem of stiffening. Thus, the kinematic limbs of PPP, PRRR, PPRRR and PRRRP are adopted to configure the decoupled *XYZ*-FPMs.

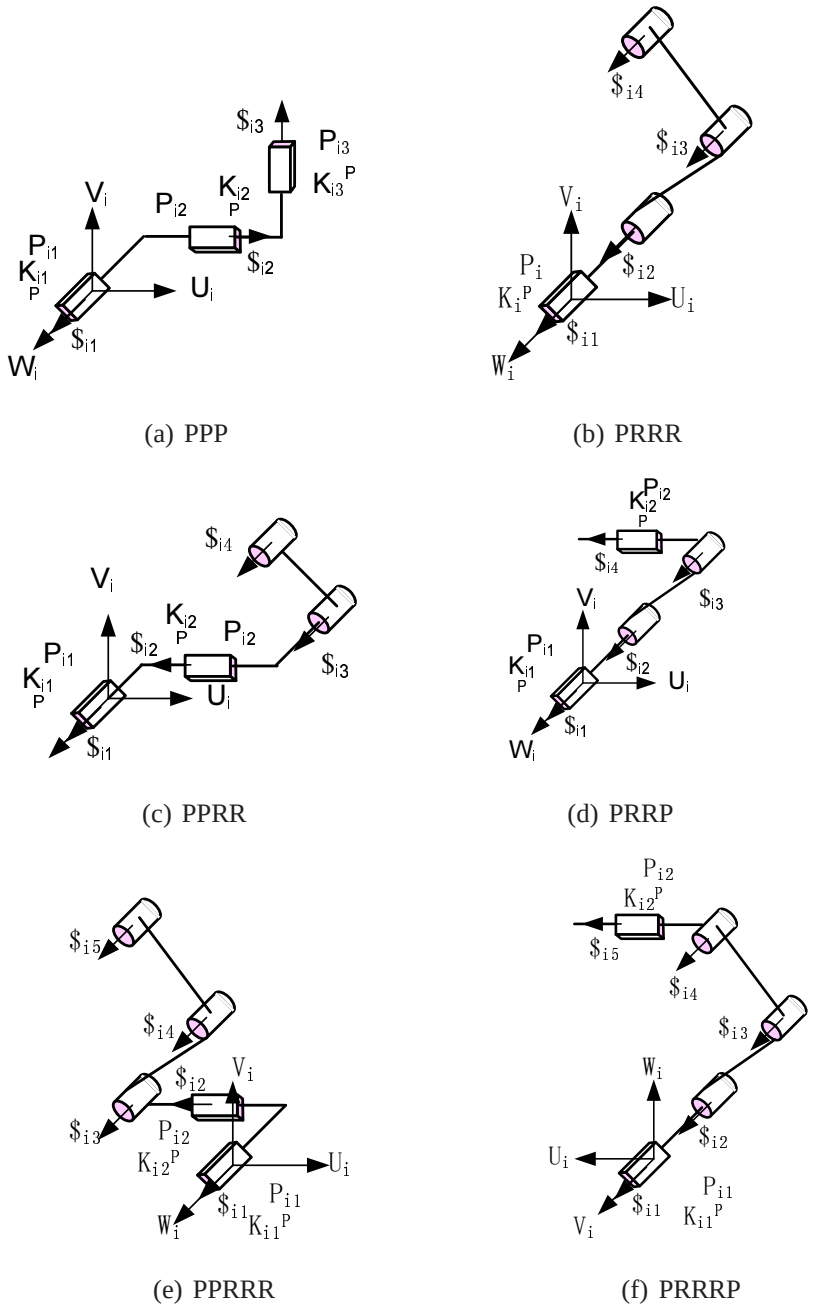

(a) PPP (b) PRRR

(c) PPRR (d) PRRP

(e) PPRRR (f) PRRRP

Figure 3.3: Kinematic limbs

Table 3.1: Kinematic limbs with a c^i-ζ_∞-system

C^i	Limb type	Geometric conditions
3	PPP	Three axes of three prismatic joints are perpendicular to each another.
2	PRRR	The axis of the prismatic joint is perpendicular to the plane of RRR-
	PPRR	-limb. The axes of the prismatic joints are perpendicular to each another.
	PRRP	The lengthwise axis of the revolute joint is not collinear with or parallel
1	PPRR	to the actuation axis.
	PRRRP	

3.3.4 Enumeration and Mobility Analysis of Decoupled *XYZ*-FPMs

The kinematic limbs have been synthesized in the previous section. In this section, the decoupled *XYZ*-FPMs are configured based on the above limbs.

The 3-PPRRR (shown in Fig. 3.4(b)) 3-PRRRP (shown in Fig. 3.4(c)), 3-PPP (shown in Fig. 3.4(d)) and 3-PRRR (shown in Fig. 3.4(a)) configurations are proposed. In the synthesized decoupled *XYZ*-FPMs, two fundamental components, i.e., the prismatic joint designed in Section 3.2 and the RRR-limb shown in Fig. 3.5, are used to configure the *XYZ*-FPMs. The flexure hinges used in the prismatic joint and the RRR-limb are the same, the single-axis circular type shown in Fig. 2.1(b). As addressed in Section 2.1.2, the single-axis flexure hinges include the leaf spring, the circular, the conic-section and the corner-fillet types. The circular type is selected because of the following three reasons. The first reason is that the circular flexure hinge has a large stiffness ratio of the nonsensitive-axis to the sensitive-axis, which means small parasitic motion of flexure mechanisms. The second reason is easy manufacturing. The common manufacturing method of flexure mechanisms is EDM. The geometric accuracy of the circular notch hinge can be easily and precisely achieved by the current EDM technique. The third reason is possibility of exact modeling. Besides the leaf spring type, the circular type is easier to be exactly modeled than others such as the conic-section and corner-fillet types.

To avoid the phenomena of stiffening and buckling, the RRR-limb is under the following

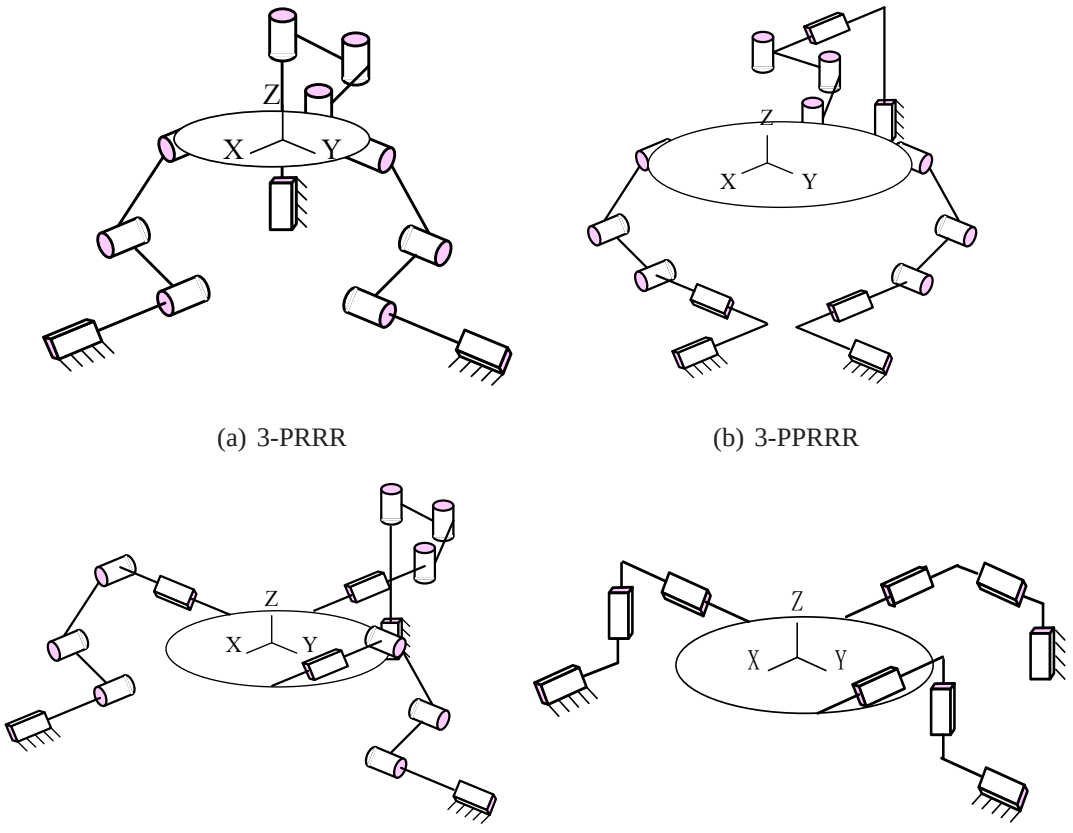

(a) 3-PRRR (b) 3-PPRRR

(c) 3-PRRRP (d) 3-PPP

Figure 3.4: Structures of decoupled *XYZ*-FPMs

constraint. In Fig. 3.5, if the desired translational motions at the end-effector of the combined 3-limb mechanism are along the U_i-, V_i- and W_i-axes, the lengthwise axis, i.e., the l_i-axis, in the local coordinate of the flexure hinge should not be parallel to any of the U_i-, V_i- and W_i-axes.

The first configuration is the 3-PPP structure. Since a PPP-limb constrains all the rotations about the three axes, and the constrained motions of the 3-PPP *XYZ*-FPM are all the rotations, which are the combination of those of each limb. It means that the end-effector, the intersection point of the three limbs, can achieve the three translational motions.

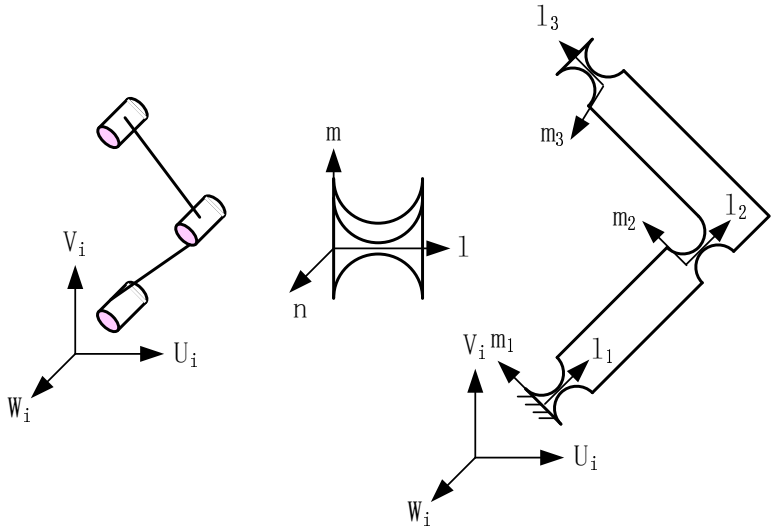

Figure 3.5: RRR limb

The second configuration is the 3-PRRR structure, shown in Fig. 3.3(b). The twist system of the PRRR-limb in the $U_i - V_i - W_i$ coordinate can be represented as

$$\begin{aligned}
\$_{i1} &= (\,0,\,0,\,0\,;\,0,\,0,\,n_1\,),\\
\$_{i2} &= (\,0,\,1,\,0\,;\,0,\,0,\,c_2\,),\\
\$_{i3} &= (\,0,\,1,\,0\,;\,a_3,\,b_3,\,c_3\,),\\
\$_{i2} &= (\,0,\,1,\,0\,;\,a_4,\,b_4,\,c_4\,).
\end{aligned}$$

The constraint system of Limb i is

$$\begin{aligned}
\$^r_{i1} &= (\,0,\,0,\,0\,;\,1,\,0,\,0\,),\\
\$^r_{i2} &= (\,0,\,0,\,0\,;\,0,\,0,\,1\,).
\end{aligned}$$

It means that in the $U_i - V_i - W_i$ coordinate, the rotary motions about the U_i- and W_i-axes of Limb i are constrained. The constrained rotary motions of each PRRR-limb can be given as

$$\begin{aligned}
i &= 1, \quad (U_1,\,V_1,\,W_1) = (X,\,Y,\,Z), \quad \theta_X\theta_Z,\\
i &= 2, \quad (U_2,\,V_2,\,W_2) = (Y,\,Z,\,X), \quad \theta_Y\theta_X,\\
i &= 3, \quad (U_3,\,V_3,\,W_3) = (Y,\,Z,\,X), \quad \theta_Y\theta_X.
\end{aligned}$$

The constrained motions of the 3-PRRR *XYZ*-FPM are the combination of those of each PRRR-limb

$$(\theta_X,\,\theta_Z) \cup (\theta_Y,\,\theta_X) \cup (\theta_Y,\,\theta_X) = (\theta_X,\,\theta_Y,\,\theta_Z).$$

Thus, the end-effector of the 3-PRRR *XYZ*-FPM can achieve the three translational motions.

The third configuration is the 3-PPRRR structure. The twist system of the PPRRR-limb in Fig. 3.3(e) can be given as

$$\begin{aligned}
\$_{i1} &= (\,0,\,0,\,0\,;\,0,\,0,\,n_1\,),\\
\$_{i2} &= (\,0,\,0,\,0\,;\,l_2,\,m_2,\,0\,),\\
\$_{i3} &= (\,0,\,1,\,0\,;\,a_3,\,b_3,\,0\,),\\
\$_{i4} &= (\,0,\,1,\,0\,;\,a_4,\,b_4,\,c_4\,),\\
\$_{i5} &= (\,0,\,1,\,0\,;\,a_5,\,b_5,\,c_5\,).
\end{aligned}$$

The constraint system of Limb i is

$$\begin{aligned}
\$^r_{i1} &= (\,0,\,0,\,0\,;\,1,\,0,\,0\,),\\
\$^r_{i2} &= (\,0,\,0,\,0\,;\,0,\,0,\,1\,).
\end{aligned}$$

The constrained rotary motions of each PPRRR-limb can be given as

$$\begin{aligned}
i &= 1, \quad (U_1,\,V_1,\,W_1) = (X,\,Y,\,Z), \quad \theta_X\theta_Z,\\
i &= 2, \quad (U_2,\,V_2,\,W_2) = (Y,\,Z,\,X), \quad \theta_Y\theta_X,\\
i &= 3, \quad (U_3,\,V_3,\,W_3) = (Y,\,Z,\,X), \quad \theta_Y\theta_X.
\end{aligned}$$

The constrained motions of the 3-PPRRR *XYZ*-FPM are the combination of those of each PPRRR-limb

$$(\theta_X,\,\theta_Z) \cup (\theta_Y,\,\theta_X) \cup (\theta_Y,\,\theta_X) = (\theta_X,\,\theta_Y,\,\theta_Z).$$

The forth configuration is the 3-PRRRP structure. The twist system of the PRRRP-limb in Fig. 3.3(f) can be given as

$$\begin{aligned}
\$_{i1} &= (\,0,\,0,\,0\,;\,0,\,0,\,n_1\,),\\
\$_{i2} &= (\,0,\,1,\,0\,;\,0,\,0,\,c_2\,),\\
\$_{i3} &= (\,0,\,1,\,0\,;\,a_3,\,b_3,\,c_3\,),\\
\$_{i4} &= (\,0,\,1,\,0\,;\,a_4,\,b_4,\,c_4\,),\\
\$_{i5} &= (\,0,\,0,\,0\,;\,l_5,\,m_5,\,n_5\,).
\end{aligned}$$

The constraint system of Limb i is

$$\begin{aligned} \$_{i1}^{r} &= (0,\,0,\,0\,;\,1,\,0,\,0), \\ \$_{i2}^{r} &= (0,\,0,\,0\,;\,0,\,0,\,1). \end{aligned}$$

The constrained rotary motions of each PRRRP-limb can be given as

$$\begin{aligned} i &= 1, \quad (U_1,\,V_1,\,W_1) = (X,\,Y,\,Z), \quad \theta_X\theta_Z, \\ i &= 2, \quad (U_2,\,V_2,\,W_2) = (Y,\,Z,\,X), \quad \theta_Y\theta_X, \\ i &= 3, \quad (U_3,\,V_3,\,W_3) = (Y,\,Z,\,X), \quad \theta_Y\theta_X. \end{aligned}$$

The constrained motions of the 3-PRRRP *XYZ*-FPM are the combination of those of each PRRRP-limb

$$(\theta_X,\,\theta_Z) \cup (\theta_Y,\,\theta_X) \cup (\theta_Y,\,\theta_X) = (\theta_X,\,\theta_Y,\,\theta_Z).$$

For each type of limb, the three identical limbs are arranged orthogonally and intersect at the end-effector. The structures of the decoupled *XYZ*-FPMs are shown in Fig. 3.4.

3.4 Summary

This chapter has studied the differences between flexure mechanisms and rigid-body mechanisms, in the aspects of available joint type, actuation joint, manufacturing, buckling and stiffening. These differences make structure synthesis of flexure mechanisms different from that of rigid-body mechanisms. The differences have been summarized as the structure constraints of structure synthesis of flexure mechanisms. Structure synthesis of the decoupled *XYZ*-FPMs is especially studied in this chapter. With the consideration of the structure constraints, the kinematic limbs of the decoupled *XYZ*-FPMs are synthesized. The decoupled *XYZ*-FPMs are enumerated, and their mobilities are analyzed. As the fundamental component of flexure mechanisms, a new type of large-motion prismatic joint has also been designed, with the advantages of no parasitic motion, no buckling, no stiffening and geometric symmetry.

Chapter 4

Modeling of Synthesized *XYZ*-FPMs

Modeling ia another important issue for study and development of flexure mechanisms, besides structure design. An exact model is critical to design, evaluate and control flexure mechanisms. Flexure hinges require an exact modeling method, and entire flexure mechanisms also require an exact modeling method to describe their static and dynamic behaviors. This chapter addresses the modeling issue of flexure mechanisms. Section 4.1 proposes an exact modeling method to formulate the static and dynamic behaviors of the new prismatic joint designed in Chapter 3, based on the continuous-compliance assumption. The exact stiffness model of the RRR-limb is formulated in Section 4.2, based on the study on the compliances of flexure hinges by Lobontiu [16]. Since the new prismatic joint and the RRR-limb are the fundamental components of the *XYZ*-FPMs synthesized in the previous chapter, the exact stiffness matrices of the *XYZ*-FPMs are given in Section 4.3, based on the compliance formulations of the prismatic joint in Section 4.1 and the RRR-limb in Section 4.2.

4.1 Modeling of Prismatic Joint

4.1.1 Necessity of Exact Modeling

Before introduction of the proposed exact modeling method, necessity of exact modeling is explained here. The current modeling methods can be categorized into two types, i.e.,

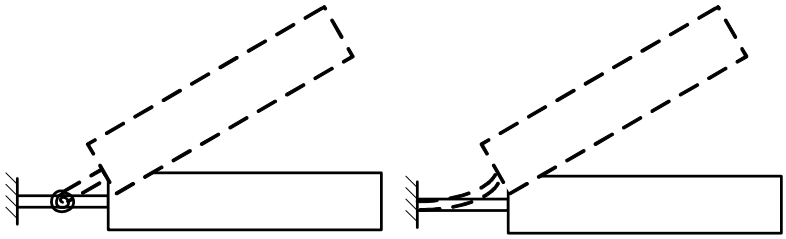

(a) PRB approximation (b) Actual deformation

Figure 4.1: Comparison between PRB approximation and actual deformation

the lumped-compliance method and the continuous-compliance method. The lumped-compliance approach assumes that the flexible components are the flexure hinges, and the connection links are rigid. The continuous-compliance approach assumes that both the flexure hinges and the connection links are flexible. The study on the compliances of flexure hinges by Lobontiu [16] is under the assumption of the lumped-compliance approach. Lobontiu has formulated the exact compliance matrices of flexure hinges, and the stiffness models of entire flexure mechanisms can be derived, based on the lumped-compliance assumption. The drawback of this approach is that it is limited in modeling of the static behaviors of entire flexure mechanisms, such as the stiffness, and the dynamic behaviors of entire flexure mechanisms cannot be obtained.

Another common lumped-compliance approach is the PRB method. The PRB method can be used to describe the static and dynamic behaviors of entire flexure mechanisms. However, the PRB approach is an approximate method for analytical formulations. There are mainly two reasons to explain that.

First, in the PRB theory, the flexure hinge is treated as a center-fixed revolute joint (shown in Fig. 4.1(a)) with the constant angular stiffness when no axial load exists, and the connection link between the centers of every two notch hinges is regarded as rigid limb. Such approximation may lead to the stiffness error. Actually, the notch hinge deforms more like an end-fixed beam than a center-fixed revolute joint (shown in Fig. 4.1(b)).

Second, in the PRB theory, the potential energy is deemed to be caused by deformation of the flexure hinge, and the kinetic energy to be from the rigid motion of the connection link. Such approximation will introduce the mass error. Actually, the flexure hinge also contributes to the kinetic energy, especially when the mass of the flexure hinge is not

negligible compared to that of the connection link.

Therefore, an exact modeling method is proposed for modeling of both the stiffness and dynamic equations. In this method, both flexure hinges and connection links are regarded as deformable beams. The method is based on the continuous-compliance assumption. Deformation of each part is exactly represented with nonlinear integral equations.

In the previous chapter, a new type of large-motion prismatic joint has been designed (shown in Fig. 3.2), and used to configure the large-motion and decoupled *XYZ*-FPMs. In this section, the exact modeling method for this type of prismatic joint is introduced, to formulate the statics and dynamic equations. This method can also be used to model the large-motion prismatic joints in Fig. 2.19(b) and Fig. 2.19(c). The prismatic joint can be regarded as an equivalent second-order system represented by the combination of a linear spring and a mass. The objective of all the modeling methods is to obtain the equivalent stiffness and mass.

4.1.2 Equivalent Stiffness Modeling of Prismatic Joint

As illustrated in Fig. 4.2(a), the prismatic joint consists of one motion stage, two secondary stages and four limbs. The motion stage and the secondary stages are regarded as rigid, and the limbs are treated as flexible. Each limb (shown in Fig. 4.2(b)) consists of three parts, two circular-flexure hinges (Part I and Part III) and one connection link (Part II). Points $P_0 \sim P_3$ are the ends of Part I $\sim$ Part III, respectively. When the force F is applied to the motion stage, the motion stage produces a linear displacement u without any parasitic motion, and the secondary stages produce half of the displacement $\frac{u}{2}$ at the motion stage. In the meanwhile, the secondary stages move a slight displacement δ perpendicular to the direction of F. The slight displacement δ nullifies the internal tensile force along the lengthwise axis of the limb. Moreover, there are no any rotations at the secondary stages. Limb 1 is connected to the ground at one end, and to the secondary stage at the other end. Limb 2 is connected to the secondary stage at one end, and to the motion stage at the other end. It can be seen that Limb 1 and Limb 2 are in serial and deform in the same manner. Limb 3 and Limb 4 are in parallel with Limb 1 and Limb 2, and deform in the same manner. Both of them deform to generate half of

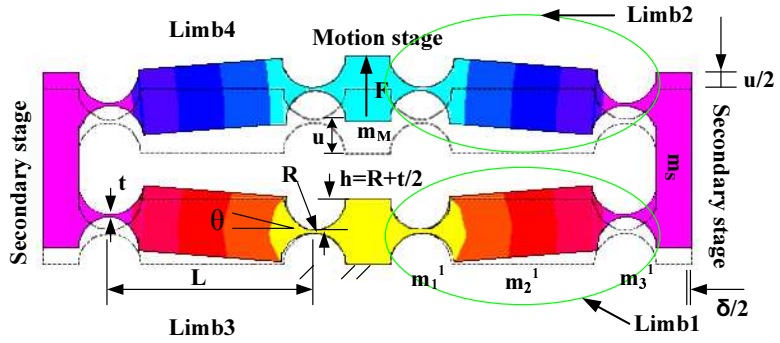

(a) Deformed prismatic joint

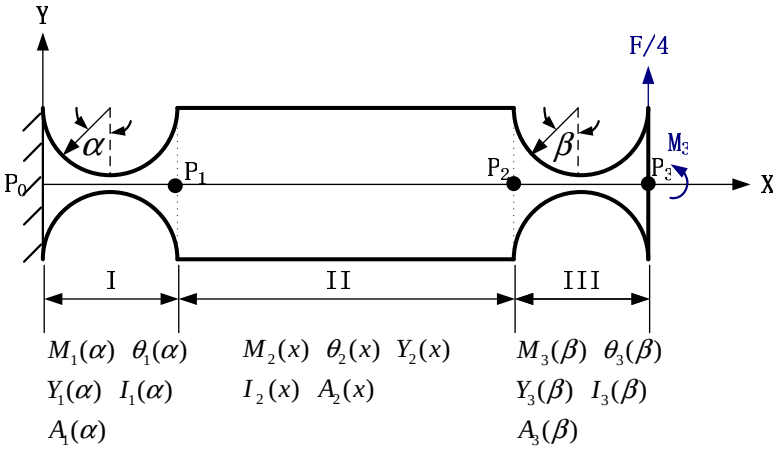

(b) One limb

Figure 4.2: Analysis of prismatic joint

the linear displacement $\frac{u}{2}$ at the motion stage. Therefore, each limb can be regarded as a fixed-end beam with the constraint of zero angular displacements in both ends, as shown in Fig. 4.2(b). When the force F is exerted on the motion stage, a quarter of the applied force, $\frac{F}{4}$, is distributed on each limb, as shown in Fig. 4.2(b). At the same time, an internal moment M_3 is generated because of the constraint of zero angular displacement at the point P_3.

Each limb is divided into three portions, Part I, Part II and Part III. Each portion is regarded to possess the continuous-compliance. For each portion, the moments of inertia $I_1(\alpha)$, $I_2(x)$ and $I_3(\beta)$ are,

$$I_1(\alpha) = \frac{2b(h - R\cos\alpha)^3}{3} \qquad -\frac{\pi}{2} \le \alpha \le \frac{\pi}{2}, \tag{4.1}$$

$$I_2(x) = \frac{bh^3}{12}, \tag{4.2}$$

$$I_3(\beta) = \frac{2b(h - R\cos\beta)^3}{3} \qquad -\frac{\pi}{2} \le \beta \le \frac{\pi}{2}. \tag{4.3}$$

The moments $M_1(\alpha)$, $M_2(x)$ and $M_3(\beta)$ are,

$$M_1(\alpha) = \frac{F(L + R - R\sin\alpha)}{4} + M_3 \qquad -\frac{\pi}{2} \le \alpha \le \frac{\pi}{2}, \tag{4.4}$$

$$M_2(x) = \frac{F(L + 2R - x)}{4} + M_3 \qquad 2R \le x \le L + 2R, \tag{4.5}$$

$$M_3(\beta) = \frac{F(R - R\sin\beta)}{4} + M_3 \qquad -\frac{\pi}{2} \le \beta \le \frac{\pi}{2}. \tag{4.6}$$

Thus, the angular displacements can be calculated as

$$\theta_1(\alpha) = \int \frac{M_1(\alpha)}{EI_1(\alpha)} R\cos\alpha d\alpha, \tag{4.7}$$

$$\theta_2(x) = \int \frac{M_2(x)}{EI_2(x)} dx, \tag{4.8}$$

$$\theta_3(\beta) = \int \frac{M_3(\beta)}{EI_3(\beta)} R\cos\beta d\beta, \tag{4.9}$$

where E is the Young's modulus. No angular deformations are generated at the two ends of the beam in Fig. 4.2(b), and the three portions in one limb are connected continuously. Thus, the constraints can be represented as

$$\theta_1(-\frac{\pi}{2}) = 0, \tag{4.10}$$

$$\theta_2(2R) = \theta_1(\frac{\pi}{2}), \tag{4.11}$$

$$\theta_3(-\frac{\pi}{2}) = \theta_2(L), \tag{4.12}$$

$$\theta_3(\frac{\pi}{2}) = 0. \tag{4.13}$$

By solving equations (4.10) to (4.13), the internal moment M_3 can be obtained as

$$M_3 = -FR/4. \tag{4.14}$$

By substituting (4.14) into equations (4.7) to (4.9), and integrating equations (4.7) to (4.9), the linear displacements and the constraints can be represented as

$$\begin{aligned}
Y_1(\alpha) &= \int \theta_1(\alpha) R\cos\alpha d\alpha, && (4.15)\\
Y_1(-\frac{\pi}{2}) &= 0, && (4.16)\\
Y_2(x) &= \int \theta_2(x) dx, && (4.17)\\
Y_2(2R) &= Y_1(\frac{\pi}{2}), && (4.18)\\
Y_3(\beta) &= \int \theta_3(\beta) R\cos\beta d\beta, && (4.19)\\
Y_3(-\frac{\pi}{2}) &= Y_2(L). && (4.20)
\end{aligned}$$

By solving equations (4.15) to (4.20), the linear displacement $Y_3(\frac{\pi}{2})$ at P_3 can be obtained, and the linear stiffness of the single limb can be calculated as

$$K_{Y-F_Y} = \frac{F/4}{Y_3(\frac{\pi}{2})}, \tag{4.21}$$

The equivalent linear stiffness of the prismatic joint is identical to that of the single limb

$$K^P = K_{Y-F_Y}. \tag{4.22}$$

4.1.3 Equivalent Mass Modeling of Prismatic Joint

After calculation of the equivalent linear stiffness of the prismatic joint, the equivalent mass needs to be formulated. Under the assumption that the mass is continuously distributed in both the flexure hinges and the connection links, the kinetic energy of the

prismatic joint can be calculated as

$$\begin{aligned} T &= \int_{\frac{-\pi}{2}}^{\frac{\pi}{2}} \rho A_1(\alpha)(\frac{d(Y_1(\alpha))}{dt})^2 R\cos\alpha d\alpha \\ &+ \int_{2R}^{L} \rho A_2(x)(\frac{d(Y_2(x))}{dt})^2 dx \\ &+ \int_{\frac{-\pi}{2}}^{\frac{\pi}{2}} \rho A_3(\beta)(\frac{d(Y_3(\beta))}{dt})^2 R\cos\beta d\beta \\ &+ (m_1^1 + m_2^1 + m_3^1 + m_S)(\frac{d(Y_3(\frac{\pi}{2}))}{dt})^2 \\ &+ \frac{1}{2} m_M (\frac{d(2Y_3(\frac{\pi}{2}))}{dt})^2, \end{aligned} \tag{4.23}$$

where ρ is the density. The cross-section areas $A_1(\alpha)$, $A_2(x)$ and $A_3(\beta)$ at any points of the three parts are

$$A_1(\alpha) = 2(h - R\cos\alpha)b \qquad -\frac{\pi}{2} \le \alpha \le \frac{\pi}{2}, \tag{4.24}$$

$$A_2(x) = 2hb, \tag{4.25}$$

$$A_3(\beta) = 2(h - R\cos\beta)b \qquad -\frac{\pi}{2} \le \beta \le \frac{\pi}{2}. \tag{4.26}$$

Therefore, the equivalent mass of the prismatic joint is

$$M_V^* = \frac{T}{2(\frac{d(Y_3(\frac{\pi}{2}))}{dt})^2}. \tag{4.27}$$

4.1.4 Dynamic Modeling of Prismatic Joint

As mentioned above, in physical sense, the prismatic joint are equivalent to a second-order system with a linear spring and a mass. The objectives of all the modeling methods are to obtain the equivalent stiffness and the equivalent mass of the equivalent second-order system. Using the proposed exact modeling method in this section, the equivalent stiffness and the equivalent mass of the new prismatic joint designed in the previous chapter have been formulated. Thus, the dynamic behavior of the prismatic joint can be represented as,

$$F = M_v^* \ddot{Y} + K^P Y. \tag{4.28}$$

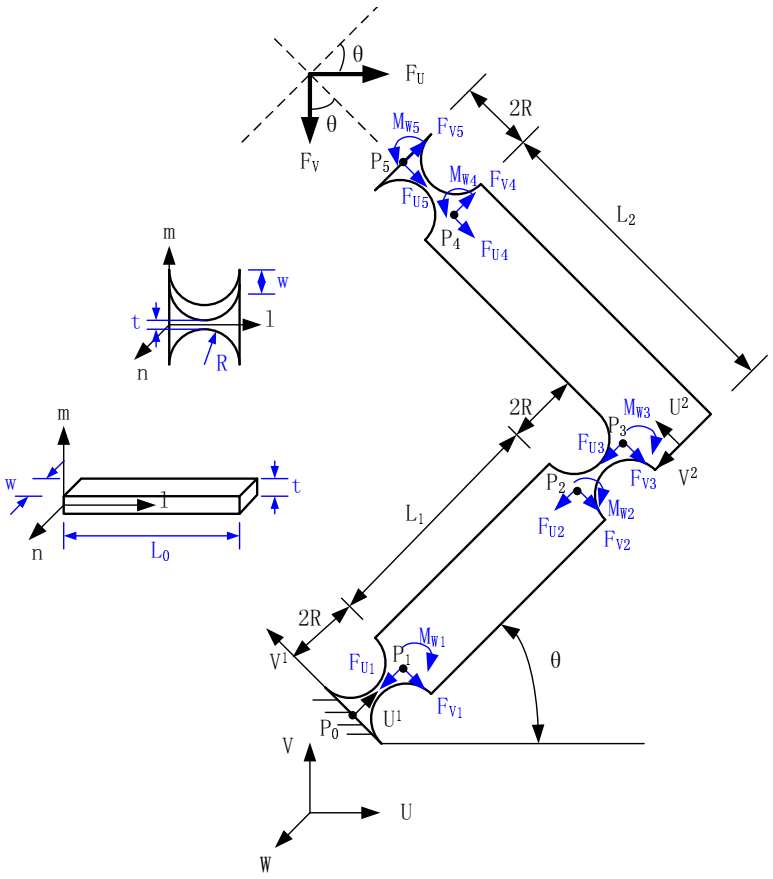

Figure 4.3: RRR-limb

4.2 Stiffness Modeling of RRR-Limb

The stiffness modeling of the RRR-limb is based on the lumped-compliance assumption. The compliance is regarded to exist in the flexure hinges, and the exact compliance matrices of the flexure hinges have been formulated by Lobontiu [16]. Based on the Lobontiu's study, the exact compliance matrices of the RRR-limb is derived in this section. The RRR-limb is illustrated in Fig. 4.3. The two links in the RRR-limb are designed to be perpendicular to each other. When the external forces F_U and F_V are applied on the tip of the limb, the loads at the node P_1 inside the limb can be given as

$$F_{U1} = -F_U \cos\theta + F_V \sin\theta, \tag{4.29}$$

$$F_{V1} = F_U \sin\theta + F_V \cos\theta, \tag{4.30}$$

$$M_{W1} = (6R + L_1 + L_2)(F_U \sin\theta + F_V \cos\theta) - M_{W5}. \tag{4.31}$$

The displacements at P_1 under the above loads can be represented in the local coordinate of $U^1 - V^1 - W^1$ as

$$\begin{bmatrix} u_{U1} \\ u_{V1} \\ \theta_{W1} \end{bmatrix} = \begin{bmatrix} C^R_{l-F_l} & 0 & 0 \\ 0 & C^R_{m-F_m} & C^R_{m-M_n} \\ 0 & C^R_{\theta_n-F_m} & C^R_{\theta_n-M_n} \end{bmatrix} \begin{bmatrix} F_{U1} \\ F_{V1} \\ M_{W1} \end{bmatrix}. \tag{4.32}$$

The 3×3 matrix describes the exact compliances of the circular-flexure hinge in its local coordinate of $l - m - n$, studied by Lobontiu [16],

$$C^R_{l-F_l} = \frac{1}{Ew}\left[\frac{2(2R+t)}{\sqrt{t(4R+t)}} \arctan\sqrt{1+\frac{4R}{t}} - \frac{\pi}{2}\right], \tag{4.33}$$

$$\begin{aligned} C^R_{m-F_m} = {} & \frac{3}{4Ew(2R+t)}\{2(2+\pi)R + \pi r + \frac{8R^3(44R^2+28Rt+5t^2)}{t^2(4R+t)^2} \\ & + \frac{(2R+t)\sqrt{t(4R+t)}[-80R^4+24R^3t+8(3+2\pi)R^2t^2]}{\sqrt{t^5(4R+t)^5}} \\ & + \frac{(2R+t)\sqrt{t(4R+t)}[4(1+2\pi)Rt^3+\pi t^4]}{\sqrt{t^5(4R+t)^5}} \\ & - \frac{8(2R+t)^4(-6R^2+4Rt+t^2)}{\sqrt{t^5(4R+t)^5}} \arctan\sqrt{1+\frac{4R}{t}}\}, \end{aligned} \tag{4.34}$$

$$C^R_{m-M_n} = C^R_{\theta_n-F_m} = \frac{24R^2}{Ewt^3(2R+t)(4R+t)^3}[t(4R+t)(6R^2+4Rt+t^2) + 6R(2R_t)^2\sqrt{t(4R+t)}\arctan\sqrt{1+\frac{4R}{t}}], \quad (4.35)$$

$$C^R_{\theta_n-M_n} = \frac{C^R_{m-M_n}}{R}. \quad (4.36)$$

The local coordinate of $l-m-n$ in the first link is identical to that of $U^1-V^1-W^1$. The angular displacement at P_1 can be calculated as

$$\theta_{W1} = [C^R_{m-M_n} + C^R_{\theta_n-M_n}(6R+L_1+L_2)](F_U\sin\theta + F_V\cos\theta) - C^R_{\theta_n-M_n}M_{W5}. \quad (4.37)$$

Similarly, the loads at P_2 are

$$F_{U2} = -F_U\cos\theta + F_V\sin\theta, \quad (4.38)$$

$$F_{V2} = F_U\sin\theta + F_V\cos\theta, \quad (4.39)$$

$$M_{W2} = (4R+L_1+L_2)(F_U\sin\theta + F_V\cos\theta) - M_{W5}. \quad (4.40)$$

The displacements at P_2 can be represented in the local coordinate of $U^1-V^1-W^1$ as

$$\begin{bmatrix} u_{U2} \\ u_{V2} \\ \theta_{W2} \end{bmatrix} = \begin{bmatrix} C^L_{l-F_l} & 0 & 0 \\ 0 & C^L_{m-F_m} & C^L_{m-M_n} \\ 0 & C^L_{\theta_n-F_m} & C^L_{\theta_n-M_n} \end{bmatrix} \begin{bmatrix} F_{U2} \\ F_{V2} \\ M_{W2} \end{bmatrix}. \quad (4.41)$$

The above 3×3 matrix describes the exact compliances of the leaf spring in its local coordinate of $l-m-n$, also studied by Lobontiu [16],

$$C^L_{l-F_l} = \frac{L_0}{Ewt}, \quad (4.42)$$

$$C^L_{m-F_m} = \frac{4L_0^3}{Ewt^3}, \quad (4.43)$$

$$C^L_{m-M_m} = C^L_{\theta_n-F_m} = \frac{6L_0^2}{Ewt^3}, \quad (4.44)$$

$$C^L_{\theta_n-M_n} = \frac{12L_0}{Ewt^3}. \quad (4.45)$$

The angular displacement at P_2 can be calculated as

$$\theta_{W2} = [C^L_{m-M_n} + C^L_{\theta_n-M_n}(4R+L_1+L_2)](F_U\sin\theta + F_V\cos\theta) - C^L_{\theta_n-M_n}M_5. \quad (4.46)$$

The loads at P_3 are given as

$$F_{U3} = -F_U \cos\theta + F_V \sin\theta, \tag{4.47}$$

$$F_{V3} = F_U \sin\theta + F_V \cos\theta, \tag{4.48}$$

$$M_{W3} = (2R + L_1 + L_2)(F_U \sin\theta + F_V \cos\theta) - M_{W5}. \tag{4.49}$$

The displacements are

$$\begin{bmatrix} u_{U3} \\ u_{V3} \\ \theta_{W3} \end{bmatrix} = \begin{bmatrix} C^R_{l-F_l} & 0 & 0 \\ 0 & C^R_{m-F_m} & C^R_{m-M_n} \\ 0 & C^R_{\theta_n-F_m} & C^R_{\theta_n-M_n} \end{bmatrix} \begin{bmatrix} F_{U3} \\ F_{V3} \\ M_{W3} \end{bmatrix}. \tag{4.50}$$

The angular displacement at P_3 is

$$\theta_{W3} = [C^R_{m-M_n} + C^R_{\theta_n-M_n}(2R + L_1 + L_2)](F_U \sin\theta + F_V \cos\theta) - C^R_{\theta_n-M_n} M_5. \tag{4.51}$$

The loads at P_4 are given as

$$F_{U4} = F_U \sin\theta + F_V \cos\theta, \tag{4.52}$$

$$F_{V4} = F_U \cos\theta - F_V \sin\theta, \tag{4.53}$$

$$M_{W4} = 2R(-F_U \cos\theta + F_V \sin\theta) + M_{W5}. \tag{4.54}$$

The displacements are

$$\begin{bmatrix} u_{U4} \\ u_{V4} \\ \theta_{W4} \end{bmatrix} = \begin{bmatrix} C^L_{l-F_l} & 0 & 0 \\ 0 & C^L_{m-F_m} & C^L_{m-M_n} \\ 0 & C^L_{\theta_n-F_m} & C^L_{\theta_n-M_n} \end{bmatrix} \begin{bmatrix} F_{U4} \\ F_{V4} \\ M_{W4} \end{bmatrix}. \tag{4.55}$$

The $l - m - n$ coordinate of the 3×3 compliance matrix is the same as $U^1 - V^1 - W^1$.

The angular displacement at P_4 is

$$\theta_{W4} = (C^L_{m-M_n} - C^L_{\theta_n-M_n} 2R)(F_U \cos\theta - F_V \sin\theta) + C^L_{\theta_n-M_n} M_{W5}. \tag{4.56}$$

The loads at P_5, the tip of the limb, are

$$F_{U4} = F_U \sin\theta + F_V \cos\theta, \tag{4.57}$$

$$F_{V4} = F_U \cos\theta - F_V \sin\theta, \tag{4.58}$$

$$M_{W5} = M_{W5}. \tag{4.59}$$

The displacements are

$$\begin{bmatrix} u_{U5} \\ u_{V5} \\ \theta_{W5} \end{bmatrix} = \begin{bmatrix} C^R_{l-F_l} & 0 & 0 \\ 0 & C^R_{m-F_m} & C^R_{m-M_n} \\ 0 & C^R_{\theta_n-F_m} & C^R_{\theta_n-M_n} \end{bmatrix} \begin{bmatrix} F_{U5} \\ F_{V53} \\ M_{W5} \end{bmatrix}. \tag{4.60}$$

The angular displacement at the tip is

$$\theta_{W5} = C^R_{m-M_n}(F_U \cos\theta - F_V \sin\theta) + C^R_{\theta_n-M_n} M_{W5}. \tag{4.61}$$

The RRR-limb, the same as the prismatic joint, is a fundamental component to form the limb of the *XYZ*-FPM. Since the *XYZ*-FPMs synthesized in the previous chapter have 3-DOFs of the three translational motions, and all the rotations are constrained, the rotation at the tip of the RRR-limb is also constrained. Thus,

$$\begin{aligned} &\theta_{W1} + \theta_{W2} + \theta_{W3} - \theta_{W4} - \theta_{W5} = 0 \\ &[C^R_{m-M_n} + C^R_{\theta_n-M_n}(6R + L_1 + L_2)](F_U \sin\theta + F_V \cos\theta) - C^R_{\theta_n-M_n} M_{W5} + \\ &[C^L_{m-M_n} + C^L_{\theta_n-M_n}(4R + L_1 + L_2)](F_U \sin\theta + F_V \cos\theta) - C^L_{\theta_n-M_n} M_{W5} + \\ &[C^R_{m-M_n} + C^R_{\theta_n-M_n}(2R + L_1 + L_2)](F_U \sin\theta + F_V \cos\theta) - C^R_{\theta_n-M_n} M_{W5} - \\ &(C^L_{m-M_n} - C^L_{\theta_n-M_n} 2R)(F_U \cos\theta - F_V \sin\theta) - C^L_{\theta_n-M_n} M_{W5} - \\ &C^R_{m-M_n}(F_U \cos\theta - F_V \sin\theta) - C^R_{\theta_n-M_n} M_{W5} = 0. \end{aligned} \tag{4.62}$$

The internal moment M_{W5} can be solved from the above equation,

$$M_{W5} = A_1 F_U + A_2 F_V, \tag{4.63}$$

where

$$\begin{aligned} A_1 &= \{[C^R_{m-M_n} + C^R_{\theta_n-M_n}(6R+L_1+L_2)]\sin\theta \\ &+ [C^L_{m-M_n} + C^L_{\theta_n-M_n}(4R+L_1+L_2)]\sin\theta \\ &+ [C^R_{m-M_n} + C^R_{\theta_n-M_n}(2R+L_1+L_2)]\sin\theta \\ &- (C^L_{m-M_n} - C^L_{\theta_n-M_n}2R)\cos\theta \\ &- C^R_{m-M_n}\cos\theta\}/(3C^R_{\theta_n-M_n} + 2C^L_{\theta_n-M_n}), \end{aligned} \tag{4.64}$$

$$\begin{aligned} A_2 &= \{[C^R_{m-M_n} + C^R_{\theta_n-M_n}(6R+L_1+L_2)]\cos\theta \\ &+ [C^L_{m-M_n} + C^L_{\theta_n-M_n}(4R+L_1+L_2)]\cos\theta \\ &+ [C^R_{m-M_n} + C^R_{\theta_n-M_n}(2R+L_1+L_2)]\cos\theta \\ &+ (C^L_{m-M_n} - C^L_{\theta_n-M_n}2R)\sin\theta \\ &+ C^R_{m-M_n}\sin\theta\}/(3C^R_{\theta_n-M_n} + 2C^L_{\theta_n-M_n}). \end{aligned} \tag{4.65}$$

Substituting M_{W5} into (4.4), the translational displacements at P_1 can be rewritten as

$$\begin{bmatrix} u_{U1} \\ u_{V1} \end{bmatrix} = \begin{bmatrix} C^R_{l-F_l} & 0 & 0 \\ 0 & C^R_{m-F_m} & C^R_{m-M_n} \end{bmatrix} \begin{bmatrix} -\cos\theta & \sin\theta \\ \sin\theta & \cos\theta \\ A_3 & A_4 \end{bmatrix} \begin{bmatrix} F_U \\ F_V \end{bmatrix}, \tag{4.66}$$

$$\theta_{W1} = C^R_{m-M_n}(\sin\theta F_U + \cos\theta F_V) + C^R_{\theta_n-M_n}(A_3F_U + A_4F_V), \tag{4.67}$$

where

$$A_3 = (6R+L_1+L_2)\sin\theta - A_1, \tag{4.68}$$

$$A_4 = (6R+L_1+L_2)\cos\theta - A_2. \tag{4.69}$$

At P_2,

$$\begin{bmatrix} u_{U2} \\ u_{V2} \end{bmatrix} = \begin{bmatrix} C^L_{l-F_l} & 0 & 0 \\ 0 & C^L_{m-F_m} & C^L_{m-M_n} \end{bmatrix} \begin{bmatrix} -\cos\theta & \sin\theta \\ \sin\theta & \cos\theta \\ A_5 & A_6 \end{bmatrix} \begin{bmatrix} F_U \\ F_V \end{bmatrix}, \tag{4.70}$$

where

$$\theta_{W2} = C^L_{m-M_n}(\sin\theta F_U + \cos\theta F_V) + C^L_{\theta_n-M_n}(A_5F_U + A_6F_V), \tag{4.71}$$

$$A_5 = (4R + L_1 + L_2)\sin\theta - A_1, \tag{4.72}$$

$$A_6 = (4R + L_1 + L_2)\cos\theta - A_2. \tag{4.73}$$

At P_3,

$$\begin{bmatrix} u_{U3} \\ u_{V3} \end{bmatrix} = \begin{bmatrix} C^R_{l-F_l} & 0 & 0 \\ 0 & C^R_{m-F_m} & C^R_{m-M_n} \end{bmatrix} \begin{bmatrix} -\cos\theta & \sin\theta \\ \sin\theta & \cos\theta \\ A_7 & A_8 \end{bmatrix} \begin{bmatrix} F_U \\ F_V \end{bmatrix}, \tag{4.74}$$

$$\theta_{W3} = C^R_{m-M_n}(\sin\theta F_U + \cos\theta F_V) + C^R_{\theta_n - M_n}(A_7 F_U + A_8 F_V), \tag{4.75}$$

where

$$A_7 = (2R + L_1 + L_2)\sin\theta - A_1, \tag{4.76}$$

$$A_8 = (2R + L_1 + L_2)\cos\theta - A_2. \tag{4.77}$$

At P_4,

$$\begin{bmatrix} u_{U4} \\ u_{V4} \end{bmatrix} = \begin{bmatrix} C^L_{l-F_l} & 0 & 0 \\ 0 & C^L_{m-F_m} & C^L_{m-M_n} \end{bmatrix} \begin{bmatrix} \sin\theta & \cos\theta \\ \cos\theta & \sin\theta \\ A_9 & A_{10} \end{bmatrix} \begin{bmatrix} F_U \\ F_V \end{bmatrix}, \tag{4.78}$$

$$\theta_{W4} = C^L_{m-M_n}(\cos\theta F_U + \sin\theta F_V) + C^L_{\theta_n - M_n}(A_9 F_U + A_{10} F_V), \tag{4.79}$$

where

$$A_9 = 2R\sin\theta - A_1, \tag{4.80}$$

$$A_{10} = 2R\cos\theta - A_2. \tag{4.81}$$

At P_5,

$$\begin{bmatrix} u_{U5} \\ u_{V5} \end{bmatrix} = \begin{bmatrix} C^R_{l-F_l} & 0 & 0 \\ 0 & C^R_{m-F_m} & C^R_{m-M_n} \end{bmatrix} \begin{bmatrix} \sin\theta & \cos\theta \\ \cos\theta & \sin\theta \\ A_1 & A_2 \end{bmatrix} \begin{bmatrix} F_U \\ F_V \end{bmatrix}, \tag{4.82}$$

$$\theta_{W5} = C^R_{m-M_n}(\cos\theta F_U + \sin\theta F_V) + C^R_{\theta_n - M_n}(A_1 F_U + A_2 F_V). \tag{4.83}$$

Thus, the displacements at the tip can be represented as

$$\begin{aligned}\triangle U &= -(u_{U1}+u_{U2}+u_{U3})\cos\theta+(u_{V1}+u_{V2}+u_{V3})\sin\theta \\ &+ (u_{U4}+u_{U5})\sin\theta+(u_{V4}+u_{V5})\cos\theta, \qquad (4.84)\\ \triangle V &= (u_{U1}+u_{U2}+u_{U3})\sin\theta+(u_{V1}+u_{V2}+u_{V3})\cos\theta \\ &+ (u_{U4}+u_{U5})\cos\theta-(u_{V4}+u_{V5})\sin\theta, \qquad (4.85)\end{aligned}$$

or as matrix format

$$\begin{bmatrix}\triangle U\\ \triangle V\end{bmatrix}=\begin{bmatrix}G_{11} & G_{12}\\ G_{21} & G_{22}\end{bmatrix}\begin{bmatrix}F_U\\ F_V\end{bmatrix}, \qquad (4.86)$$

where

$$\begin{aligned}G_{11} &= -D_{11}\cos\theta+D_{21}\sin\theta+E_{11}\sin\theta+E_{21}\cos\theta, \qquad (4.87)\\ G_{12} &= -D_{12}\cos\theta+D_{22}\sin\theta+E_{12}\sin\theta+E_{22}\cos\theta, \qquad (4.88)\\ G_{21} &= D_{11}\sin\theta+D_{21}\cos\theta+E_{11}\cos\theta-E_{21}\sin\theta, \qquad (4.89)\\ G_{22} &= D_{12}\sin\theta+D_{22}\cos\theta+E_{12}\cos\theta-E_{22}\sin\theta, \qquad (4.90)\end{aligned}$$

$$\begin{aligned}D_{11} &= -2C^R_{l-F_l}\cos\theta-C^L_{l-F_l}\cos\theta, \qquad (4.91)\\ D_{12} &= 2C^R_{l-F_l}\sin\theta+C^L_{l-F_l}\sin\theta, \qquad (4.92)\\ D_{21} &= 2C^R_{m-F_m}\sin\theta+C^R_{m-M_n}(A_3+A_7)+C^L_{m-F_m}\sin\theta+C^L_{m-M_n}A_5, \qquad (4.93)\\ D_{22} &= 2C^R_{m-F_m}\cos\theta+C^R_{m-M_n}(A_4+A_8)+C^L_{m-F_m}\cos\theta+C^L_{m-M_n}A_6, \qquad (4.94)\end{aligned}$$

$$\begin{aligned}E_{11} &= -C^L_{l-F_l}\cos\theta-C^R_{l-F_l}\cos\theta, \qquad (4.95)\\ E_{12} &= C^L_{l-F_l}\sin\theta+C^R_{l-F_l}\sin\theta, \qquad (4.96)\\ E_{21} &= C^L_{m-F_m}\sin\theta+C^L_{m-M_n}A_9+C^R_{m-F_m}\sin\theta+C^R_{m-M_n}A_1, \qquad (4.97)\\ E_{22} &= C^L_{m-F_m}\cos\theta+C^L_{m-M_n}A_{10}+C^R_{m-F_m}\cos\theta+C^R_{m-M_n}A_2. \qquad (4.98)\end{aligned}$$

Incorporated in the above synthesized *XYZ*-FPMs, the RRR-limb in Fig. 4.3 behaves as follows. If the force F_U along the U-axis is exerted on the tip of the RRR-limb, the tip generates a translational motion $\triangle U$,

$$\triangle U=(G_{11}-\frac{G_{12}G_{21}}{G_{22}})F_U. \qquad (4.99)$$

If the force F_V along the V-axis is exerted on the tip of the RRR-limb, the tip generates a translational motion $\triangle V$,

$$\triangle V = (G_{22} - \frac{G_{12}G_{21}}{G_{11}})F_V. \tag{4.100}$$

Therefore, it can be concluded that the translational compliances of the 3-RRR Limb i can be formulated as

$$C^i_{RRR} = \begin{bmatrix} G_{11} - \frac{G_{12}G_{21}}{G_{22}} & 0 \\ 0 & G_{22} - \frac{G_{12}G_{21}}{G_{11}} \end{bmatrix}. \tag{4.101}$$

4.3 Stiffness Modeling of *XYZ*-FPMs

Based on the exact stiffness models of the prismatic joint and the RRR-limb, the stiffness models of the *XYZ*-FPMs composed of the prismatic joint and the RRR-limb can be formulated in this section. In Fig. 3.3(b), the prismatic joint K^P_i is connected to the RRR-limb in serial. Hence, the compliance of the PRRR-limb is given as

$$C^i_{PRRR} = \left[\begin{array}{c|c} C^i_{RRR} & \mathbf{0} \\ \hline \mathbf{0} & 1/K^P_i \end{array}\right]. \tag{4.102}$$

The stiffness of the 3-PRRR *XYZ*-FPM is summation of those of the three limbs connected in parallel,

$$K_{3-PRRR} = \sum_{i=1}^{3} \frac{1}{C^i_{PRRR}}. \tag{4.103}$$

As shown in Fig. 3.3(e), the prismatic joints K^P_{i1} and K^P_{i2} are connected to the RRR-limb in serial. Hence, the compliance of the PPRRR-limb is given as

$$C^i_{PPRRR} = \left[\begin{array}{c|c} C^i_{RRR} + I \begin{bmatrix} 1/K^P_{i2} & 0 \\ 0 & 0 \end{bmatrix} & \mathbf{0} \\ \hline \mathbf{0} & 1/K^P_{i1} \end{array}\right]. \tag{4.104}$$

The stiffness of the 3-PPRRR *XYZ*-FPM is the summation of those of the three limbs connected in parallel,

$$K_{3-PPRRR} = \sum_{i=1}^{3} \frac{1}{C^i_{PPRRR}}. \tag{4.105}$$

As shown in Fig. 3.3(f), the compliance of the PRRRP-limb is given as

$$C^i_{PRRRP} = \left[\begin{array}{cc|c} C^i_{RRR} + I \begin{bmatrix} 1/K^P_{i2} & 0 \\ 0 & 0 \end{bmatrix} & & \mathbf{0} \\ \hline \mathbf{0} & & 1/K^P_{i1} \end{array}\right]. \tag{4.106}$$

The stiffness of the 3-PRRRP *XYZ*-FPM is the summation of those of the three limbs connected in parallel,

$$K_{3-PRRRP} = \sum_{i=1}^{3} \frac{1}{C^i_{PRRRP}}. \tag{4.107}$$

As shown in Fig. 3.3(a), the compliance of the PPP-limb is given as

$$K^i_{PPP} = \begin{bmatrix} K^P_{i1} & 0 & 0 \\ 0 & K^P_{i2} & 0 \\ 0 & 0 & K^P_{i3} \end{bmatrix}, \tag{4.108}$$

The stiffness of the 3-PPP *XYZ*-FPM is the summation of those of the three limbs,

$$K_{3-PPP} = \sum_{i=1}^{3} K^i_{PPP}. \tag{4.109}$$

4.4 Summary

This chapter has exactly formulated the *XYZ*-FPMs synthesized in the previous chapter. The modules to configure the *XYZ*-FPMs, i.e., the RRR-limb and the prismatic joint, have been formulated respectively. The stiffness model of the RRR-limb has been formulated based on the study on the compliances of flexure hinges by Lobontiu. The stiffness and dynamic models of the newly designed prismatic joint have been derived using an exact method proposed in this chapter.

Chapter 5

Design and Modeling of 3-PPP *XYZ*-FPM

In this thesis, a 3-PPP *XYZ*-FPM with large motion range and decoupled kinematic structure is developed. The new type of large-motion prismatic joint is used, with the advantages of no cross-axis error, no buckling, no stiffening and symmetric structure. Using these prismatic joints, the assembled 3-PPP *XYZ*-FPM possesses large motion range and small parasitic motion. This chapter focuses on structure design and dimension optimization of the 3-PPP *XYZ*-FPM. In Section 5.1, structure design of the 3-PPP *XYZ*-FPM is presented. The PRB model is formulated in Section 5.2, prepared for optimal design. In Section 5.3, a dimension optimization approach, based on the static performances, i.e., stiffness, workspace, stage size and parasitic motion, is proposed. This approach is generalized for flexure mechanisms, and three definitions, i.e., motion range (defined in Chapter 2), parasitic motion ratio and permissible maximum stiffness, are proposed and used to describe the static performances of flexure mechanisms. Using this approach, the dimensions of the 3-PPP *XYZ*-FPM are determined. In Section 5.4, the exact dynamic model of the 3-PPP *XYZ*-FPM is formulated using the proposed exact modeling method introduced in Section 4.2.

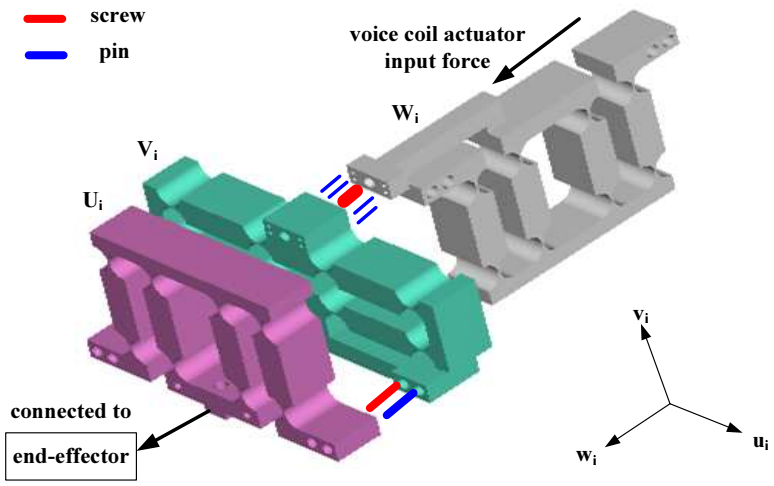

Figure 5.1: Connection of PPP-limb

5.1 Structure Design of 3-PPP *XYZ*-FPM

The 3-PPP *XYZ*-FPM is a combination of three orthogonal limbs in parallel. Each limb is a serial combination of three prismatic joints, achieving three translational DOFs, along the U_i-, V_i- and W_i-axes. The two asymmetric large-displacement prismatic joints (shown in Fig. 2.19(b)) and one new type of large-motion prismatic joint (shown in Fig. 3.2) are assembled in serial in one limb. Each prismatic joint is a monolithic workpiece fabricated using wire EDM. The three prismatic joints in one limb are connected by the pins and the screws, as shown in Fig. 5.1. The alignment of every two prismatic joints is ensured by the pins, and fastened by the screws. In each limb, W_i joint is closely connected and driven by the one-DOF voice coil actuator respectively, and U_i joint is fixed on the end-effector. Such three limbs are assembled in the orthogonal configuration to form the 3-PPP *XYZ*-FPM. The 3D schematic diagram of the 3-PPP *XYZ*-FPM is shown in Fig. 5.2.

The working principle of the 3-PPP *XYZ*-FPM can be explained based on Fig. 5.2. From the diagonal stiffness matrix (4.108), it can be concluded that the 3-PPP *XYZ*-FPM possesses a decoupled kinematic structure. Each actuator is responsible for one-axis translational motion. Here, the X-axis translational motion is explained in detail. When the force F_X along the X-axis is directly applied on W_1 joint, W_1 joint deforms to generate the X-axis motion and transfers the force to U_1 and V_1 joints. Theoretically, U_1 and V_1 joints move along the X-axis without deformation, and directly transfer the force to U_2

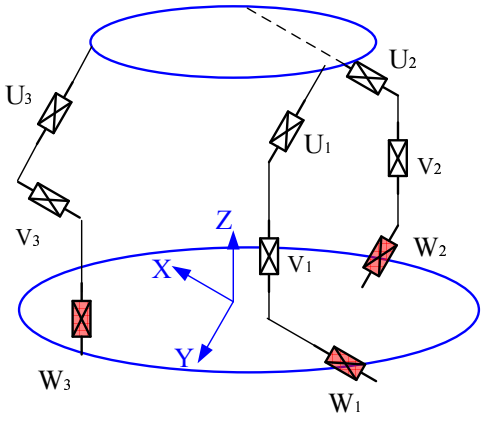

Figure 5.2: Schematic diagram of 3-PPP *XYZ*-FPM

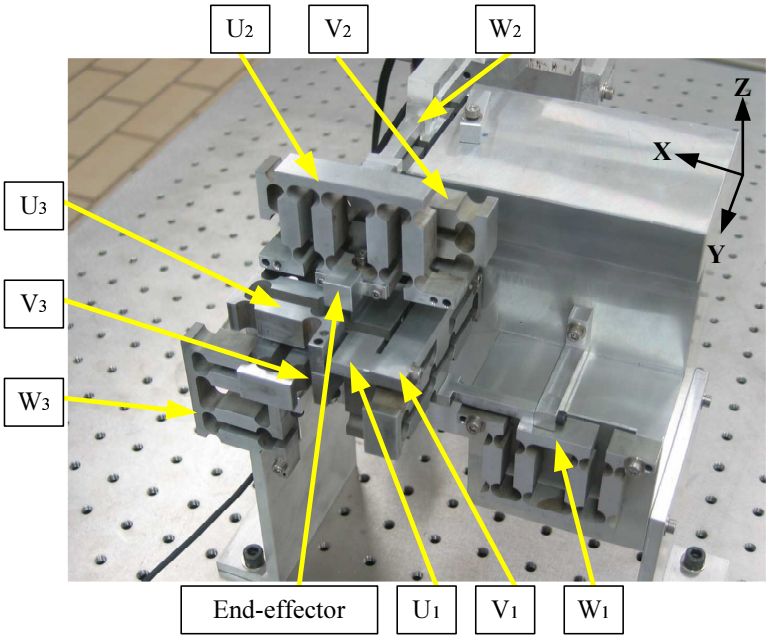

Figure 5.3: Prototype of 3-PPP *XYZ*-FPM

and V_3 joints through the end-effector. At the same time, U_2 and V_3 joints deflect to create the X-axis motion. Therefore, the translational motion along the X-axis is generated at the end-effector. Briefly, when F_X is exerted, W_1, U_2 and V_3 joints deflect to generate the X-axis motion, U_1 and V_1 joints move the same displacement as the end-effector without deformation, and other prismatic joints remain stationary. The motions along the Y- and Z-axes are similar, and are actuated by the respective voice coil actuators. The prototype of the 3-PPP *XYZ*-FPM has been fabricated, shown in Fig. 5.3.

5.2 PRB Model of 3-PPP *XYZ*-FPM

The PRB model of the 3-PPP *XYZ*-FPM is presented in this section. The PRB model will be used to the following dimension optimization, because the expressions of the specified performances are simplified and it is not complicated to find the optimal values. The optimal design using the approximate PRB models has been realized in many studies of flexure mechanisms, such as [49, 54].

5.2.1 PRB Model of Prismatic Joints

In the PRB theory, the flexure hinge can be simplified as a center-fixed revolute joint when there is no axial compressive or tensile load. In our design, the flexure hinges do not bear any axial load, and a revolute joint with the constant angular stiffness is equivalent to the flexure hinge when there is no stress concentration. According to the PRB theory, the links connecting every two notch hinges are regarded as rigid, and the length is the distance between the centers of every two flexure hinges. The equivalent rigid models of the prismatic joints are shown in Fig. 5.4. Each equivalent rigid model can be further simplified as a second-order system with a linear spring and a mass. Based on the assumption that the kinetic energy of the flexure-based prismatic joint is equal to that of the equivalent second-order system, and the kinetic energy originates from the rigid connection links. The equivalent mass of the second-order system can be derived. It is also assumed that the values of the potential energy are also identical, and the potential energy is caused by flexure revolute hinges. The equivalent stiffness can be obtained,

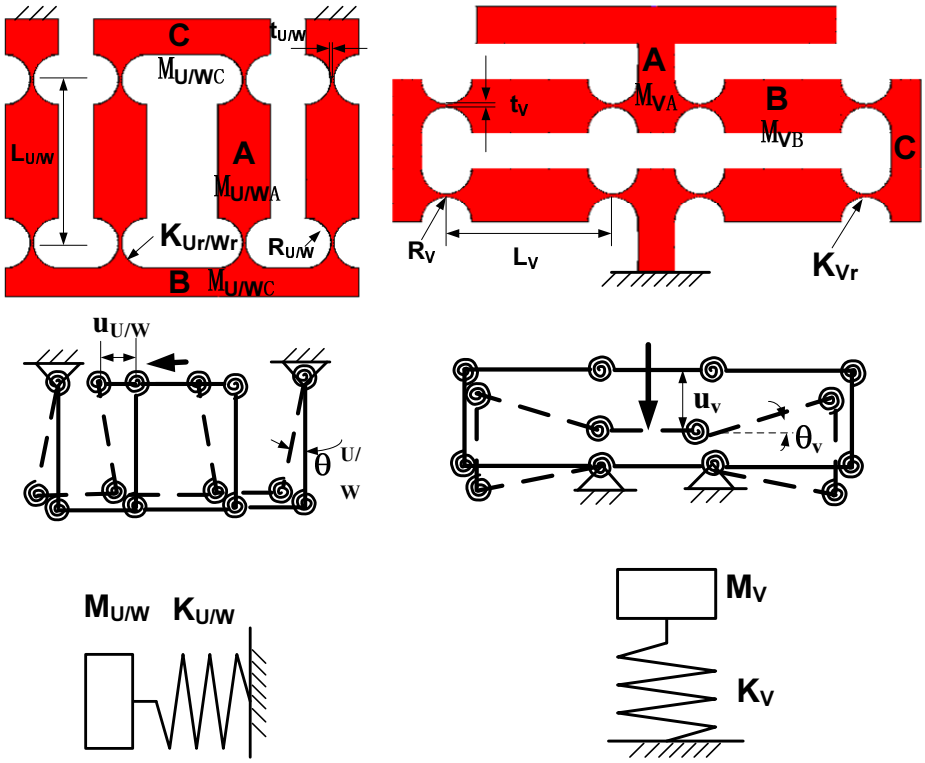

(a) W/U joints (b) V joint

Figure 5.4: PRB models of prismatic joints

$$M_{W/U} = \frac{(5M_{W/U_A} + M_{W/U_B} + 4M_{W/U_C})L_{W/U}^2 + 4J_{W/U_A}}{4L_{W/U}^2}, \tag{5.1}$$

$$K_{W/U} = \frac{2K_{W/U_r}}{L_{W/U}^2}, \tag{5.2}$$

$$M_V = \frac{(4M_{V_A} + 5M_{V_B} + 2M_{V_C})L_V^2 + 4J_{V_A}}{4L_V^2}, \tag{5.3}$$

$$K_V = \frac{2K_{V_r}}{L_V^2}. \tag{5.4}$$

In order to unify the stiffnesses of the two prismatic joints, the dimensions of the circular-flexure hinges are selected to be identical, and lengths of the connection links are also selected to be identical, thus

$$\begin{aligned} K_{U/W_r} &= K_{V_r} = K_r, \\ L_{U/W} &= L_V = L, \end{aligned}$$

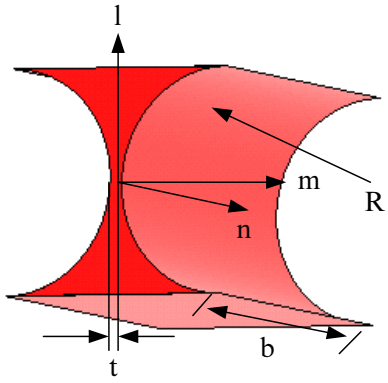

Figure 5.5: Circular-flexure hinge

where K_r is the angular stiffness of the flexure hinge.

Design of the prismatic joint is limited by that of the flexure hinge. There are two limitations. The first limitation is that the parasitic motions of flexure mechanisms originate from the nonsensitive-axis deformations of flexure hinges. Therefore, a small stiffness ratio of the sensitive-axis to the nonsensitive-axis of the flexure hinge is expected. In development of the 3-PPP *XYZ*-FPM, the problem is considered.

The circular-flexure hinge shown in Fig. 5.5 is used in the prismatic joints. The rotation about the n-axis is the sensitive motion, which is expected to generate the translational motions of the prismatic joints. The n-axis angular stiffness of the circular-flexure hinge is given as [19]

$$K_r = K_{\theta_Z - M_Z} \approx \frac{2Ebt^{\frac{5}{2}}}{9\pi R^{\frac{1}{2}}}. \tag{5.5}$$

The circular-flexure hinge also bears the nonsensitive-axis motion. As illustrated in Fig. 5.1, when the input force is applied on W_i joint along the W_i-axis, the circular-flexure hinges (in Fig. 5.5) of U_i and V_i joints will bear the moment about the m-axis in the circular-flexure hinge's local coordinates. The rotation about the m-axis of the circular-flexure hinge will introduce the parasitic rotation of the end-effector of the 3-PPP *XYZ*-FPM. Thus, circular-flexure hinges' rotation about the m-axis, termed the nonsensitive-axis motion, is not expected. The angular stiffness about the m-axis can be calculated as [19]

$$\frac{1}{K_{\theta_Y - M_Y}} = \frac{4(2R+t)\sqrt{\frac{t}{4R+t}}\arctan(\sqrt{\frac{t}{4R+t}}) - \pi t}{Eb^3 t/6}. \tag{5.6}$$

To reduce the parasitic rotations of the 3-PPP *XYZ*-FPM, the circular-flexure hinge should be sensitive to the moment about the n-axis and immune to the moment about the m-axis in the circular-flexure hinge's local coordinates, as shown in Fig. 5.5. The ratio λ should be small, and

$$\lambda = K_{\theta_Z - M_Z} / K_{\theta_Y - M_Y}. \tag{5.7}$$

The second limitation, which the flexure hinge exerts on the flexure mechanism, is that the permissible maximum stress in the flexure hinge limits the motion range of the prismatic joint. When the flexure hinge is under a bending moment about n-axis, the maximum stress occurs at each surface of the thinnest part. If the angular displacement about the n-axis of the circular-flexure hinge is θ, the estimated stress σ at the surface of the thinnest portion can be given as [18]

$$\sigma = \frac{E(1+\beta)^{\frac{9}{20}}}{\beta^2 f(\beta)}\theta, \tag{5.8}$$

where

$$f(\beta) = \frac{3+4\beta+2\beta^2}{1+\beta} + \frac{6(1+\beta)}{(2\beta+\beta^2)^{\frac{1}{2}}}\tan^{-1}\left(\sqrt{\frac{2+\beta}{\beta}}\right),$$
$$\beta = \frac{t}{2R}.$$

The yielding limit σ_b determines the maximum bending of the circular-flexure hinge, and also the maximum translational motion of the prismatic joints. When σ increases to the maximum value of σ_b, the angular deformation θ reaches the maximum value of θ_{max},

$$\theta_{max} = \frac{u_{max}}{2L}, \tag{5.9}$$

where u_{max} is the maximum linear displacement of the prismatic joint, that is, the motion range. The dimensions of the circular-flexure hinges and the rigid links of two types of large-motion prismatic joints are equal. Therefore, the maximum displacements of them are the same as

$$u_{max} = \frac{2L\sigma_b\beta^2 f(\beta)}{E(1+\beta)^{\frac{9}{20}}}. \tag{5.10}$$

In summary, these two parameters of λ and u_{max} are critical to the performances of flexure mechanisms, including the parasitic motion and the motion range. In the following dimension optimization of flexure mechanisms, λ and u_{max} will be considered to achieve high static performances of flexure mechanisms.

5.2.2 Dynamic Model of 3-PPP *XYZ*-FPM

In this section, the dynamic equation of the assembled 3-PPP *XYZ*-FPM is presented. From Fig. 5.2, it can be seen that the 3-PPP *XYZ*-FPM is a hybrid combination of the prismatic joints. Each prismatic joint can be regarded as a second-order system, and the 3-PPP *XYZ*-FPM, a hybrid combination of these second-order systems, can also be equivalent to a second-order system. The equivalent second-order systems of the prismatic joints have been formulated in Section 5.2.1. Based on these formulated prismatic joints and the working principle of the 3-PPP *XYZ*-FPM, the equivalent second-order system of the 3-PPP *XYZ*-FPM can be obtained. As shown in Fig. 5.2, when the X-axis voice coil actuator is activated, W_1, U_2 and V_3 joints deform to generate the X-axis translational motion, with U_1, V_1 and U_3 joints moving rigidly and V_2, W_2 and W_3 joints keeping stationary. Thus, for the X-axis translational motion, the equivalent second-order system of the 3-PPP *XYZ*-FPM can be illustrated as Fig. 5.6. The kinetic energy is formulated as

$$E_{K_X} = \frac{1}{2}(M_{W_1} + M_{U_2} + MV_3)\dot{X}^2 + \frac{1}{2}(m_{U_1} + m_{V_1} + m_{U_3})\dot{X}^2. \tag{5.11}$$

The potential energy is formulated as

$$E_{P_X} = \frac{1}{2}(K_{W_1} + K_{U_2} + K_{V_3})X^2. \tag{5.12}$$

Based on the Lagrange theory, the dynamic equation of the X-axis translational motion is described as

$$F_X = \frac{d}{dt}(\frac{\partial E_{K_X}}{\partial \dot{X}}) - \frac{\partial E_{K_X}}{\partial X} + \frac{\partial E_{P_X}}{\partial X}. \tag{5.13}$$

Similarly, for the Y- and Z-axes translational motions, the equivalent second-order system of the 3-PPP *XYZ*-FPM can be represented as Fig. 5.7 and Fig. 5.8 respectively. The kinetic energies are formulated as

$$E_{K_Y} = \frac{1}{2}(M_{W_2} + M_{U_1} + M_{U_3})\dot{Y}^2 + \frac{1}{2}(m_{U_2} + m_{V_2})\dot{Y}^2, \tag{5.14}$$

$$E_{K_Z} = \frac{1}{2}(M_{W_3} + M_{V_1} + M_{V_2})\dot{Z}^2 + \frac{1}{2}(m_{V_3} + m_{U_3} + m_{U_2} + m_{U_1})\dot{Z}^2. \tag{5.15}$$

The potential energies are formulated as

$$E_{P_Y} = \frac{1}{2}(K_{W_2} + K_{U_1} + K_{U_3})Y^2, \tag{5.16}$$

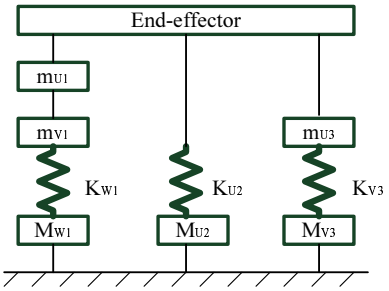

Figure 5.6: Equivalent second-order system of X-axis motion

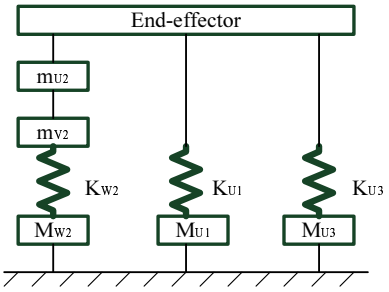

Figure 5.7: Equivalent second-order system of Y-axis motion

$$E_{P_Z} = \frac{1}{2}(K_{W_3} + K_{V_1} + K_{V_2})Z^2. \tag{5.17}$$

The dynamic equations of the Y- and Z-axes translational motions are described as

$$F_Y = \frac{d}{dt}(\frac{\partial E_{K_Y}}{\partial \dot{Y}}) - \frac{\partial E_{K_Y}}{\partial Y} + \frac{\partial E_{P_Y}}{\partial Y}, \tag{5.18}$$

$$F_Z = \frac{d}{dt}(\frac{\partial E_{K_Z}}{\partial \dot{Z}}) - \frac{\partial E_{K_Z}}{\partial Z} + \frac{\partial E_{P_Z}}{\partial Z}. \tag{5.19}$$

In the above equations, M_{U_i}, M_{V_i} and M_{W_i} are the equivalent masses of U_i, V_i and W_i joints, m_{U_i}, m_{V_i} and m_{W_i} are the actual masses of U_i, V_i and W_i joints and K_{U_i}, K_{V_i} and

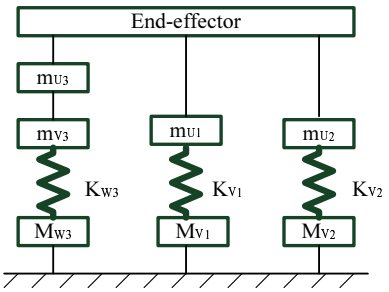

Figure 5.8: Equivalent second-order system of Z-axis motion

K_{W_i} are the equivalent stiffnesses of U_i, V_i and W_i joints.

Thus, the dynamic equation for the 3-PPP *XYZ*-FPM can be derived as,

$$\begin{bmatrix} F_X \\ F_Y \\ F_Z \end{bmatrix} = M \begin{bmatrix} \ddot{X} \\ \ddot{Y} \\ \ddot{Z} \end{bmatrix} + K \begin{bmatrix} X \\ Y \\ Z \end{bmatrix}, \tag{5.20}$$

$$M = \begin{bmatrix} M_{W_1} + M_{U_2} + M_{V_3} & 0 & 0 \\ m_{U_1} + m_{V_1} + m_{U3} & & \\ 0 & M_{W_2} + M_{U_3} + M_{U_1} & 0 \\ & m_{U_2} + m_{V_2} & \\ 0 & 0 & M_{W_3} + M_{V_1} + M_{V_2} \\ & & m_{U_3} + m_{V_3} + m_{U1} + m_{U2} \end{bmatrix},$$

$$K = \begin{bmatrix} K_{W_1} + K_{U_2} + K_{V_3} & 0 & 0 \\ 0 & K_{W_2} + K_{U_1} + K_{U_3} & 0 \\ 0 & 0 & K_{W_3} + K_{V_1} + K_{V_2} \end{bmatrix}.$$

Vector $[X, Y, Z]^T$ represents the displacements of the end-effector, which is the central point in Fig. 5.3. Vector $[F_X, F_Y, F_Z]$ represents the actuation forces exerted on the prismatic joints of W_1, W_2 and W_3 respectively.

Note that in (5.20), the damping ratio is omitted. There are two reasons to explain our omission. The first reason is that it is difficult to exactly formulate the damping. It is due to the nonreplicated nature of several parameters involved in the damping, such as material properties, manufacturing processes or the experimental environments. Moreover, the material damping is incepted at molecular level, which conflicts with the macroscale structural dynamics [86]. The second reason is that the damping of the flexure mechanism is due to energy dissipation through acoustic radiation and radiation through the supporting string, and internal dissipation [87]. These two types of dissipation are called as the passive damping. In one system, the damping is mainly from the passive damping and the active damping that accounts for energy dissipation through external devices such as actuators and assembled joints. Among these two types of dampings, the passive damping amounts to no more than 10% [88].

5.3 Dimension Optimization

5.3.1 Generalized Dimension Optimization Approach

In recent research, optimal design is conducted to obtain the expected performances of flexure mechanisms. The objective of optimal design is to obtain dimensions of flexure mechanisms to meet the performance requirements. Some studies of optimal design focus on the dynamic response, e.g., the natural frequency as the criterion, such as [49, 54]. In other studies, the resolutions of flexure mechanisms are regarded as the criterion, for example [11, 89]. However, the achievable resolutions of flexure mechanisms are difficult to be evaluated, usually limited by hardwares, i.e., actuators and sensors. Youm [90] combined the dynamic performance and the resolution as the objective function. The stiffness of the flexure mechanism is also critical, because its value is limited by the output of the actuator, and it affects positioning precision, parasitic motion and natural frequency as well. Dong [91] has studied the influence of the dimensions on the stiffness of a 6-DOF flexure platform.

The studies of optimal design mentioned above aim at achieving single performance such as natural frequency, resolution and stiffness. Here we concentrate on the optimal design with the consideration of a series of static performances. For flexure mechanisms, the main static performances include stiffness, workspace, parasitic motion and stage size. These parameters are critical for flexure mechanisms, and almost cover all static performances. In the following paragraphs, importance and relationship of these parameters are explained in detail.

Stiffness, workspace, stage size and parasitic motion almost determine whether the flexure mechanism possesses the high static performances. Parasitic motion is one important evaluation. It is not expected in flexure mechanisms, because it is difficult to be modeled and compensated. Parasitic motion is caused by nonsensitive-axis deformations of flexure hinges. The parasitic motion will be small, if the flexure mechanism simultaneously possesses the small sensitive-axis stiffness and large nonsensitive-axis stiffness. Reducing parasitic motion of flexure mechanisms can be achieved by reducing the sensitive-axis stiffness and increasing the nonsensitive-axis stiffness of flexure hinges. Thus, we

give the definition of the parasitic motion ratio λ here,

$$\lambda = \frac{senstive - axis\ stiffness}{nonsensitive - axis\ stiffness}. \tag{5.21}$$

Stiffness, workspace and stage size are not three independent evaluations. Usually, the larger the stage size, the smaller the stiffness. If the stiffness is large, the workspace will be small, because the actuation ability of PZT actuators and VCAs in flexure-based micromanipulators is limited. The output forces of the VCAs are mostly limited within several ten Newtons. Though the output forces of the PZT actuators are relatively large, the strokes are quite small. To indicate the relationship between the workspace and the stage size, the motion range β is introduced from Definition 2.1. The motion range β is defined as the ratio of the workspace to the stage size. The workspace is determined by the yielding limit of the material. The flexure mechanism with the large value of β is regarded as large-motion. The large value of β means that the flexure mechanism has a large workspace and a compacted size as well. The flexure mechanism, which has a large workspace but a large stage size, cannot be deemed as large-motion. Besides the consideration of large motion range, the stiffness of the flexure mechanism cannot exceed the actuation ability of the actuators. The permissible maximum stiffness K_max is defined as,

$$K_{max} = \frac{Maximum\ output\ force\ of\ actuator}{Workspace}. \tag{5.22}$$

Usually, the flexure mechanism with high precision, small parasitic error, large workspace and compact stage size is expected in applications such as micro/nano-scale manipulations. The three definitions we mention above give the quantitative descriptions of these requirements. Based on these quantitative formulations, dimension determination of flexure mechanisms can be generalized as the optimal problem.

- Objective function: Minimize λ or $\frac{1}{\beta}$,
- Design variables: Dimensions of the flexure hinge including the radius of R, thickness of t and width of b,

  Lengths of the links connecting every two flexure hinges,
- Constraints: Stiffness $\leq K_{max}$,

Stage size $\leq$ permissible maximum size,

Desired workspace $\leq$ range constrained by material elasticity,

$\beta \geq$ desired value or $\lambda \leq$ desired value.

The task of optimal design is to determine the dimensions of the flexure mechanism. Hence, the dimensions are represented as the design variables. The flexure mechanism is expected to possess high precision with small parasitic errors or large workspace with compact stage size. Hence, the objective function is represented as minimization of λ or $\frac{1}{\beta}$ or the weight function of both. Simultaneously, the flexure mechanism is limited by the hardware such as the actuation, the mounting space and the material elasticity. Hence, these limitations are represented as the constraints.

Optimal design of flexure mechanisms based on the static performances has been generalized the single-objective optimal problem. Most of the standard single-objective optimization algorithms can be easily used in our generalized optimal design.

5.3.2 Dimension Optimization of 3-PPP *XYZ*-FPM

Using the above generalized dimension optimization approach and the above PRB model of the 3-PPP *XYZ*-FPM, dimension optimization of the 3-PPP *XYZ*-FPM can be formulated as follows,

- Objective: Minimize λ,
- Design variables: R, t, b, L,
- Constraints: $\beta \geq \frac{1}{20}$

  $0.3mm \leq t \leq 1mm$,

  $10mm \leq b \leq 20mm$,

  $20mm \leq L \leq 30mm$,

  $1mm \leq u_{max}$,

  $K \leq 50N/mm$.

The objective of optimal design is to develop a 3-PPP *XYZ*-FPM with minimum parasitic motion. λ is defined in (5.7). The design variables are the dimensions of the circular-flexure hinges and the distance between every two circular-flexure hinges. The constraints consider the factors as follows. Since the 3-PPP *XYZ*-FPM is assembled using nine pieces of prismatic joints, the 3-PPP *XYZ*-FPM will possess large motion range if β of the prismatic joint is large. β is defined as $u_{max}/(2R + L)$. The flexure mechanism is cut by wire EDM. The thinnest portion of the circular-flexure hinge is not less than $0.3mm$, because the tolerance of $\pm 0.01mm$ cannot be ensured when the thickness is smaller than $0.3mm$. For compactness, the size of the 3-PPP *XYZ*-FPM should not be large, and thus the distance between every two circular-flexure hinges is limited. In order to achieve the desired motion range without plastic deformation, the maximum displacement should be larger than the required absolute motion range of $1mm$. With limitation of the output of the VCA, the linear stiffness of the 3-PPP *XYZ*-FPM cannot exceed $50N/mm$.

The Gradient Projection Method (GPM) is used to search the optimal points in the workspace. The final values of the design variables are listed in Table 5.1. The 3-PPP *XYZ*-FPM possesses the advantage of large motion range, as proved by the following calculations. Substituting these parameters into the PRB model formulated in Section 5.2, the linear stiffness and the workspace of the prismatic joint can be calculated as

$$\begin{aligned} K_{W/U} &= K_V = 10.4N/mm, \\ u_{max} &= 2.3mm. \end{aligned}$$

The motion range of the designed large-motion prismatic joint is

$$\beta_P = \frac{u_{max}}{2R + L} = \frac{2.3}{32} \approx 7\%.$$

The dimensions of the assembled 3-PPP *XYZ*-FPM are $185mm \times 141mm \times 148mm$, and the motion range of the 3-PPP *XYZ*-FPM is

$$\beta = \frac{2.3mm}{185mm} \approx \frac{1}{80}. \tag{5.23}$$

The value is large compared to the current flexure mechanisms illustrated in Table 2.2.

Table 5.1: Results of dimension optimization

R	t	b	L
3.5mm	0.4mm	10mm	25mm

The matrices of the equivalent mass and the equivalent stiffness of the 3-PPP *XYZ*-FPM can be given as

$$M = \begin{bmatrix} 0.1304 & 0 & 0 \\ 0 & 0.1104 & 0 \\ 0 & 0 & 0.1504 \end{bmatrix} Kg,$$

$$K = \begin{bmatrix} 31.3 & 0 & 0 \\ 0 & 31.3 & 0 \\ 0 & 0 & 31.3 \end{bmatrix} N/mm.$$

Based on the above matrices, the natural frequencies for the translational mode shape of the 3-PPP *XYZ*-FPM can be calculated as

$$f_X = \frac{1}{2\pi}\sqrt{\frac{31300}{0.1304}} \approx 78Hz,$$
$$f_Y = \frac{1}{2\pi}\sqrt{\frac{31300}{0.1104}} \approx 85Hz,$$
$$f_Z = \frac{1}{2\pi}\sqrt{\frac{31300}{0.1504}} \approx 73Hz.$$

5.4 Exact Modeling of 3-PPP *XYZ*-FPM

5.4.1 Static Analysis of Prismatic Joints

It has been mentioned in Section 5.2, the two types of prismatic joints used in the proposed *XYZ*-FPM have the same working principle and stiffness, and the same analytical method can be used. Only analysis of the prismatic joint in Fig. 4.2(a) is presented here.

Substituting the dimensions in Table 5.1 into equations (4.24) to (4.13), the internal moment M_3 can be calculated as

$$M_3 = \frac{-3.5F}{4}. \tag{5.24}$$

Substituting (5.24) into equations (4.7) to (4.9), the angular deformations can be rewritten as

$$\begin{aligned}\theta_1(\alpha) &= \int_{-\frac{\pi}{2}}^{\alpha} \frac{10.5F(18-3.5\sin\gamma)\cos\gamma}{96E(3.7-3.5\cos\gamma)^3}d\gamma \\ &= \frac{F}{E}[188.6971\arctan(6\tan\frac{\alpha}{2}) + \frac{1134.5138\tan\frac{\alpha}{2}-0.2954}{36\tan^2\frac{\alpha}{2}+1} \\ &+ \frac{754.7882\tan\frac{\alpha}{2}+5.4645}{(36\tan^2\frac{\alpha}{2}+1)^2}], \end{aligned} \tag{5.25}$$

$$\begin{aligned}\theta_2(x) &= \int_{2R}^{x} \frac{F(11.5-x)}{202.612E}dx + \frac{592.9109F}{E} \\ &= \frac{F}{E}(-0.0012x^2+0.0768x+592.9109), \end{aligned} \tag{5.26}$$

$$\begin{aligned}\theta_3(\beta) &= \int_{-\frac{\pi}{2}}^{\beta} \frac{-12.25F\sin\gamma\cos\gamma}{32(3.7-3.5\cos\gamma)^3}d\gamma - \frac{0.6719F}{E} \\ &= \frac{F}{E}[17.9305\arctan(6\tan\frac{\beta}{2}) + \frac{107.8045\tan\frac{\beta}{2}-0.2954}{36\tan^2\frac{\beta}{2}+1} \\ &+ \frac{71.7220\tan\frac{\beta}{2}+5.4645}{(36\tan^2\frac{\beta}{2}+1)^2} - 0.6719]. \end{aligned} \tag{5.27}$$

The linear deformations and the constraints can be represented as

$$\begin{aligned}Y_1(\alpha) &= \int \theta_1(\alpha)R\cos\alpha d\alpha \\ &= \int \frac{3.5F}{E}[188.6971\arctan(6\tan\frac{\alpha}{2}) + \frac{1134.5138\tan\frac{\alpha}{2}-0.2954}{36\tan^2\frac{\alpha}{2}+1} \\ &+ \frac{754.7882\tan\frac{\alpha}{2}+5.4645}{(36\tan^2\frac{\alpha}{2}+1)^2}]\cos\alpha d\alpha, \end{aligned} \tag{5.28}$$

$$Y_1(-\frac{\pi}{2}) = 0, \tag{5.29}$$

$$\begin{aligned}Y_2(x) &= \int \theta_2(x)dx \\ &= \int \frac{F}{E}(-0.0012x^2+0.0768x+592.9109)dx, \end{aligned} \tag{5.30}$$

$$Y_2(2R) = Y_1(\frac{\pi}{2}), \tag{5.31}$$

$$\tag{5.32}$$

$$
\begin{aligned}
Y_3(\beta) &= \int \theta_3(\beta) R\cos\beta d\beta \\
&= \int \frac{3.5F}{E}[17.9305\arctan(6\tan\frac{\beta}{2}) + \frac{107.8045\tan\frac{\beta}{2} - 0.2954}{36\tan^2\frac{\beta}{2}+1} \\
&+ \frac{71.7220\tan\frac{\beta}{2} + 5.4645}{(36\tan^2\frac{\beta}{2}+1)^2} - 0.6719]\cos\beta d\beta, \qquad (5.33)\\
Y_3(-\frac{\pi}{2}) &= Y_2(L). \qquad (5.34)
\end{aligned}
$$

By solving equations (5.28) to (5.34), the linear deformation $Y_3(\frac{\pi}{2})$ at P_3 can be obtained, and the linear stiffness of the single limb can be calculated using (4.21) as

$$K_{Y-F_Y} = \frac{F/4}{Y_3(\frac{\pi}{2})} \approx 7.31N/mm. \qquad (5.35)$$

The equivalent linear stiffness of the prismatic is identical to that of the single limb, and (4.22) can be calculated as

$$K_V^* = K_{Y-F_Y} \approx 7.31N \cdot mm. \qquad (5.36)$$

The equivalent mass of the prismatic joint can be calculated using (4.27) as

$$M_V^* = 0.0211Kg. \qquad (5.37)$$

5.4.2 Dynamic Model of 3-PPP *XYZ*-FPM

The dynamic equation derived using the proposed exact modeling method has the same format as that from the PRB model. The equivalent mass and the equivalent stiffness matrices of the 3-PPP *XYZ*-FPM are obtained as

$$
M^* = \begin{bmatrix}
M_{W_1}^* + M_{U_2}^* + M_{V_3}^* & 0 & 0 \\
m_{U_1} + m_{V_1} + m_{U3} & & \\
0 & M_{W_2}^* + M_{U_1}^* + M_{U_3}^* & 0 \\
 & m_{U_1} + m_{V_2} & \\
0 & 0 & M_{W_3}^* + M_{V_1}^* + M_{V_2}^* \\
 & & m_{U_3} + m_{V_3} + m_{U1} + m_{U2}
\end{bmatrix},
$$

$$
K^* = \begin{bmatrix}
K_{W_1}^* + K_{U_2}^* + K_{V_3}^* & 0 & 0 \\
0 & K_{W_2}^* + K_{U_1}^* + K_{U_3}^* & 0 \\
0 & 0 & K_{W_3}^* + K_{V_1}^* + K_{V_2}^*
\end{bmatrix}.
$$

Substituting the dimensions in Table 5.1, the matrices of the equivalent mass and the equivalent stiffness can be calculated as

$$
\begin{aligned}
M^* &= \begin{bmatrix} 0.1265 & 0 & 0 \\ 0 & 0.1065 & 0 \\ 0 & 0 & 0.1465 \end{bmatrix} Kg, \\
K^* &= \begin{bmatrix} 21.93 & 0 & 0 \\ 0 & 21.93 & 0 \\ 0 & 0 & 21.93 \end{bmatrix} N/mm.
\end{aligned}
$$

Based on the above matrices of mass and stiffness, the natural frequencies for the translational mode shape of the 3-PPP *XYZ*-FPM are obtained as

$$
\begin{aligned}
f_X^* &= \frac{1}{2\pi}\sqrt{\frac{21930}{0.1265}} \approx 66.3Hz, \\
f_Y^* &= \frac{1}{2\pi}\sqrt{\frac{21930}{0.1065}} \approx 72.3Hz, \\
f_Z^* &= \frac{1}{2\pi}\sqrt{\frac{21930}{0.1465}} \approx 61.6Hz.
\end{aligned}
\tag{5.38}
$$

5.5 Summary

In this chapter, the generalized dimension optimization approach has been proposed, based on the static performances of flexure mechanisms, i.e., stiffness, workspace, stage size and parasitic motion. The structure of a 3-PPP *XYZ*-FPM has been designed. Using the generalized dimension optimization approach, the dimensions of the 3-PPP *XYZ*-FPM have been determined. The designed large-motion prismatic joint has the large workspace of $2.3mm$ and large relative motion range of 7%. The assembled 3-PPP *XYZ*-FPM also has the large workspace of $2.3mm$ and the large motion range of $1/80$. The exact stiffness and dynamic models of the 3-PPP *XYZ*-FPM have been formulated using the exact modeling method proposed in the previous chapter.

Chapter 6

Prototype, Simulation and Experiment

In this chapter, the prototype of the 3-PPP *XYZ*-FPM is presented. The static performances of the 3-PPP *XYZ*-FPM and the new prismatic joint designed in Chapter 3, including stiffness and parasitic motion, are tested. The modal simulation is conducted to study the mode shapes which occur in the actual operation. The hammer test is conducted to measure the corresponding natural frequencies of the simulated mode shapes. These experiments aim at validation of the structure design, the dimension optimization and the exact modeling method.

6.1 Prototype Development

In development of flexure mechanisms, selected material, manufacturing error, actuation and sensing can influence the positioning precision of flexure mechanisms. Determination of these aspects become important for flexure mechanisms.

6.1.1 Material Selection

The property of the selected material is important to the performances of flexure mechanisms. The material selection should meet the requirements of large deflection strength S_y/E, high strength S_y, low internal stress $k/\Omega E$ and low thermal expansion $1/\Omega$. E, S_y, k and Ω are Young's modulus, yield stress, thermal conductivity and thermal expansion coefficient respectively. The materials that can be used in flexure mechanisms

Table 6.1: Properties of AL 7075

Material	E	S_y	ρ	$1/\Omega$
AL 7075	$72N/mm^2$	$510N/mm^2$	$2.8kg/dm^3$	$23 \times 10^{-6}/°C$

include aluminium, titanium, steel and beryllium copper [92].

Several aluminium alloys are available and commonly used in flexure mechanisms. Aluminium is not stiff and its density is the lowest in these available materials. Among aluminium alloy, 2000, 6000 and 7000 are the only heat treatable series, where strength improvement can be achieved by precipitation hardening without any cold working , which adds significant amounts of internal stresses. AL 2024 and AL 7075 are aircraft alloys that offer very high strengths, whereas AL 6061 is common for regular use and has a moderate strength. Judged by the phase stability of a long period of time, AL 6061 and AL 7075 are recommended for precision instruments [93].

Beryllium copper and titanium are stiffer than aluminium, and have larger density than that of aluminium. Beryllium has good thermal performances, such as low thermal expansion. Its drawback is that it cannot be used in flexure mechanisms under vibration, because its deflection is very small in case of vibration. Titanium has poor thermal conductivity and moderate thermal expansion, more like that of ceramic. Steel is the stiffest material, and has large density offering high damping [93].

With the consideration of materials properties, fabrication and cost, AL 7075 is selected as the material of the 3-PPP *XYZ*-FPM. The properties of AL 7075 is listed in Table. 6.1.

6.1.2 Manufacturing and Assembling

Because of the requirements of small size and high tolerance of flexure mechanisms, the conventional machining is not suitable to fabrication of flexure mechanisms. EDM is a common machining method for fabrication of flexure mechanisms. There are two types of EDMs, i.e., plunge EDM and wire EDM [92].

Plunge EDM

Plunge EDM utilizes electric discharges to erode local areas of a surface as a shaped electrode is brought into close proximity to a grounded workpiece surface. A shaped electrode is produced using conventional machining. The workpiece is immersed in a dielectric fluid. A potential is then applied to the electrode and it is lowered towards the workpiece surface until electric discharges are produced. Electrodes are usually made from materials with a high melting temperature and high latent heat of melting. Graphite is often used for shaped electrodes, while tungsten wires are commonly used to produce small holes of high aspect ratios.

Wire EDM

In wire EDM, the electrode is a thin wire that is continuously fed through the workpiece. This is then electrically energized and used to erode a thin line through the workpiece material. Moving the wire in a controlled path through the specimen results in the desired geometry. In practice, wires ranging in size from $0.025mm$ and $1mm$ are common. Presently, capital cost of these machines is high, and the continued costs of wire and filtering of the flushing fluid limit this process to the production of precise flexures. Some of the advantages of wire EDM for flexures are listed as follows.

- Components of almost arbitrary complexity can be produced.
- Any reasonable conductor can be machined enabling choice from the hardest materials.
- For thin wires, the gaps between surfaces can be correspondingly small, enabling the design of compact mechanisms.
- Being capable of machining to depths of $100 - 200mm$, geometry of high aspect ratio can be produced making possible designs with high ratios of stiffness between the free and constrained directions.
- Highly automated machines capable of re-threading accidentally broken wires can be left unattended, therefore reducing labor costs.

- Workpiece can be stacked to produce multiple components with a single machining cycle.

Under controlled conditions, it is not unreasonable to produce components holding tolerances within a few micrometers and with sub-micrometer surface finish. Flexures measuring $0.1mm$ in the thinnest portion are routinely manufactured. Although some surface alteration must occur, no significant problems caused by this have been observed in flexures of these dimensions. Current machines can produce components to accuracies of better than a few micrometers.

The 3-PPP *XYZ*-FPM designed in this project is fabricated using wire EDM. The width of the thinnest portion of the notch hinges is $0.4mm$, and the tolerance of $\pm 0.01\mu m$ is assigned.

6.1.3 Actuation

Performance of the actuators for flexure mechanisms are critical to the precision of the flexure-based mechatronic system. Main types of commercial actuators driving flexure mechanisms include PZT actuator, mechanical micrometer and VCA based on the electromagnetic theory [92].

PZT material experiences a dimensional change upon application of an electrical potential gradient. Based on this property of the PZT material, some PZT actuators have been produced and applied, such as the piezoelectric stack actuators by US EuroTek, Inc. [94] and the ultra-reliable piezo actuators by PI (Physik Instrumente) L.P. [95]. These PZT actuators have the advantages of large output force and high response speed. Whereas, their drawbacks are small stroke, usually below $100\mu m$, hysteresis and creep. Hysteresis and creep introduce nonlinear errors into the flexure-based system,which cannot be easily compensated.

Standard micrometer screws provide a low cost solution to many short to medium range drive applications. The open-loop micrometer can achieve the positioning precision of $1 - 2\mu m$. The closed-loop micrometer has the positioning precision of $0.1\mu m$. Its disadvantages include backlash caused by screw, temperature sensitivity and nonlinearities.

Table 6.2: Characteristics of actuators

Actuator	PZT	Micrometer	VCA
Force	Large	Large	Small (within 100N)
Stroke	micrometer	millimeter	millimeter
Stiffness	High	Medium	≈ 0
Linearity	Poor	Moderate	Good
Continuity	Yes	No	Yes
Accuracy	Medium	Low	High (nanometer)
Cost	Medium	Low	Medium

Picomotor 8301-8341 by New Focus [96] is a combined product of PZT and micrometer with the resolution of $30nm$. This type of actuators have the advantages of large output force and large stroke, but their resolution and repeatability are poor because of backlash of screws.

In precision electromagnetic devices, a saturated permanent magnet is surrounded by a coil. A force is generated between the magnet and the coil, which is proportional to both the strength of the magnet and the gradient of the field from the coil perpendicular to the axis of the magnet. The force can be transferred to the flexure mechanism to generate a desired displacement. Above is the working principle of VCAs. The advantages are large stroke, high linearity and high accuracy. However, the output forces are small, usually within $100N$.

Evaluating the three types of actuators in aspects of output force, stroke, linearity, accuracy and cost (listed in Table 6.2), in this project, the voice coil actuator AVM 60 by Akribis [1] is selected, of which specifications are listed in Table 6.3. The VCA is driven by a linear amplifier TA115 by Trust [97].

Table 6.3: Specifications of AVM 60 [1]

	Unit	AVM 60
Stroke	mm	25
Force costant	N/A	15.7
Continuous force	N	31.4
Peak force	N	94.2
Continuous current	A	2
Peak current	A	4.7
Resistance	Ω	5.2
Max coil temperature	$^{\circ}C$	155
Coil assembly mass	g	316

6.1.4 Sensing

In order to obtain the stiffness, the displacements of the prismatic joint and the 3-PPP *XYZ*-FPM are needed to be measured. The ultra high accuracy laser displacement meter LC2400 series by KEYENCE [2] is used to measure the displacements. LC2430 and LC2440 are used in this project. The specifications are listed in Table 6.4.

The force sensor is also used to measure the output force of the actuator to the single prismatic joint and the 3-PPP *XYZ*-FPM. The specifications of the six-dimensional Nano 43 F/T Transducer by ATI [3] are listed in Table 6.5. Only the Z-axis sensory cell is used to measure the one-dimensional force applied to the single prismatic joint and the 3-PPP *XYZ*-FPM.

6.2 Static Test of Prismatic Joint

To verify the proposed exact modeling method in Chapter 4, the static test is conducted to measure the linear stiffness of the single prismatic joint. The force exerted on the

Table 6.4: Specifications of laser displacement sensor [2]

	LC 2430	LC 2440
Measuring Range	± 0.5 mm	± 3 mm
Operating Distance	30 mm	30 mm
Resolution	0.02 μm	0.2 μm
Linearity	$\pm 0.5\%$ of F.S.	$\pm 0.5\%$ of F.S.
Sampling Frequency	50 kHz	50 kHz
Response Frequency	20 kHz	20 kHz
Response Time	100 μm	100 μm
Measuring Stability	$\pm 0.2\%$ of F.S.	$\pm 0.03\%$ of F.S.

Table 6.5: Specifications of Nano 43 F/T Transducer [3]

Sensing Range	F_X, F_Y, F_Z ($\pm$ N)	36
	T_X, T_Y, T_Z ($\pm$ N)	0.5
Resolution	F_X, F_Y, F_Z ($\pm$ N)	(1/512) $\times$ 36
	T_X, T_Y, T_Z ($\pm$ N)	(1/40000) $\times$ 0.5

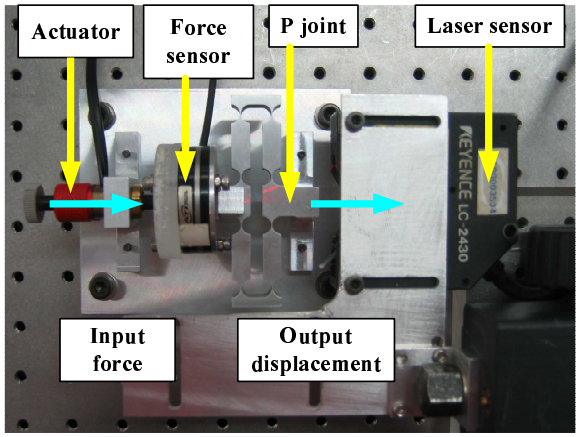

Figure 6.1: Experimental setup of prismatic joint

Table 6.6: Results of linear stiffness of prismatic joint

	Experiment	PRB	Nonlinear method
Value	7.79N/mm	10.4N/mm	7.31N/mm
Percentage Error		33.5%	6.2%

prismatic joint and the output displacement are needed for calculating the stiffness. The actuation force is measured by the six-dimensional force sensor FT05270 (ATI), and the displacement is detected by the laser sensor LC2430 (KEYENCE). The experimental setup is shown in Fig. 6.1.

The experimental data, the forces and the displacements, are plotted in Fig. 6.2. Based on these data, a straight line is fitted with the slope of $128.3\mu m/N$. The reciprocal of the slope is the linear stiffness of the prismatic joint, of which value is $7.79N/mm$.

Table 6.6 lists the results of the stiffness of the prismatic joint. The stiffness from the PRB method is calculated from(5.5). It shows that the exact modeling method is more accurate than the PRB method. The modeling accuracy is increased significantly. The percentage error between the values from the exact modeling method and the experiment may be due to manufacturing error and sensing error.

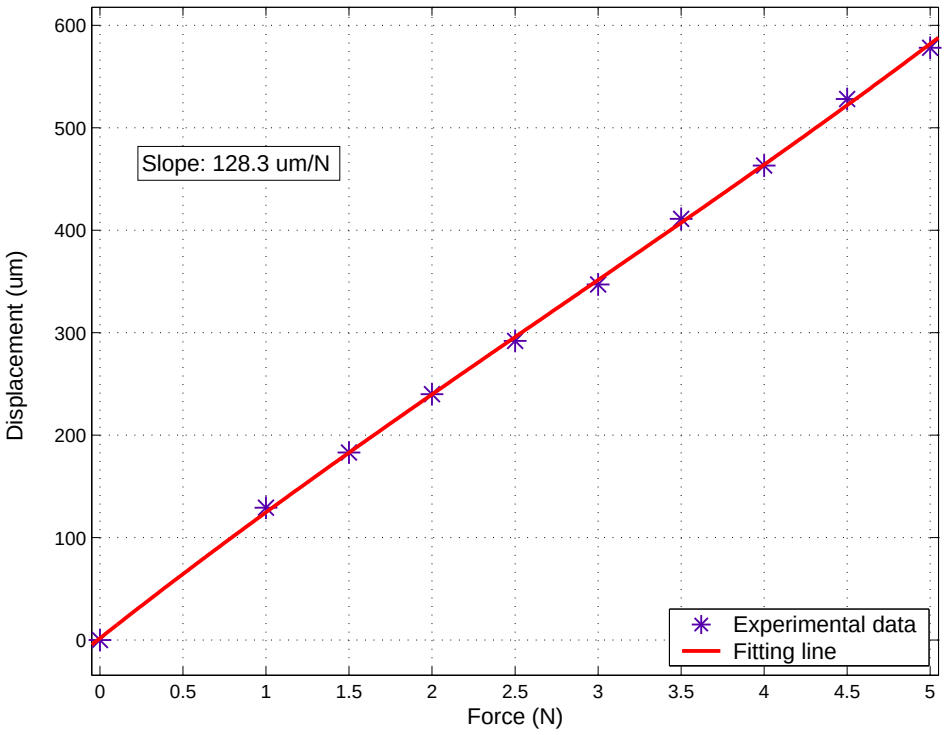

Figure 6.2: Experimental result of linear stiffness of prismatic joint

6.3 Static Tests of 3-PPP *XYZ*-FPM

In this section, the static performances of the 3-PPP *XYZ*-FPM are tested, including the linear stiffness and the parasitic motions, to verify the proposed exact modeling method and the decoupled kinematic structure.

6.3.1 Stiffness Measurement of 3-PPP *XYZ*-FPM

The linear stiffnesses of the 3-PPP *XYZ*-FPM along the X-, Y- and Z-axes are determined respectively. The linear stiffness is the ratio of the measured actuation force to the displacement. The six-axis force sensor FT05270 is mounted on W_1, W_2 and W_3 joints respectively, to measure the actuation forces. The laser sensor LC2430 is used to measure the displacements of the end-effector along the X- and Y-axes respectively. The end-effetor is located at the center of the 3-PPP *XYZ*-FPM. Fig. 6.3 shows the experimental setup for measuring the linear stiffness along the Y-axis.

The input forces and the output displacements are measured and plotted, and these sampled points are fitted with the straight lines. The slopes of the fitted straight lines describe

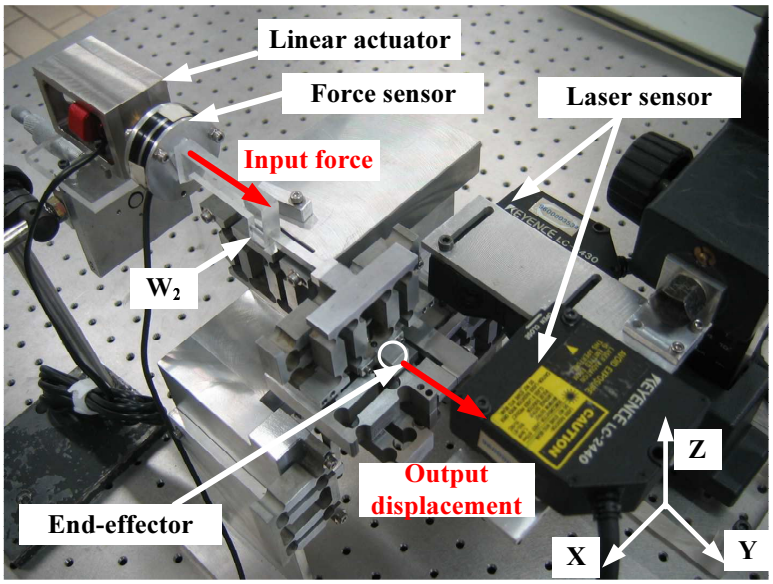

Figure 6.3: Experimental setup of 3-PPP *XYZ*-FPM

the linear stiffnesses of the 3-PPP *XYZ*-FPM. In Fig. 6.4, the first fitted straight line describes the stiffness along the X-axis of the 3-PPP *XYZ*-FPM. The slope of the straight line is $39.1\mu m/N$, and its reciprocal is the linear stiffness of $25.6N/mm$. In Fig. 6.5, the second straight line describes the stiffness along the Y-axis of the 3-PPP *XYZ*-FPM. The slope of the straight line is $39.4\mu m/N$, and its reciprocal is the linear stiffness of $25.4N/mm$. In Fig. 6.6, the third straight line describes the stiffness along the Z-axis of the 3-PPP *XYZ*-FPM. The slope of the straight line is $39.6\mu m/N$, and its reciprocal is the linear stiffness of $25.3N/mm$.

Comparison of the linear stiffness values from the PRB method, the exact modeling method and the experiment, is shown in Table 6.7. The stiffness from the PRB method is calculated from (5.20). The result from the exact modeling method is closer to the actual value than that from the PRB method. The difference between the analytical value and the experimental result may be caused by manufacturing and assembly errors.

6.3.2 Parasitic Error Measurement of 3-PPP *XYZ*-FPM

Measurement of the parasitic motions of the 3-PPP *XYZ*-FPM aims at verifying design of the decoupled kinematic structure. The parasitic motions of the 3-PPP *XYZ*-FPM presented here, include the cross-axis error and the parasitic rotation. The cross-axis

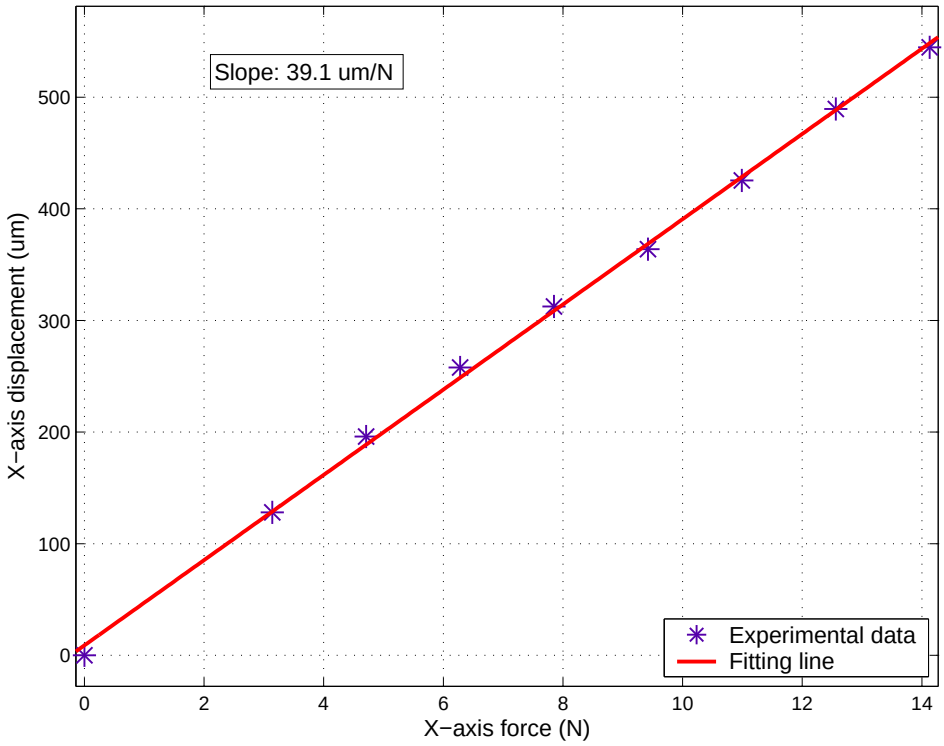

Figure 6.4: X-axis linear stiffness

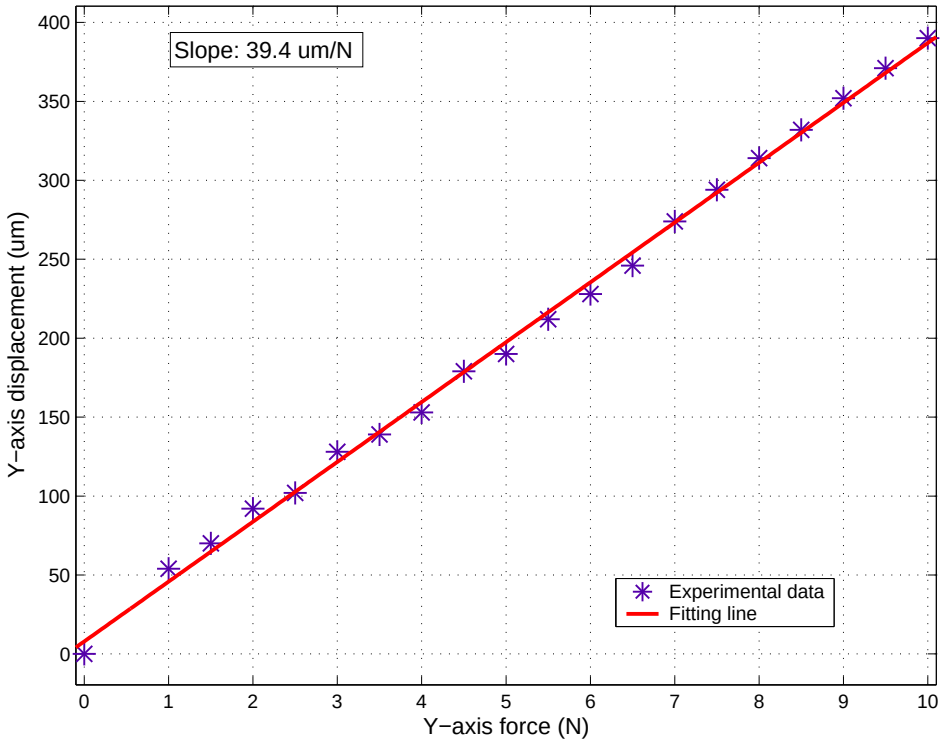

Figure 6.5: Y-axis linear stiffness

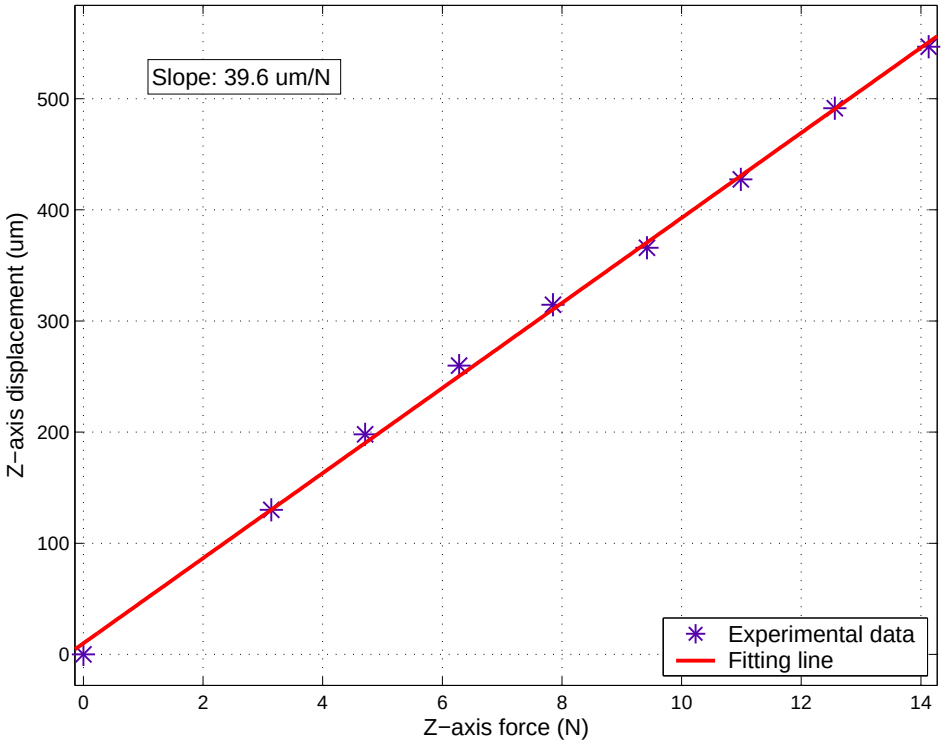

Figure 6.6: Z-axis linear stiffness

Table 6.7: Results of linear stiffness of 3-PPP *XYZ*-FPM

		Experiment	PRB	Nonlinear method
Stiffness	X	25.6N/mm	31.3N/mm	21.93N/mm
	Y	25.4N/mm	31.3N/mm	21.93N/mm
	Z	25.3 N/mm	31.3N/mm	21.93N/mm
Percentage error	X		22.3%	14.3%
	Y		23.2%	13.7%
	Z		23.7%	13.3%

error is defined as the displacement ratio of the unactuated-axis to the actuated-axis. The parasitic rotation is defined as the rotary angles of the end-effector when the translational motions are actuated. There are two sets of experiments are conducted to evaluate the parasitic errors of the 3-PPP *XYZ*-FPM.

The first set of experiments are conducted to evaluate the cross-axis errors of the 3-PPP *XYZ*-FPM. The experimental setup for measuring the cross-axis errors is shown in Fig. 6.3. When the force, e.g., along the Y-axis, is generated to push the mechanism, the force sensor measures the linear input force, the laser sensor LC2440 measures the Y-axis displacement at the end-effector, and LC2430 measures the X-axis displacement simultaneously. The displacement ratio of the unactuated-axis to the actuated-axis, e.g., the motion ratio of the X-axis to the Y-axis, can be calculated, shown in Fig. 6.7(a). The same input forces are fed along the Y-axis, the laser sensor LC2440 measures the Y-axis motion, and LC2430 measures the Z-axis value. The motion ratio of the Z-axis to the Y-axis can be calculated, shown in Fig. 6.7(b). Thus, the cross-axis errors along the X- and Z-axes can be obtained, when the Y-axis motion is actuated. The same procedures are applied to measure the cross-axis errors when the X- and Z-axes motions are actuated, shown in Fig. 6.8(a), Fig. 6.8(b), Fig. 6.9(a) and Fig. 6.9(b). The Table 6.8 lists the maximum cross-axis errors of the X-, Y- and Z-axes. It can be concluded that the cross-axis errors of the 3-PPP *XYZ*-FPM are smaller than 2%. Note that LC2430 with the resolution of $0.02\mu m$ and LC2440 of $0.2\mu m$ are used to simultaneously measure the two-axes motions. In the ideal situation, the displacement sensors with the same resolutions should be utilized to measure the two-axes motions simultaneously. Due to the hardware limitation, LC2430 and LC2440 are used, but they do not affect the measured results. The high-resolution LC2430 is used to measure the unactuated-axis motion, and the low-resolution LC2440 is applied to measure the actuated-axis motion. The resolution ratio of LC2430 ro LC2440 is $1/10$, which means that the limit of the measured cross-axis error is 10%. The cross-axis error below 10% can be measured accurately, and the measured values are all equal to 10% if the real values are larger than 10%. Since the measured values in our experiments are 2%, below 10%, the results are still credible.

The second set of experiments are conducted to obtain the parasitic rotations at the end-effector. In dimension optimization in Chapter 5, the parasitic rotations are considered

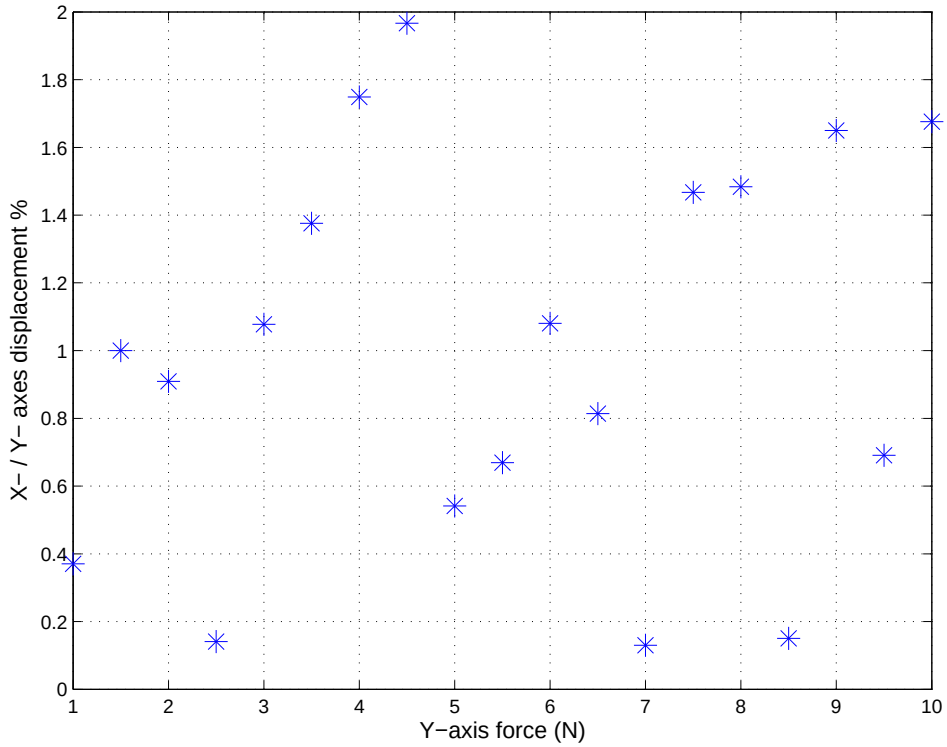

(a) X/Y error

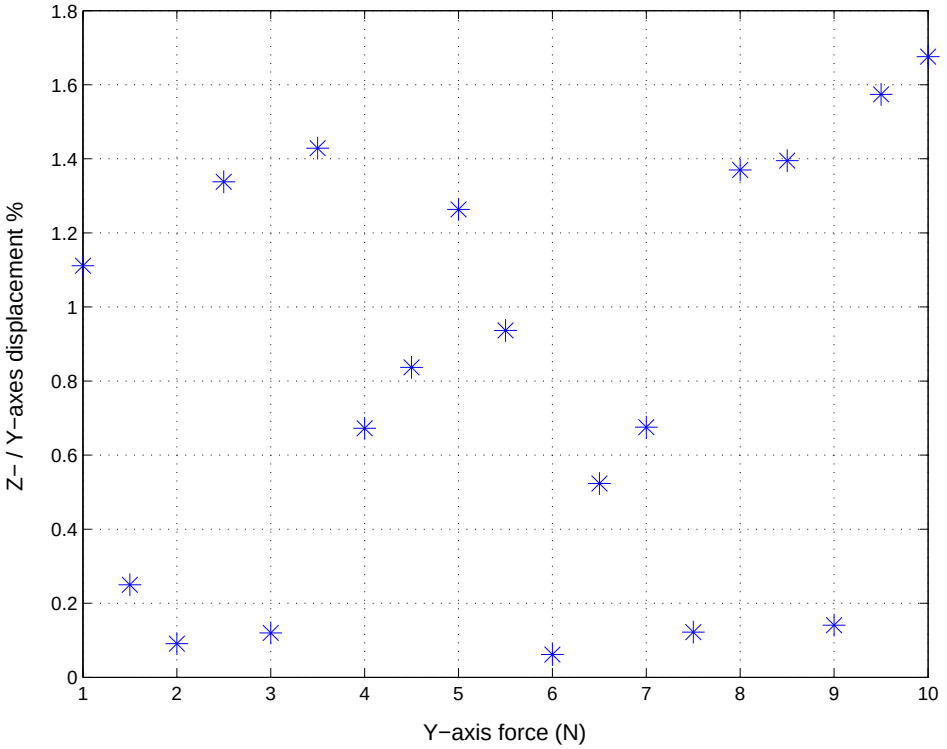

(b) Z/Y error

Figure 6.7: Y-axis cross-axis errors

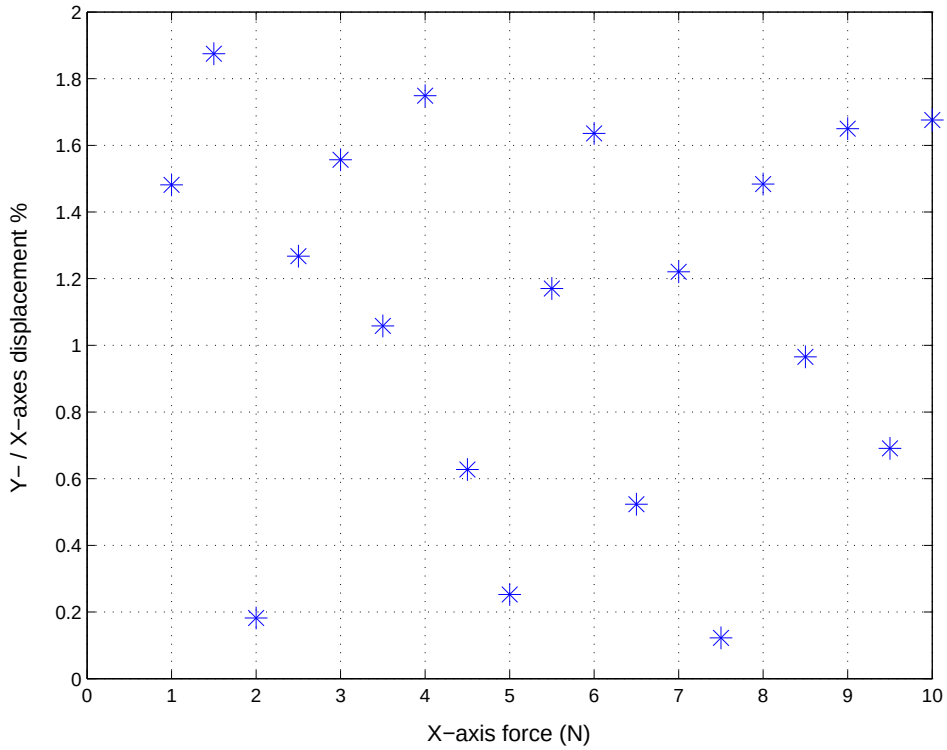

(a) Y/X error

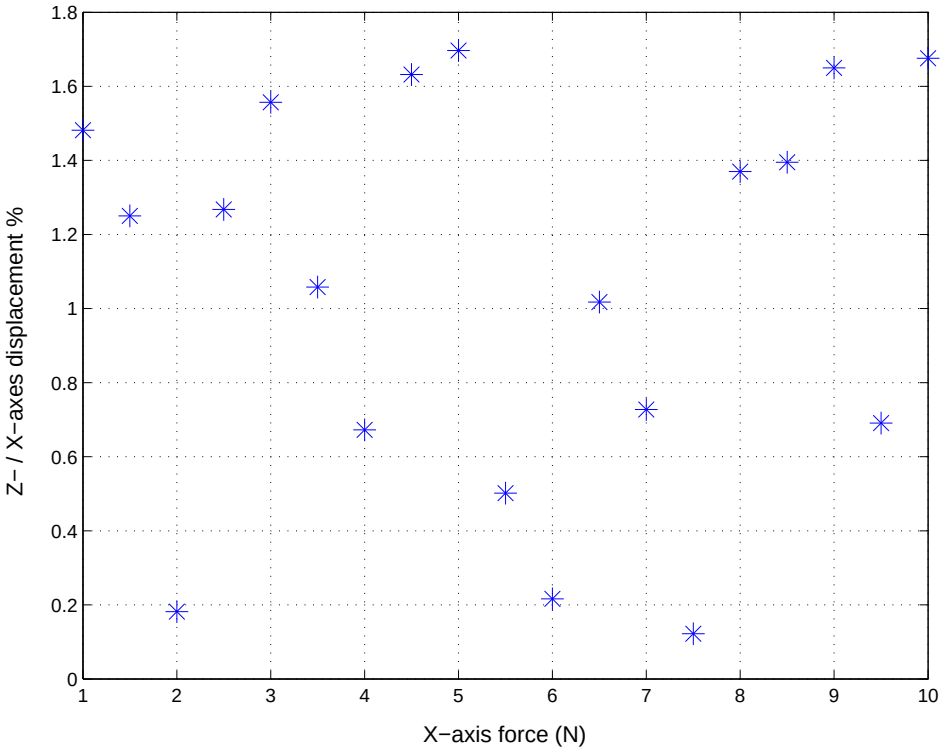

(b) Z/X error

Figure 6.8: X-axis cross-axis errors

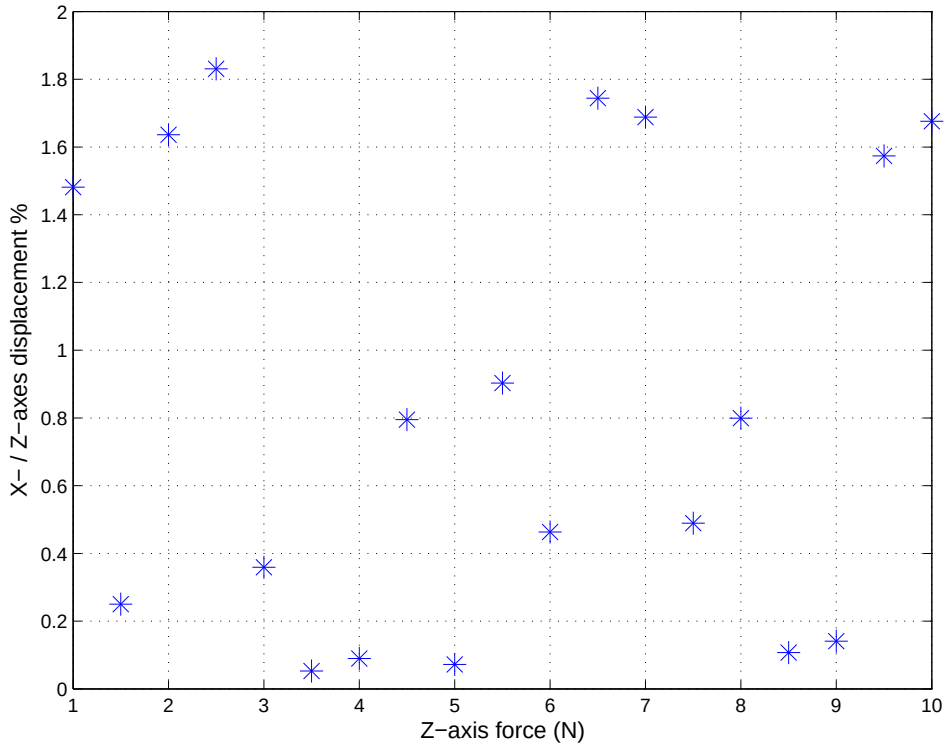

(a) X/Z error

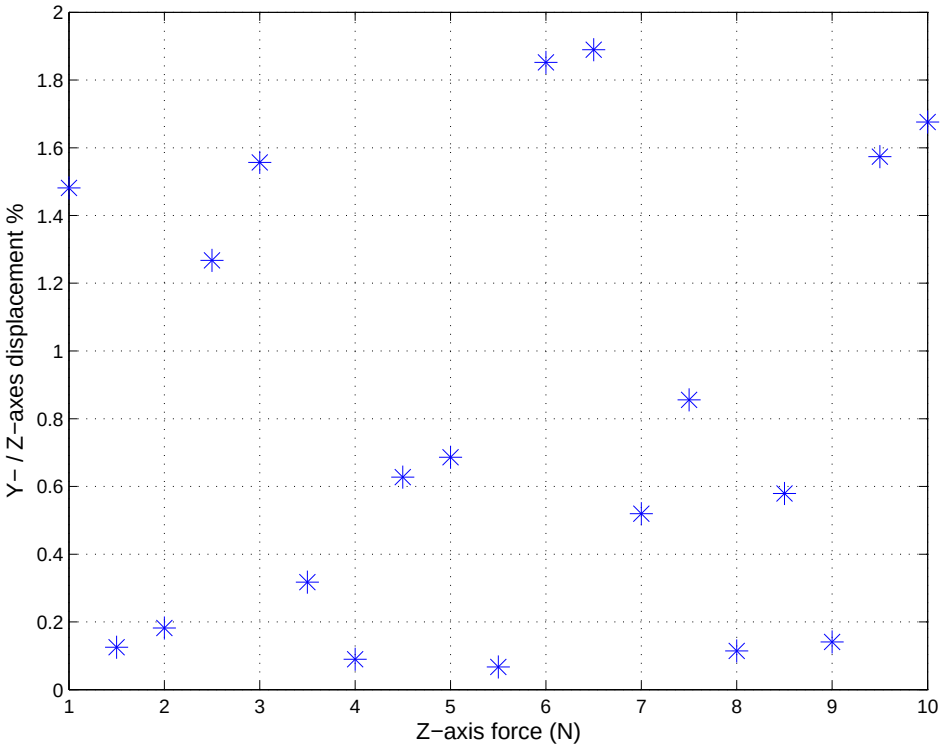

(b) Y/Z error

Figure 6.9: Z-axis cross-axis errors

Table 6.8: Results of cross-axis error of 3-PPP *XYZ*-FPM

Actuated motion	Unactuated motion	Maximum cross-axis error
X	Y	1.9%
	Z	1.7%
Y	X	2%
	Z	1.7%
Z	X	1.8%
	Y	1.9%

Table 6.9: Results of the cross-axis error of the 3-PPP *XYZ*-FPM

$F_X - \theta_Y$	$F_Y - \theta_X$	$F_Z - \theta_Y$
1.5 mrad	1.3 mrad	1.3 mrad

by minimizing the ratio of λ defined in Section 5.2. The rotary errors are measured here, listed in Table 6.9. The maximum angular motion is smaller than $1.5mrad$.

6.4 Modal Analyses of 3-PPP *XYZ*-FPM

In this section, the modal analyses of the 3-PPP *XYZ*-FPM are conducted. the FEM simulation is conducted to study the mode shapes, that is how the 3-PPP *XYZ*-FPM deforms. The hammer test is conducted to obtain the natural frequencies corresponding to the simulated mode shapes, that is under what kind of stimulations the 3-PPP *XYZ*-FPM can operate.

6.4.1 FEM Simulation for Mode Shapes

The modal analysis is implemented for evaluating dynamic performances of the 3-PPP *XYZ*-FPM. Since flexure hinges have infinite flexibility, not only one-axis motion is activated. Usually the motion of the flexure mechanism is the combination of several mode shapes. The modal analysis studies what kinds of mode shapes are activated and how they are stimulated.

According to the selected material of AL 7075, in ANSYS, the material properties are defined with Young's modulus E of $72GPa$, Poisson's ratio of 0.33 and density of $2800kg/m^3$. Then the solid model is established, and it is required to be meshed for further static analysis and modal analysis. The element for meshing is selected as 20-node SOLID95 for achieving high accuracy of the simulation results.

The displacement constraints are applied according to the actual experimental setup before performing analyses. Three VCAs are mounted on W_1, W_2 and W_3 joints, and each actuator will activate one-axis translational motion and constrain two other axis translational motions. Thus, each prismatic joint is allowed for its sensitive-axis motion and constrained for two other axes. W_1 joint is allowed to move along the X-axis and fixed along the Y- and Z-axes. Similarly, W_2 joint is allowed to move along the Y-axis and fixed along the X- and Z-axes. W_3 joint is permitted to move along the Z-axis and fixed along the X- and Y-axes.

By checking the modal results, it is found that the following three mode shapes contribute to the operation of the 3-PPP *XYZ*-FPM. The first-, second- and third-orders mode shapes describe the translational motions along the X-, Y- and Z-axes, which are desired, as shown in Fig. 6.10(a), Fig. 6.10(b) and Fig. 6.10(c). The eighth mode shape (shown in Fig. 6.10(d)) is facile to occur when the translational motion operates. Other mode shapes are not related to the actual deformations when the X-, Y- and Z-axes motions are actuated. Existing of the eighth mode shape partially explains the parasitic rotations at the end-effector listed in Table 6.8. The eighth mode shape is caused by the parasitic motions of the prismatic joints. As illustrated in Fig. 6.11, the desired deformation of the single prismatic joint is to generate the translational motion. Actually, the parasitic

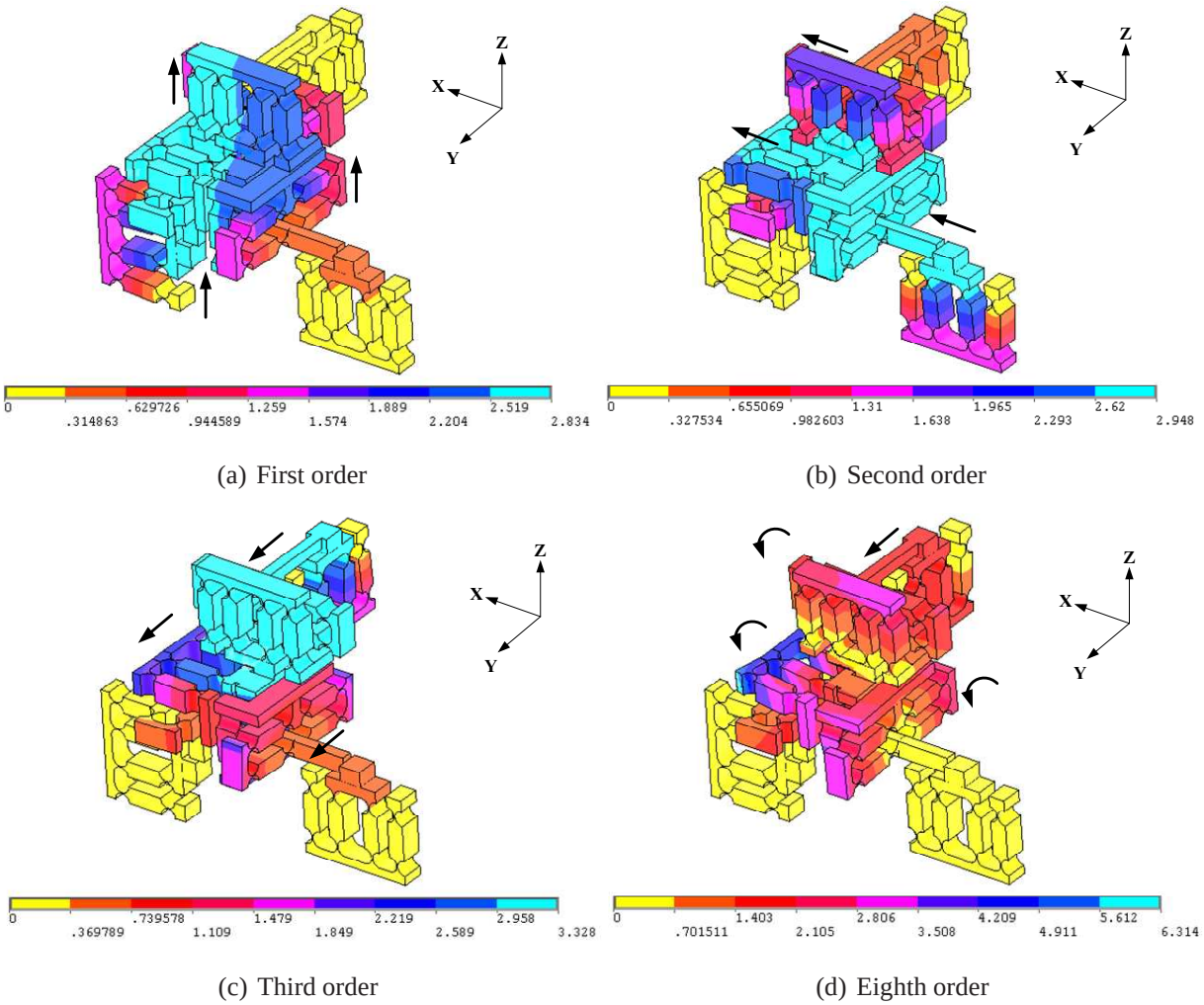

(a) First order

(b) Second order

(c) Third order

(d) Eighth order

Figure 6.10: Mode shapes of 3-PPP *XYZ*-FPM

bending occurs in the prismatic joints, when nine pieces of prismatic joints are assembled as shown in Fig. 5.2. The parasitic bending of the prismatic joint is transferred to the end-effector, and the parasitic rotation occurs. In the above analytical modeling, the first-, second- and third-orders mode shape are considered, but the eighth mode shape is difficult to be modeled. Therefore, the eighth mode shape is regarded as the unmodelled uncertainty. In the control algorithm design, the problem of the unmodeled uncertainty will be solved. The corresponding natural frequencies are listed in Table. 6.10.

6.4.2 Hammer Test for Natural Frequency

The hammer test is conducted to obtain the natural frequencies for the translational motions simulated by ANSYS. The experimental setup is shown in Fig. 6.12. The working

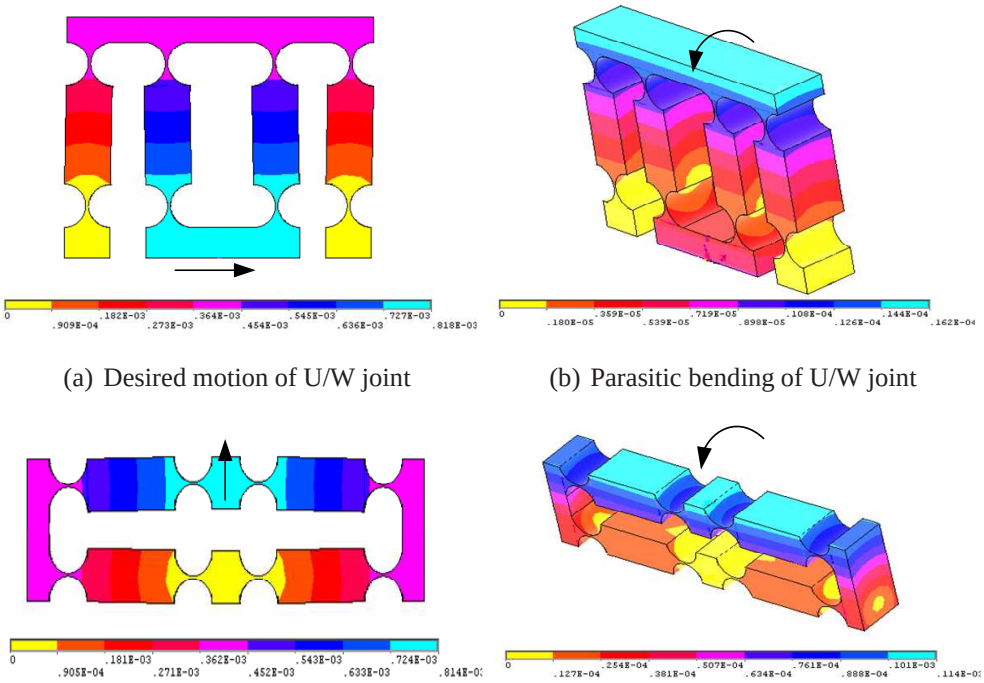

(a) Desired motion of U/W joint (b) Parasitic bending of U/W joint

(c) Desired motion of V joint (d) Parasitic bending of V joint

Figure 6.11: Mode shapes of prismatic joint

Table 6.10: Natural frequencies of 3-PPP *XYZ*-FPM by ANSYS

Mode shape	Natural frequency (Hz)
1	76.265
2	80.360
3	82.276
8	230.770

Table 6.11: Specifications of accelerometer

Measuring Range	± 500 g
Sensitivity	10.26 mv/g
Resonant Frequency	70.0 KHz

Table 6.12: Results of natural frequencies of 3-PPP *XYZ*-FPM

		Experiment	PRB	ANSYS	Nonlinear method
Natural frequency	X	56Hz	78Hz	80Hz	66Hz
	Y	50Hz	85Hz	82Hz	72Hz
	Z	50Hz	73Hz	80Hz	62Hz

principle of the hammer test is to stimulate the mechanism, and to measure the acceleration of the end-effector. The acceleration data in the time domain is transferred to those in the frequency domain using Fourier function. From the data in the frequency domain, the natural frequencies can be obtained. A pulse force is fed by a hammer impact at W_1 joint along the X-axis. The accelerometer listed in Table 6.11 is attached on the end-effector to track the dynamic responses of the 3-PPP *XYZ*-FPM. The sampled acceleration data are computed in the Fourier analyzer, and the natural frequencies can be obtained, as shown in Fig. 6.13. The first natural frequency is about $56Hz$, and the corresponding mode shape of this natural frequency is the first mode shape obtained from the ANSYS simulation in the previous section. The same procedures are applied to measure the natural frequencies for the Y- and Z-axes translational motions in Fig. 6.14 and Fig. 6.15. The results of the natural frequencies from the experiment, the PRB method using (5.24), the ANSYS simulation and the exact modeling method using (5.38) are listed in Table 6.12. These results also verify the proposed exact modeling method is more accurate than the conventional PRB method.

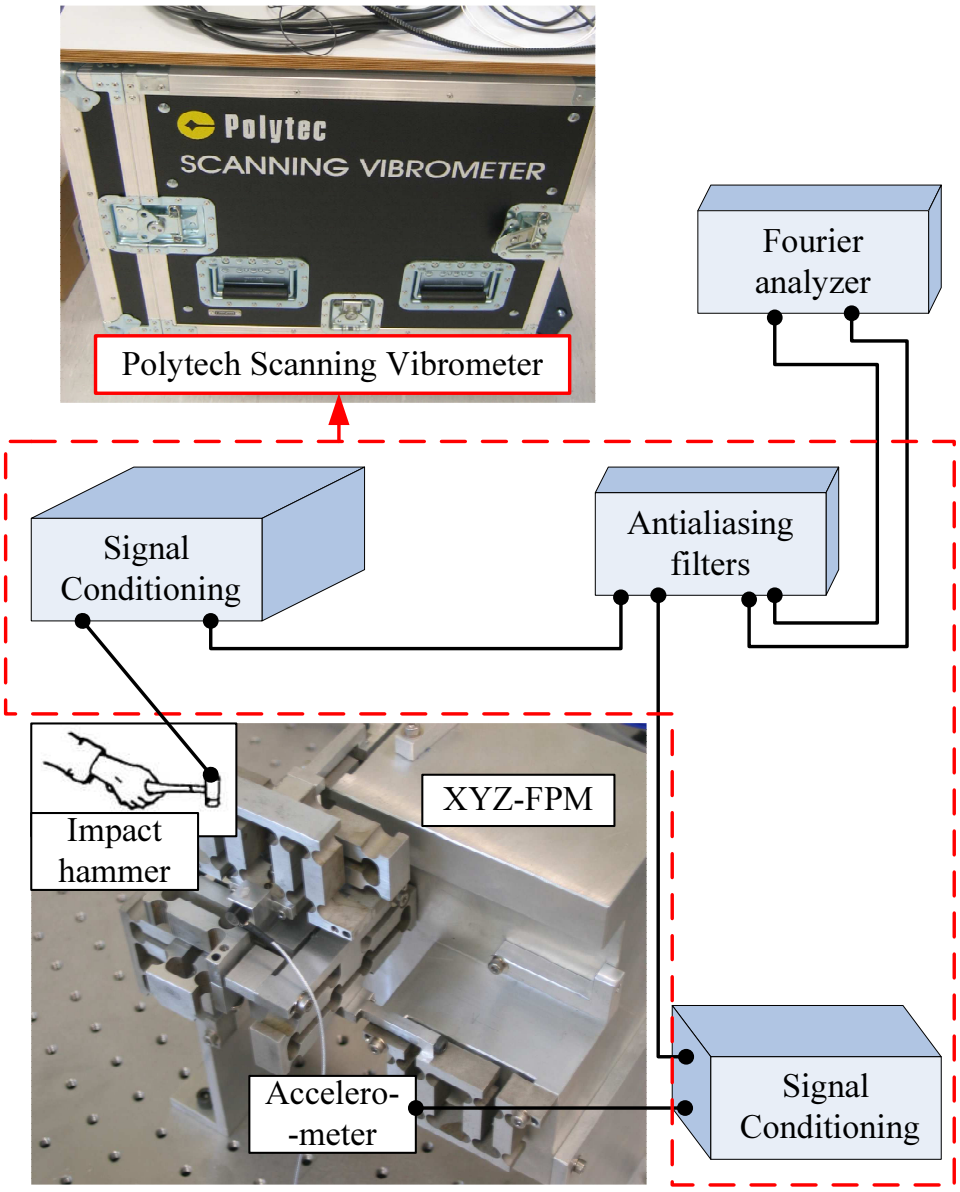

Figure 6.12: Schematic diagram of hammer test

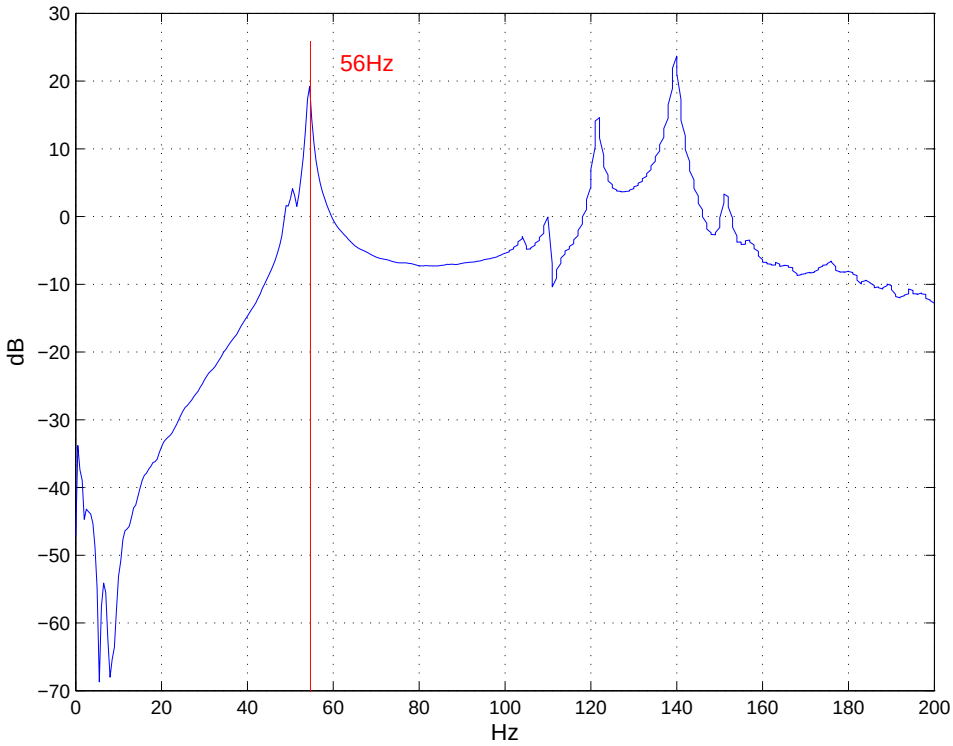

Figure 6.13: X-axis natural frequencies of 3-PPP *XYZ*-FPM

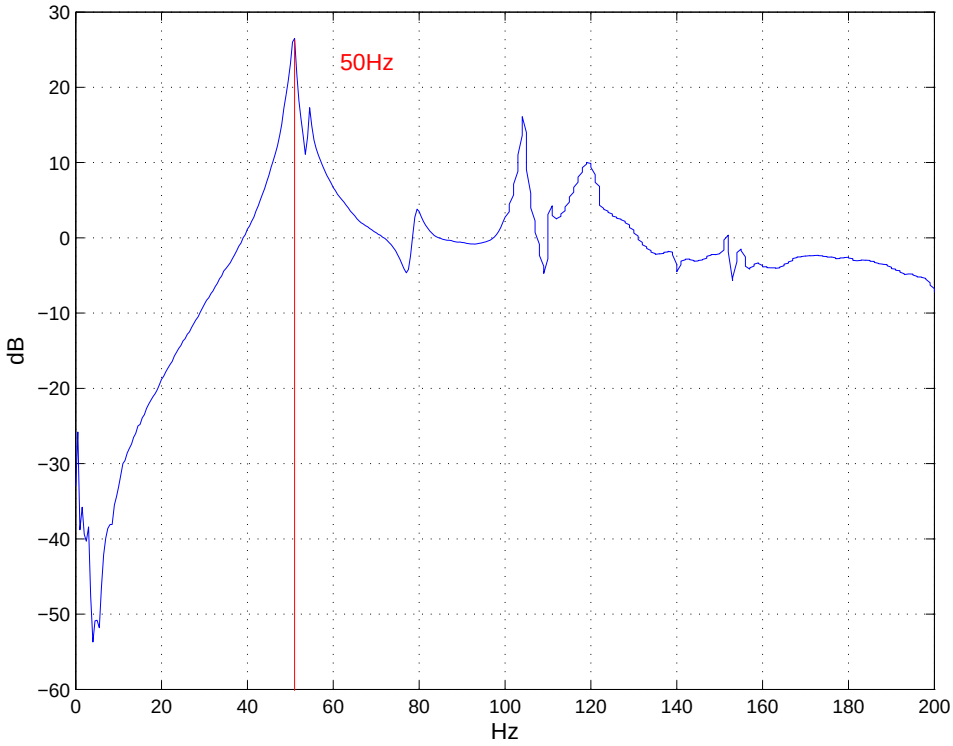

Figure 6.14: Y-axis natural frequencies of 3-PPP *XYZ*-FPM

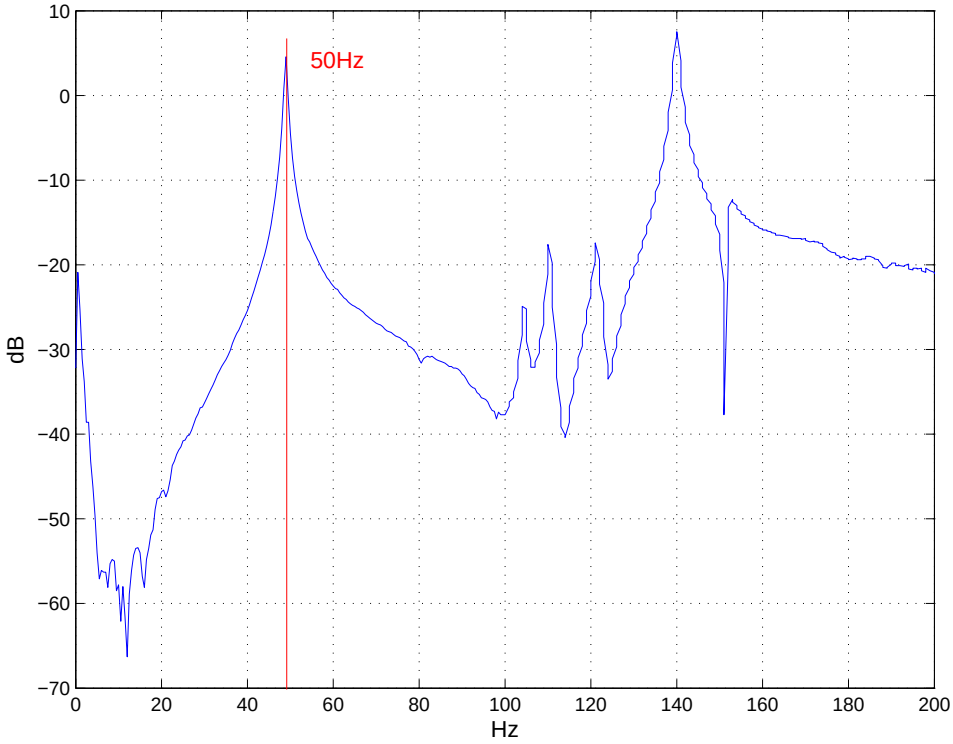

Figure 6.15: Z-axis natural frequencies of 3-PPP *XYZ*-FPM

6.5 Summary

The stiffness measurement of the single prismatic joint has been conducted to verify the proposed exact modeling method. The experimental results show that the exact modeling method has been more accurate than the conventional PRB method. The stiffness of the 3-PPP *XYZ*-FPM is also measured to validate this method. The decoupled kinematic structure of the 3-PPP *XYZ*-FPM is also verified. The experimental results show that the cross-axis errors of the 3-PPP *XYZ*-FPM are within 2%, and the parasitic rotations are smaller than $1.5mrad$. The ANSYS simulation has been performed to study the mode shapes of the 3-PPP *XYZ*-FPM, and the results explain the parasitic rotation. The hammer test has been conducted to obtain the natural frequencies for the translational motions.

Chapter 7

Robust Control Algorithm Design and Implementation

The 3-PPP *XYZ*-FPM is expected to achieve a high positioning precision of $0.1\mu m$ and a fast dynamic response with a short settling time. To achieve these two requirements, several common problems of flexure mechanisms must be solved. It is the reason why the controller is introduced to the flexure-based micromanipulator. In this chapter, the common problems of flexure mechanisms, deteriorating the positioning precision and the dynamic response, are investigated and summarized. A hybrid controller with position control and vibration control with high robustness is designed and implemented for the 3-PPP *XYZ*-FPM.

7.1 Problems of Flexure Mechanisms

Generally, there are three problems, which are common in flexure mechanisms, deteriorating the positioning precision and the dynamic response. The three common problems are explained as follows.

- Unmodeled mode shapes and unmodeled parameters
  Since flexure hinges or flexible components possess multi-axis flexibility, multi-mode shapes of flexure mechanisms are stimulated in the actual operation. In

derivation of the dynamic equations of flexure mechanisms, only low-order mode shapes describing the expected deformations are considered. High-order mode shapes are difficult and usually neglected in the dynamic equations. Hence, omission of high-order mode shapes introduces unmolded mode shapes into the analytical dynamic model.

Although the expected low-order mode shapes are formulated, it is also difficult to describe the actual deformations of flexible components. Hence, there are unmodeled parameters in the matrices of mass and stiffness in the dynamic equations.

Unmodeled mode shapes and unmodeled parameters are called as unmodeled uncertainties. Unmodeled uncertainties make it difficult for controllers to achieve high positioning precision.

- Vibration

  Different from rigid-body mechanisms, flexure mechanisms have no the assembled joints, where friction is generated. Friction contributes to damping of rigid-body mechanisms. In flexure mechanisms, damping originates from thermal dissipation during elastic deformation. Thermal dissipation in flexure mechanisms is far smaller than friction in rigid-body mechanisms. Accordingly, vibration caused by low damping is another common problem in flexure mechanisms. Thus, vibration is required to be suppressed to ensure fast dynamic response.

- External disturbances

  The expected positioning precision of flexure mechanisms is usually high to micrometer- or submicrometer-scale. Even small external disturbances can affect random positioning errors. Thus, sensitivity to external disturbances is needed to be restrained to ensure the positioning precision and the fast dynamic response.

In order to solve the above three problems, the controller must possess the following characteristics.

- High robustness

  Unmodeled uncertainties and external disturbances are both difficult to be formulated by the exact models. Thus, the conventional control algorithms, which

require the exact dynamic equations, e.g. PID control, are not suitable to flexure mechanisms, because the parameters of the controllers are fixed and cannot compensate the variances in the closed-loop system. Response changes caused by unmodeled uncertainties and external disturbances can only be described by an enveloping boundary. With knowledge of the enveloping boundary, the robust controller can ensure the expected high positioning precision of flexure mechanisms.

- Hybrid algorithm with position control and vibration control
  Position control with high robustness is not complete to ensure a good response of the flexure mechanisms. Evaluation of a good response includes a high positioning precision and a fast dynamic response with a short settling time. Vibration is an inherent phenomena of flexure mechanisms, because of low damping, and may elongate the settling time. Vibration control is required to be incorporated to ensure a fast dynamic response.

Thus, to ensure a good response with a high positioning precision and a fast response, a hybrid controller with position control and vibration control is necessary to be developed for flexure mechanisms. Here, a hybrid controller with high robustness is designed based on the H_∞-theory and implemented in the developed 3-PPP *XYZ*-FPM.

7.2 Preliminaries of H_∞-Control

The robust H_∞-control theory [69] is suitable to the system with multiple sources of uncertainties, noises and disturbances, as shown in Fig. 7.1(a). In our project, we cover the synthesis problem. The synthesis problem is defined as designing a controller so that the controlled signals satisfy the desired properties for all admissible noises, disturbances and model uncertainties. Most of the synthesis problems can be carried out in a unified linear fractional transformation (LFT) framework, as shown in Fig. 7.1(b). Let P be the interconnection matrix, K be the controller, $\triangle$ be the set of all possible uncertainties, w be a vector signal including noises, disturbances and reference signals, z be a vector

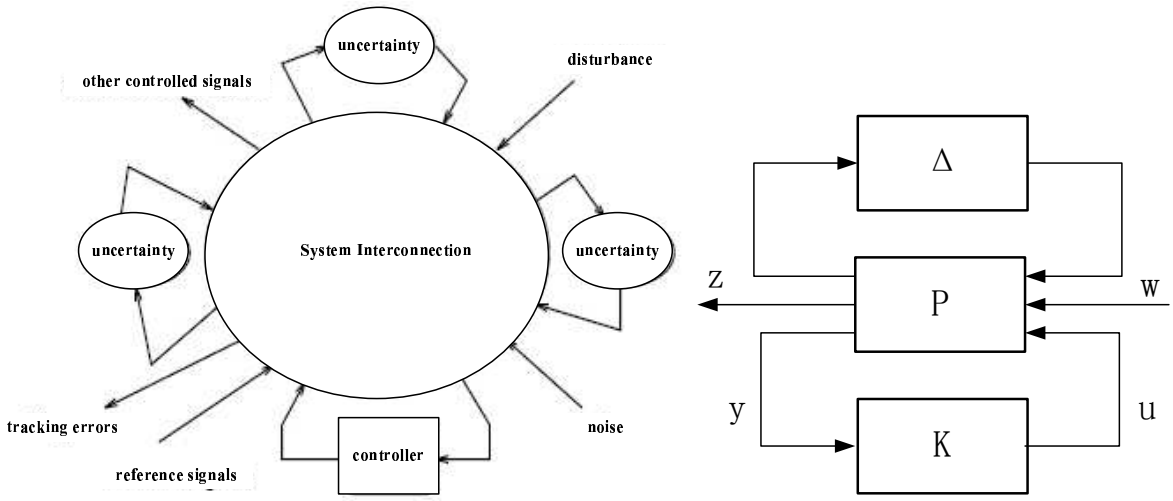

(a) General system interconnection (b) General LFT framework

Figure 7.1: H_∞-control system

signal including all controlled signals and tracking errors, u be the control signal, and y be the measured displacement at the end-effector.

Define T_{zw} as the transfer matrix from w to z, and assume that the admissible uncertainty Δ satisfies $\|\Delta\|_\infty < 1/\gamma_p$ for some $\gamma_p > 0$. The synthesis problem is to design a controller K so that the closed-loop system is stable for all admissible Δ and $\|T_{zw}\|_\infty \leq \gamma_p$ for some prespecified $\gamma_p > 0$, where $\|T_{zw}\|_\infty$ is the H_∞ norm defined as $\|T_{zw}\|_\infty = sup_\omega \overline{\sigma}(T_{zw}(j\omega))$.

For multiple sources of uncertainties, μ-synthesis is used to obtain the controller K. The general LFT framework in Fig. 7.1(b) can be converted to that in Fig. 7.2(a).

$$M(s) = F_l(P(s), K(s)) = \begin{bmatrix} M_{11} & M_{12} \\ M_{21} & M_{22} \end{bmatrix}, \tag{7.1}$$

where $\overline{\Delta}$ is a $n \times n$ block diagonal, and M includes all the weight functions,

$$\overline{\Delta}(s) = \{diag\,[\delta_1 I_{r1}, \cdots, \delta_S I_{rS}, \Delta_1, \cdots, \Delta_F] : \ \delta_i \in C, \ \Delta_j \in C^{m_j \times m_j}\}. \tag{7.2}$$

The value of μ is defined as

$$\mu_{\overline{\Delta}}(M_{11}) = \frac{1}{min\{\sigma_{max}(\Delta) | \Delta \in \overline{\Delta}, det(I - M_{11}\Delta) = 0\}}. \tag{7.3}$$

Thus, the controller design can be briefly explained that, assume that the admissible uncertainty Δ in Fig. 7.1(b) satisfies $\|\Delta\|_\infty < 1/\gamma_p$ for some $\gamma_p > 0$, the synthesis problem

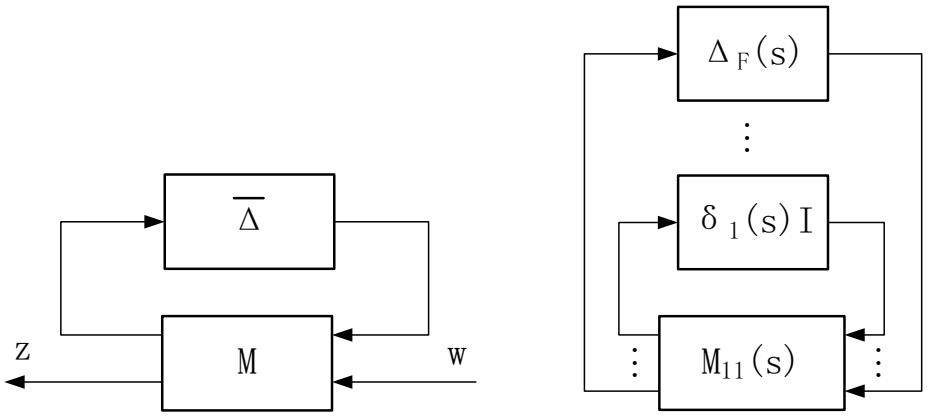

(a) Analysis framework

(b) Robust stability analysis framework

Figure 7.2: μ-synthesis

is to design a controller K so that the closed-loop system is stable for all admissible Δ, that is, $sup\mu_{\overline{\Delta}}(M_{11}(j\omega)) \leq 1/\gamma_p$. For actual design of implementation, MATLAB has the μ-synthesis toolbox aiding the solution of K controller.

7.3 Experimental Setup

The experimental system is set up for the open-loop identification and the closed-loop control implementation. The open-loop identification aims at measurement of the open-loop responses and obtaining the boundaries of uncertainties of the entire system. The boundaries of uncertainties will be used to the following control algorithm design.

The closed-loop system is established for implementation of the designed controller, as shown in Fig. 7.3 and Fig. 7.4. One control cycle operates in the following manner. The controller sends out a voltage signal to the linear amplifier, according to the expected displacement at the end-effector. The current converted from the voltage by the linear amplifier is the input of the VCA, and the VCA generates a force pushing the 3-PPP *XYZ*-FPM. The 3-PPP *XYZ*-FPM deforms and the translational motion at the end-effector along the actuation direction is measured by the encoder. The actual displacement at the end-effector is fed into the controller through the digital input interface. The difference between the expected value and the actual one is calculated, and the compensation voltage is computed based on the predetermined control algorithm. After one control cycle

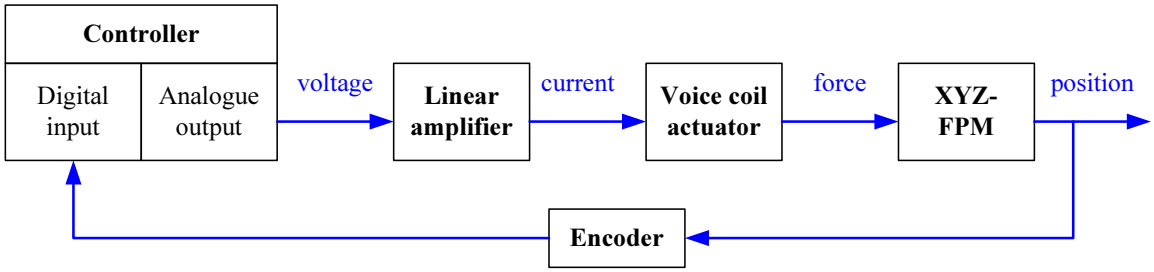

Figure 7.3: Signal flow of a closed-loop system

is finished, the next cycle is triggered until the desired positioning precision is achieved.

The four-axis controller, I-8430 Embedded Controller manufactured by ICP DAS [98], provides four-channel analogue outputs in conjunction with the actuators, the eight-channel analogue inputs, and the three-axis digital inputs and outputs for encoder feedback and encoder blocks. The controller has compatibility with MATLAB/Simulink, and can support the model-based control design approach. It means that the control algorithm designed in MATLAB/Simulink can be downloaded to the microchip integrated in the controller via the RS232 interface or the network. The microchip takes responsibilities of error computation and compensation calculation. The cycle time is selected as $0.2ms$, and the real-time control can be implemented.

The linear amplifier TA115 by Trust Automation INC. [99], which is a small-size brush-type motor, is used to convert the voltage signals sent out from the controller to the current signals, and the current signals drives the VCA introduced in Chapter 5. Another amplifier is the PWM-type, such as Cello Digital Servo Drive by Elmo Motion Control Ltd. [100]. However, the PWM amplifier introduces the ripple into the closed-loop system as the input noise, which may reduce the positioning precision of the 3-PPP *XYZ*-FPM. Thus, the linear amplifier is selected in this research work.

The displacement sensor mounted at the end-effector is Mercy 3500 SS-350c by MicroE Systems [101]. The resolution is $20nm$, and the maximum speed is $576mm/s$.

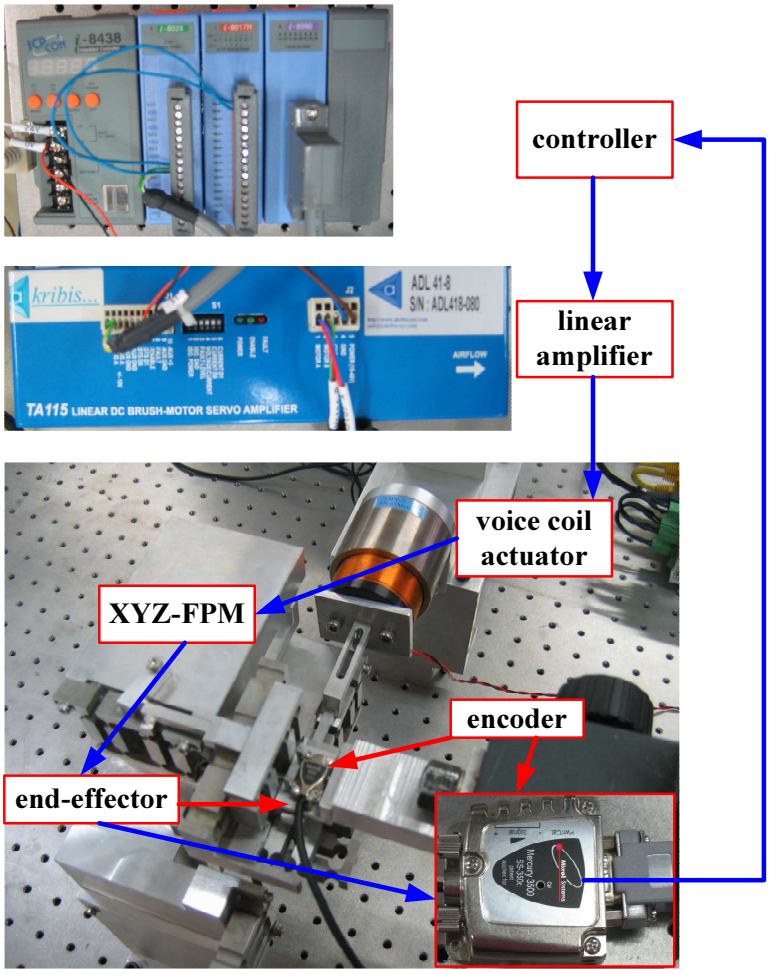

Figure 7.4: Hardware of closed-loop system

7.4 Robust Algorithm Design of Robust Position and Vibration Control

7.4.1 Closed-Loop System Configuration

The robust control system of the 3-PPP *XYZ*-FPM is designed shown in Fig. 7.5. The parameters in Fig. 7.5 are explained as follows.

- $K_{(s)}$ is the designed controller.
- $G_{(S)}$ is the nominal dynamic model including the actuator and the 3-PPP *XYZ*-FPM.
- r is the reference signal.
- y is the actual displacement at the end-effector of the 3-PPP *XYZ*-FPM.
- e is the displacement error signal.
- u is the output of the controller.
- d is the disturbance from the unmodeled uncertainties.
- Z_1, Z_2 and Z_3 are the external outputs.
- Output weight function $W_{Z1}(s)$ determines the bandwidth and the steady-state error of the closed-loop system.
- Output weight function $W_{Z2}(s)$ describes the additive uncertainties in the dynamics model.
- Output weight function $W_{Z3}(s)$ penalizes excitation of the first flexible mode and thus provides for vibration damping.

The closed-loop system in Fig. 7.5 can be formulated as the standard format in Fig. 7.6. The objective can be briefly explained as controller design to ensure the expected tracking performance and vibration suppression with robustness to the unmodeled uncertainties and noises. To ensure the tracking performance, i.e., the positioning precision, the

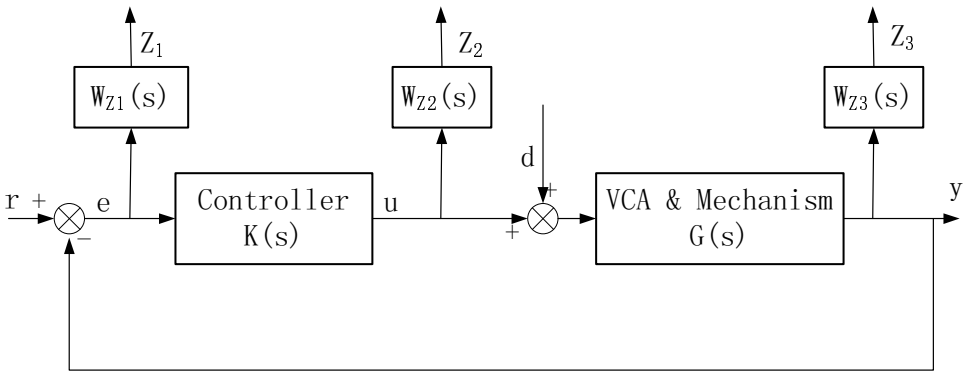

Figure 7.5: Block diagram of robust control system

reference signal r must be the external input. To achieve robustness to the unmodeled uncertainties, d must also be the external input. Thus, the external inputs are the vector $W = [r,\, d]$. Vector $Z = [\,Z_1,\, Z_2,\, Z_3]$ is the external outputs, and $P(s)$ is the generalized plant. The controller $K(s)$ is what we plan to design. The output weight functions $W_{Z1}(s)$, $W_{Z2}(s)$ and $W_{Z3}(s)$ are determined from the expected performance and are estimated from the open-loop responses.

The $G(s)$ is the transfer function of the translational motion of the 3-PPP *XYZ*-FPM and the VCAs, and it is also called as the nominal model. It is determined by the analytical dynamic model of the 3-PPP *XYZ*-FPM and the parameters of the VCAs. In (5.20), the dynamic equation for the translational motion of the 3-PPP *XYZ*-FPM has been formulated. The coil weight of the VCA is $0.316Kg$, and this mass is attached on the flexure mechanism. Thus, the dynamic equation for the translational motion including the flexure mechanism and voice coil actuator is given as using the $N - Kg - N/m$ unit

$$\begin{bmatrix} F_X \\ F_Y \\ F_Z \end{bmatrix} = \begin{bmatrix} 0.4425 & 0 & 0 \\ 0 & 0.4225 & 0 \\ 0 & 0 & 0.4625 \end{bmatrix} \begin{bmatrix} \ddot{X} \\ \ddot{Y} \\ \ddot{Z} \end{bmatrix} + \begin{bmatrix} 25400 & 0 & 0 \\ 0 & 25400 & 0 \\ 0 & 0 & 25400 \end{bmatrix} \begin{bmatrix} X \\ Y \\ Z \end{bmatrix}.$$

The transfer function of the X-axis translational motion can be given as

$$G(s) = \frac{1}{0.4425s^2 + 25400}. \tag{7.4}$$

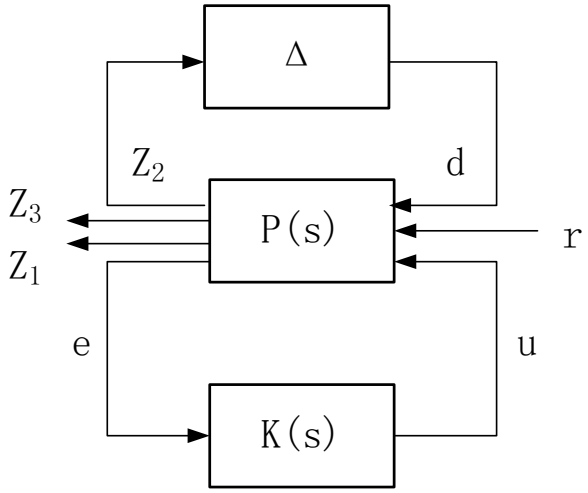

Figure 7.6: H_∞-control system

7.4.2 Dynamic Responses of Open-Loop System

The open-loop dynamic responses in the time domain under eight different input forces along the X-axis are measured and plotted in Fig. 7.7. From Fig. 7.7, it can be seen that there exist vibration lasting about $0.5s$ and ripple caused by the external noises.

Using MATLAB/Ident toolbox, the models of the eight open-loop dynamic responses are identified as

$$G_1(s) = \frac{-1.92 \times 10^{-4}s^4 + 0.4556s^3 + 218s^2 + 3.16 \times 10^5 s + 1.563^8}{s^5 + 2134s^4 + 5.42 \times 10^5 s^3 + 9.159 \times 10^8 s^2 + 4.54 \times 10^{10} s + 3.817 \times 10^{13}}, \tag{7.5}$$

$$G_2(s) = \frac{1.513 \times 10^{-4}s^3 + 0.1326s^2 + 108.2s + 7.558 \times 10^4}{s^4 + 50.08s^3 + 4.313 \times 10^5 s^2 + 1.172 \times 10^7 s + 1.815 \times 10^{10}}, \tag{7.6}$$

$$\begin{aligned} G_3(s) &= \frac{0.0001758s^5 + 0.1233s^4 + 198.4s^3 + 1.48 \times 10^5 s^2}{s^6 + 36.56s^5 + 1.015 \times 10^6 s^4 + 3.115 \times 10^7 s^3 + 2.697 \times 10^{11} s^2} \\ &\quad \frac{+5.744 \times 10^7 s + 4.334 \times 10^{10}}{+5.776 \times 10^{12} 2s + 1.055 \times 10^{16}}, \end{aligned} \tag{7.7}$$

$$\begin{aligned} G_4(s) &= \frac{1.308 \times 10^{-4}s^5 + 0.1241s^4 + 161.1s^3 + 1.482 \times 10^5 s^2}{s^6 + 38.39s^5 + 1.011 \times 10^6 s^4 + 3.133 \times 10^7 s^3 + 2.686 \times 10^{11} s^2} \\ &\quad \frac{+5.093 \times 10^7 s + 4.185 \times 10^{10}}{+5.702 \times 10^{12} s + 1.051 \times 10^{16}}, \end{aligned} \tag{7.8}$$

$$\begin{aligned} G_5(s) &= \frac{1.513 \times 10^{-4}s^5 + 0.1165s^4 + 166.7s^3 + 1.435 \times 10^5 s^2}{s^6 + 37.93s^5 + 1.011 \times 10^6 s^4 + 3.15 \times 10^7 s^3 + 2.683 \times 10^{11} s^2}, \\ &\quad \frac{+4.821 \times 10^7 s + 4.057 \times 10^{10}}{+5.771 \times 10^{12} s + 1.05 \times 10^{16}}, \end{aligned} \tag{7.9}$$

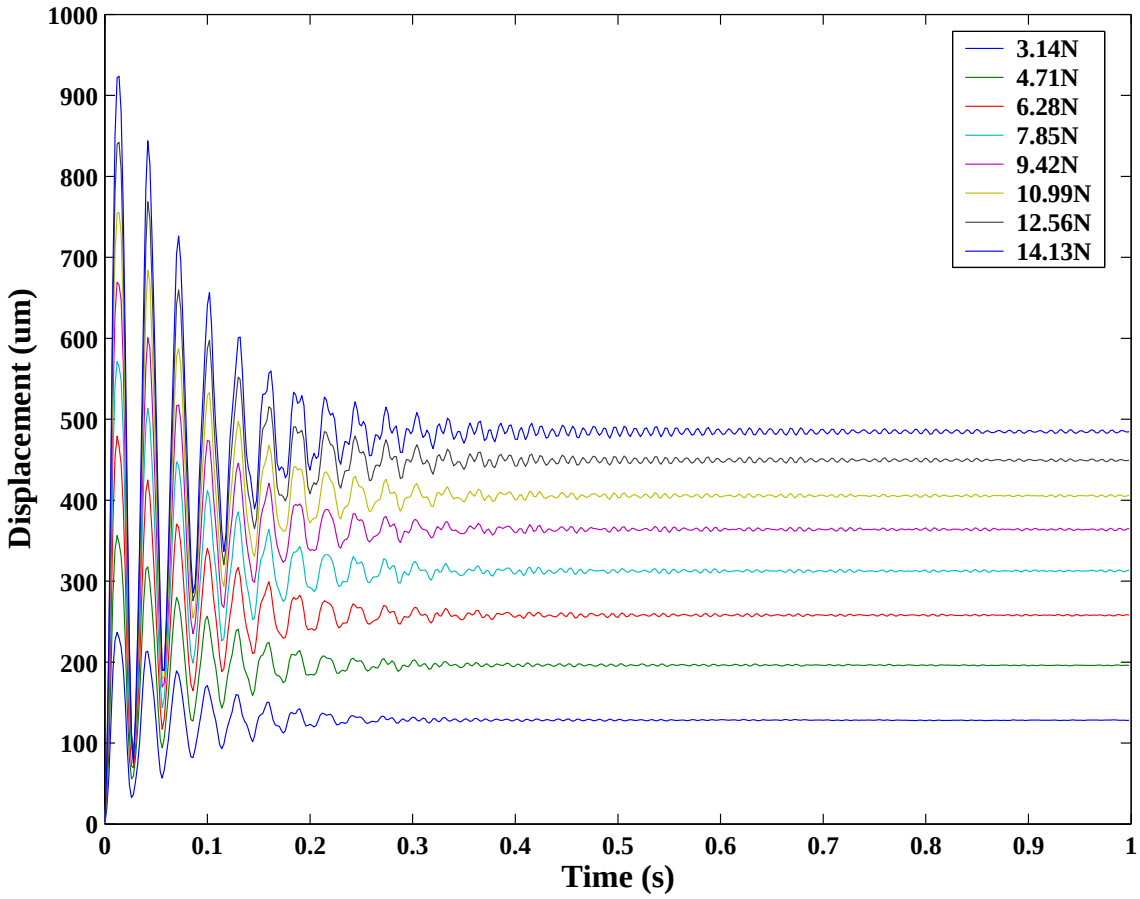

Figure 7.7: Open-loop responses in time domain

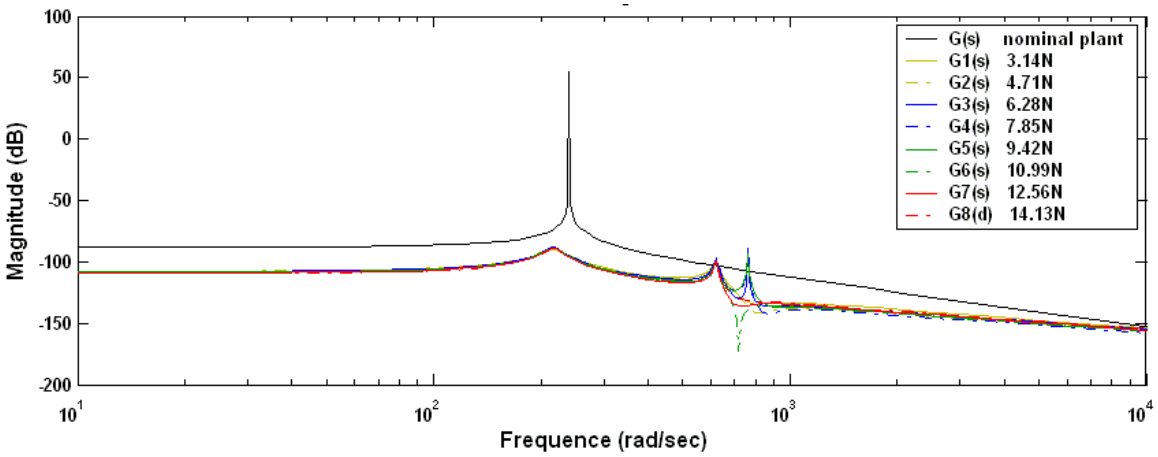

Figure 7.8: Open-loop responses in frequency domain

$$G_6(s) = \frac{1.517 \times 10^{-4}s^3 + 0.1303s^2 + 78.17s + 6.736 \times 10^4}{s^4 + 41.01s^3 + 4.333 \times 10^5 s^2 + 1.034 \times 10^7 s + 1.825 \times 10^{10}}, \tag{7.10}$$

$$G_7(s) = \frac{1.688 \times 10^{-4}s^3 + 0.1209s^2 + 74.49s + 6.491 \times 10^4}{s^4 + 33.06s^3 + 4.315 \times 10^5 s^2 + 9.68 \times 10^6 s + 1.814 \times 10^{10}}, \tag{7.11}$$

$$G_8(s) = \frac{1.88 \times 10^{-4}s^3 + 0.1039s^2 + 72.16s + 6.234 \times 10^4}{s^4 + 32.25s^3 + 4.316 \times 10^5 s^2 + 9.494 \times 10^6 s + 1.816 \times 10^{10}}. \tag{7.12}$$

The eight identified models and the nominal model (7.4) are represented in the frequency domain, as shown in Fig. 7.8. Note that in Fig. 7.8, the high-order mode shapes between $600\,rad/sec$ and $900\,rad/sec$ are activated, and not included in the nominal model. The high-order unmodeled mode shapes will be considered in the output weight function $W_{Z2}(s)$.

7.4.3 Determination of Output Weight Functions

Output Weight Function $W_{Z1}(s)$

The output weight $W_{Z1}(s)$ considers the performance criteria of the steady-state error and the closed-loop bandwidth. $W_{Z1}(s)$ gives a possibility to shape the sensitivity function $S(s)$ of the closed-loop system. The sensitivity is defined as the transfer function

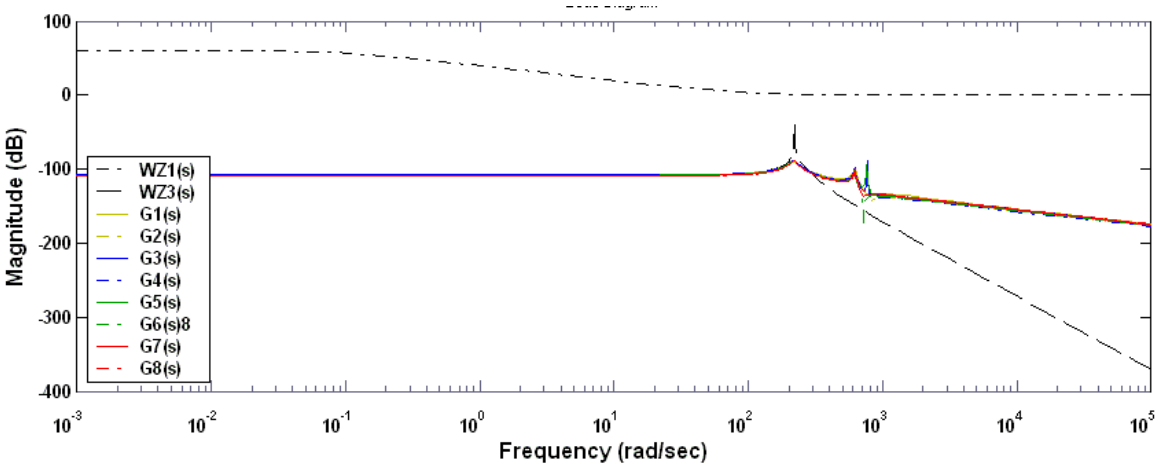

Figure 7.9: Weight functions

from e to r. The lower $\|S(s)\|$ in low frequency, the smaller the steady-state error. If $\|S(0)\|_\infty = \varepsilon$, the error in response to a step stimulation will be smaller than ε [102]. Therefore, ε is selected as the steady-state error of 10^{-4}, and the sensitivity function $S(s)$ is designed as

$$S(s) = \frac{s + 10^{-4}\omega_B}{s + \omega_B}, \tag{7.13}$$

where ω_B is the desired bandwidth of the closed-loop system. $W_{Z1}(s)$ is the inverse of $S(s)$,

$$W_{Z1}(s) = \frac{1}{S(s)}. \tag{7.14}$$

Based on the results in Fig. 7.8, it can be concluded that the natural frequency for the translational motion is about $35Hz$. It is the natural frequency of the combination of the 3-PPP *XYZ*-FPM and the VCA, and hence the value is smaller than $56Hz$ from the hammer test in Chapter 5. The bandwidth of the closed-loop system is chosen as $15Hz$, according to the value of $35Hz$. In the meanwhile, $W_{Z1}(s)$ functions as a low-pass filter in Fig. 7.9, filtering out the signals higher than $15Hz$. Therefore,

$$W_{Z1}(s) = \frac{s + 94.2}{s + 94.2 \times 10^{-4}}. \tag{7.15}$$

Output Weight Function $W_{Z2}(s)$

$W_{Z2}(s)$ describes the additive uncertainty due to the unmodeled uncertainties. The representations of the real plant $P(s)$ and the nominal plant $P_{nom}(s)$ in the frequency domain

have been plotted in Fig. 7.8. The real plant $P(s)$ can be represented using the additive uncertainty,

$$P(s) = P_{nom}(s) + W_{Z2}(s)\triangle, \tag{7.16}$$

where $P_{nom}(s)$ is the nominal dynamic model based on the analytical derivation, and $\|\triangle\|_\infty < 1$. The additive uncertainty $W_{Z2}(s)\triangle$ can be derived as

$$W_{Z2}(s)\triangle = P(s) - P_{nom}(s). \tag{7.17}$$

Based on the open-loop responses under the different inputs, the real plant $P(s)$ is equal to $G_1(s)$, $G_2(s)$, $G_3(s)$, $G_4(s)$, $G_5(s)$, $G_6(s)$, $G_7(s)$ and $G_8(s)$, respectively. Based on the analytical model, the nominal plant $P_{nom}(s)$ is equal to $G(s)$ in (7.4). Hence, $W_{Z2}(s)\triangle$, plotted in Fig. 7.10, is calculated as,

$$W_{Z2}(s)\triangle|_1 = G_1(s) - G(s), \tag{7.18}$$

$$W_{Z2}(s)\triangle|_2 = G_2(s) - G(s), \tag{7.19}$$

$$W_{Z2}(s)\triangle|_3 = G_3(s) - G(s), \tag{7.20}$$

$$W_{Z2}(s)\triangle|_4 = G_4(s) - G(s), \tag{7.21}$$

$$W_{Z2}(s)\triangle|_5 = G_5(s) - G(s), \tag{7.22}$$

$$W_{Z2}(s)\triangle|_6 = G_7(s) - G(s), \tag{7.23}$$

$$W_{Z2}(s)\triangle|_7 = G_8(s) - G(s), \tag{7.24}$$

$$W_{Z2}(s)\triangle|_8 = G_8(s) - G(s). \tag{7.25}$$

The output weight function $W_{Z2}(s)$ should envelop $W_{Z2}(s)\triangle$ in all frequencies, and is selected as

$$W_{Z2}(s) = \frac{800(s^2 + 300s + 9 \times 10^4)(s + 10^4)}{(s^2 + 500s + 6.4 \times 10^5)(s + 10^6)}. \tag{7.26}$$

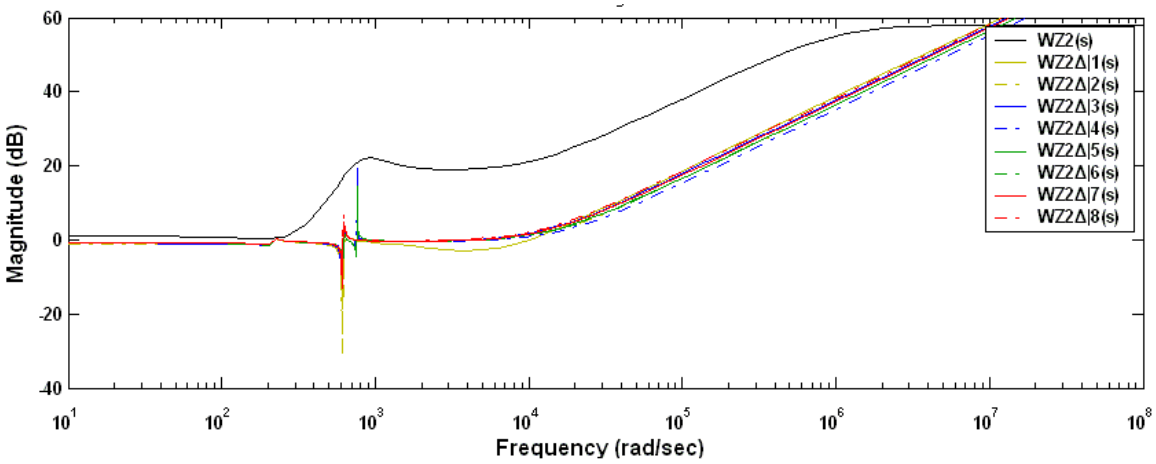

Figure 7.10: Additive uncertainty

Output Weight Function $W_{Z3}(s)$

$W_{Z3}(s)$ penalizes excitation of the first mode of the 3-PPP *XYZ*-FPM, and thus suppresses vibration at the natural frequency of the first mode. $W_{Z3}(s)$ in Fig. 7.9 is expected to increase the gain at the natural frequency of $35Hz$, and remain small constant at other frequencies [73]

$$W_{Z3}(s) = \frac{2500}{(s^2 + 0.1s + 48312.04)(s + 219.8)(s^2 + 94.2a + 63101.44)}. \tag{7.27}$$

7.4.4 μ-Synthesize with MATLAB

Using the MATLAB/μ-Toolbox, the 11-order controller $K(s)$ is synthesized. The transfer function is designed as

$$\begin{aligned} K(s) \;=\; & \frac{-6.408\times10^{-8}s^{11} + 0.01363s^{10} + 41.66s^9 + 4.144\times10^4 s^8 + 1.128\times10^7 s^7}{s^{11} + 4028s^{10} + 7.09\times10^6 s^9 + 8.082\times10^9 s^8 + 7.088\times10^{12} s^7} \\ & \frac{-1.603\times10^{10}s^6 - 3.834\times10^{13}s^5 - 3.722\times10^{16}s^4 - 1.394\times10^{19}s^3}{+4.35\times10^{15}s^6 + 1.582\times10^{18}s^5 + 4.065\times10^{20}s^4 + 1.14\times10^{23}s^3} \\ & \frac{-1.815\times10^{21}s^2 - 5.988\times10^{23}s - 5.638\times10^{22}}{+1.044\times10^{25}s^2 + 2.585\times10^{27}s + 2.437\times10^{26}}. \end{aligned} \tag{7.28}$$

Bode plot of the controller is shown in Fig. 7.11.

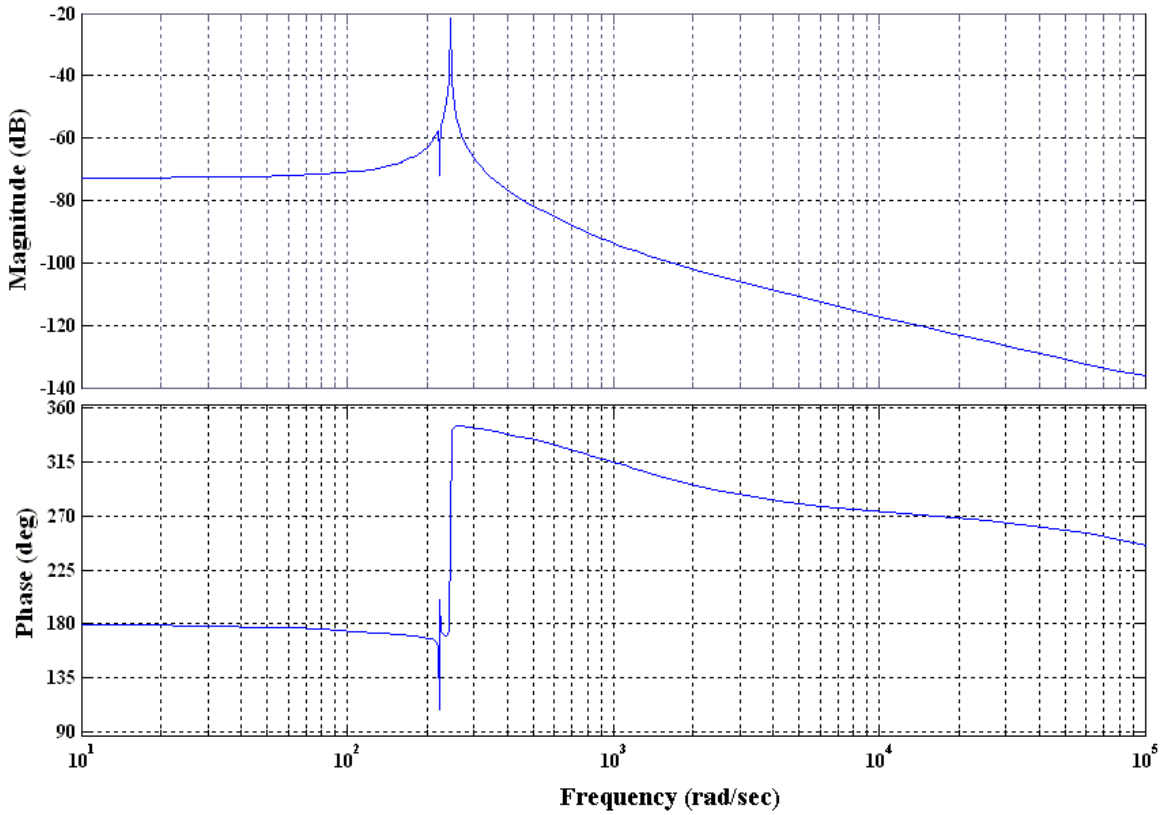

Figure 7.11: Robust Controller

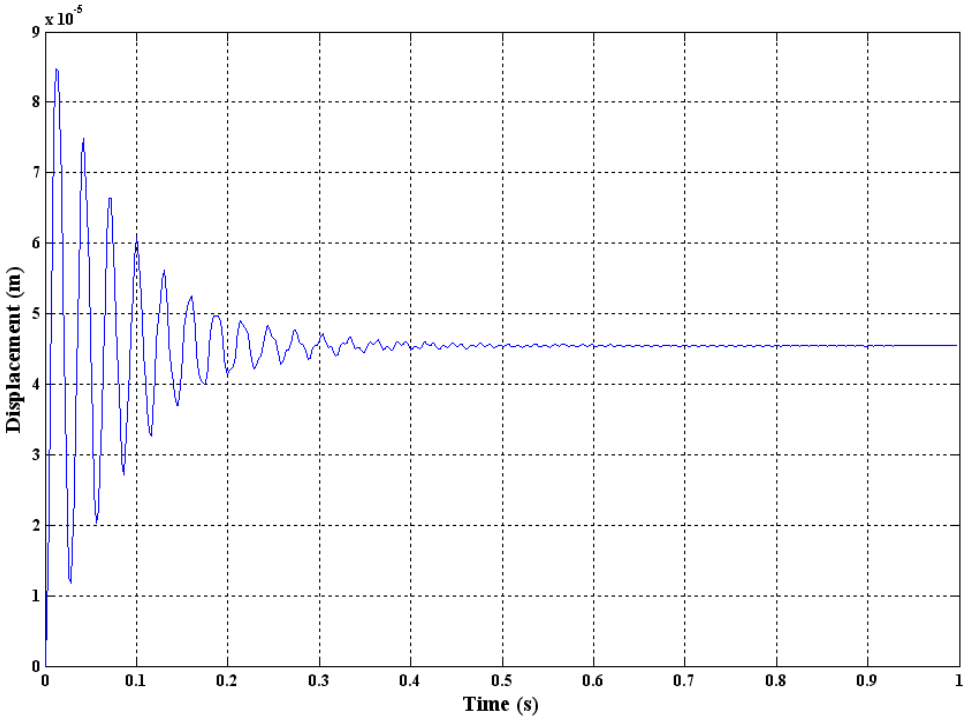

(a) Open-loop dynamic response

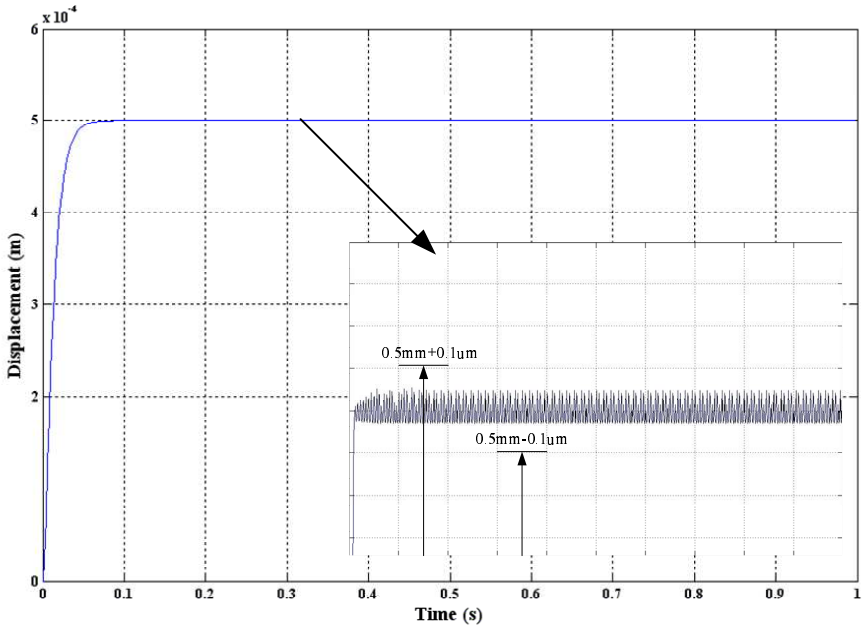

(b) Closed-loop dynamic response

Figure 7.12: Dynamic responses from experiments

7.4.5 Implementation

In order to verify the designed controller, two sets of experiments are conducted. The first experiment is to measure the open-loop responses, as shown in Fig. 7.12(a). The force $12.7N$ is generated to push the 3-PPP *XYZ*-FPM along the X-axis, and the expected translational motion of the end-effector should be $0.5mm$ based on the nominal model (7.4). However, influenced by unmodeled uncertainties, external disturbances and vibration, the actual displacement of the end-effector is $0.46mm$, with a positioning error about 8%, and oscillation lasting more than $0.5s$.

The second experiment is to implement the designed controller and measure the closed-loop response. After downloading the designed controller K into the microchip of the I-8430 Embedded Controller, the closed-loop system can operate. The same input force $12.7N$ is generated to push the 3-PPP *XYZ*-FPM along the X-axis, and the end-effector is expected to move $0.5mm$ along the X-axis. The experimental result, plotted in Fig. 7.12(b), shows that the positioning precision is improved with the positioning error within the boundaries of $\pm 0.1\mu m$, and vibration is also suppressed with a short settling time about $0.1s$.

7.5 Summary

A hybrid controller with position control and vibration control has been designed using the H_∞-theory. The controller is robust to the unmodeled uncertainties due to high-order mode shapes and unmodeled parameters of flexure mechanism, and also nonsensitive to the external disturbances. The controller also suppresses vibration caused by the inherent low damping in flexure mechanisms. The dynamic performances of the closed-loop system are improved significantly. The positioning precision of $0.1\mu m$ and the settling time of $0.1s$ are achieved.

Chapter 8

Conclusions, Contributions and Future Works

8.1 Conclusions

Structure synthesis of large-displacement and decoupled *XYZ*-FPMs

The characteristics of flexure mechanisms have been investigated, and generalized as the structure constraints. Based on these structure constraints, structure synthesis of the *XYZ*-FPMs with decoupled kinematic structures has been conducted. The 3-PPP, 3-PRRR, 3-PPRRR and 3-PRRRP structures have been designed. Moreover, a new type of large-motion prismatic joint has been designed, and functions as the fundamental modules to configure the *XYZ*-FPMs. Therefore, the synthesized decoupled *XYZ*-FPMs has the advantage of large motion range.

Exact modeling of synthesized *XYZ*-FPMs

The exact stiffness models of the synthesized *XYZ*-FPMs have been formulated, based on the lumped-compliance assumption. The compliance matrix of the RRR-limb, the module for the *XYZ*-FPM configurations, has been obtained based on the exact compliance formulation of flexure hinges. An exact modeling method, based on the continuous-compliance assumption, has been proposed and been applied to formulate the static and dynamic behaviors of the new type of prismatic joint.

Dimension optimization based on static performance

The critical static performances of flexure mechanisms include stiffness, motion range, stage size and parasitic motion. To ensure flexure mechanisms possess the high static performances, the dimension optimization approach has been generalized. Dimension determination has been formulated quantitatively as an optimal problem with the single-objective. Therefore, dimensions can easily be determined by the standard single-objective optimization algorithms.

Development of a 3-PPP *XYZ*-FPM

Based on the generalized studies of structure synthesis, exact modeling and dimension optimization, a 3-PPP *XYZ*-FPM with large motion range and decoupled kinematic structure has been developed. The experimental results show that the 3-PPP *XYZ*-FPM possesses the decoupled kinematic structure, with the small cross-axis errors below 2% and small parasitic rotations smaller than $1.5mrad$. The results also show that the 3-PPP *XYZ*-FPM has large motion range, with a workspace of $2.3mm$ and a large motion range of $1/80$. From the experimental results, the designed prismatic joint is proved to possess the a workspace of $2.3mm \times 2.3mm \times 2.3mm$ and a large motion range of 7%. The exact modeling method, applied to the designed prismatic joint and the 3-PPP *XYZ*-FPM, is verified to improve the modeling accuracy significantly. A hybrid position and vibration controller using the H_∞-theory has also been designed for achieving the positioning precision of $0.1\mu m$ and the fast response with the settling time of $0.1s$.

In summarization, compared to the current flexure mechanisms, our developed 3-PPP *XYZ*-FPM has the advantages of a large workspace, a compact stage size, a large motion range, smaller parasitic motions, high positioning precision. Comparisons are listed in Table 8.1

8.2 Contributions

This research work contributes towards development of the large-motion and decoupled *XYZ*-FPMs. This research work is important since more and more flexure mechanisms

Table 8.1: Performance comparison of flexure mechanisms

Stages	**Workspace**	**Stage size**	**Motion range** β	**Parasitic motion**	**Positioning precision**
XY [10]	$5mm \times 5mm$	$300mm \times 300mm$	$1/60$	cross-axis 0.03% rotation $0.5arcsecs$	NA
6-DOF [27]	$100\mu m \times 100\mu m \times 100\mu m$	$> 100mm \times 100mm$	$< 1/1000$	NA	$0.25\mu m$
$XY\theta_Z$ [28]	$100\mu m \times 100\mu m \times 0.1^\circ$	$> 200mm \times 200mm$	$< 1/2000$	NA	NA
XYZ [32]	$200\mu m \times 400\mu m \times 400\mu m$	$> 100mm \times 100mm \times 100mm$	$< 1/500$	NA	$0.1\mu m$

are required for micromanipulation with high positioning precision and fast response. To summarize, the contributions are:

Design of large-motion prismatic joint

The new prismatic joint has the advantages of large motion range, no parasitic motion, no buckling and no stiffening. Increasing of the motion range of the prismatic joint can enlarge the workspace of the flexure mechanism significantly. Therefore, integrating the new prismatic joint, the flexure mechanism can achieve a large workspace. If the prismatic joint has parasitic motion, the parasitic motion may be transferred or amplified at the end-effector of the flexure mechanism. Thus, the new prismatic joint without the parasitic motion can significantly reduce the parasitic motion of the flexure mechanism.

Structure synthesis of decoupled *XYZ*-FPMs

Study of structure synthesis of decoupled *XYZ*-FPMs is necessary, because low-mobility FPMs with decoupled kinematic structures are suitable and dominant for the requirement of high precision, and there is still no generic study for synthesizing decoupled *XYZ*-FPMs. Although, there are many studies for synthesizing decoupled *XYZ* rigid mechanisms, flexure mechanisms have some differences and more constraints than rigid mechanisms. These differences and constraints make structure synthesis method of flexure mechanisms different from that of rigid mechanisms. The differences and constraints are summarized, and the structure synthesis method for decoupled *XYZ*-FPMs is generalized based on the summarization.

Exact modeling

The exact modeling method for the new type of prismatic joint is useful, because it is not only an exact method based on the continuous-compliance assumption, but also it can formulate the stiffness and the dynamics of the new prismatic joint exactly. Moreover, it is generic and can be applied to a series of large-motion prismatic joints introduced in Chapter 2.

Dimension optimization based on static performances

The generalized dimension optimization method based on the static performances is necessary. The method considers the critical static performances of flexure mechanisms, including stiffness, workspace, stage size, parasitic motion and actuation ability. The previous studies about the optimal design of flexure mechanisms consider one or two items, and no study summarizes and generalizes the entire static performances based method. The generalized dimension optimization method mentioned here gives the quantitative representations of these static performances, and formulates as a single-objective optimal problem. Thus, the method can be easily applied, by obtaining the optimal solution via the standard single-objective optimization algorithms.

Hybrid position and vibration control with robustness

There are three common problems in flexure mechanisms, i.e., unmodeled uncertainties caused by difficulty to model high-order mode shapes, high sensitivity of external disturbances and vibration due to the inherent low damping. The hybrid control algorithm integrates both position control and vibration control, and solves the three common problems simultaneously. Successful implementation of the designed control algorithm proves that the advanced control theory of the H_∞-theory is suitable to flexure mechanisms and the further application is meaningful.

8.3 Future Works

The future direction of this project will include following issues:

Modeling of nonsensitive-axis motion

The exact stiffness and dynamic models of the sensitive-axis motions have been derived. Moreover, in dimension optimization, small parasitic motion is considered. The cross-axis error and parasitic rotation at the end-effector are proved to be small through the experimental results. However, there is still no analytical model for formulating the nonsensitive-axis motions. In the following works, the 6×6 stiffness matrices of the synthesized *XYZ*-FPMs are needed to be formulated.

Optimal design based on dynamic performance

The natural frequency for the X-axis translational mode shape of the 3-PPP *XYZ*-FPM is $56Hz$, and this value determines the closed-loop bandwidth about $15Hz$. The smaller the natural frequency of flexure mechanisms, the narrower the closed-loop bandwidth. For purpose of fast response of the closed-loop system, the natural frequency of flexure mechanisms is expected to be high. Therefore, the dynamics-based design becomes necessary.

Bibliography

[1] Akribis Systems Pte Ltd. [Online]. Available: http://www.akribis-sys.com/

[2] LC Series Ultra-high Accuracy Laser Displacement Meters. [Online]. Available: http://www.keyence.com.sg/products/vision/laser/lc/lc.php

[3] ATI Force Sensor, Torque Sensor, Multi Axis, Six Axis Sensors, Force Transducer, Torque Transducer. [Online]. Available: http://www.ati-ia.com/products/ft/ft_models.aspx

[4] B. Salamon, "Mechanical advantage aspects in complinat mechanisms design," Ph.D. dissertation, Purdue University, West Lafayette, IN, 1989.

[5] L. L. Howell, "The design and analysis of large-deflection members in compliant mechanisms," Ph.D. dissertation, Purdue University, West Lafayette, IN, 1991.

[6] A. Midha, "A bilateral force reflecting teleoperation system for wiping operation," in *Proceedings of the IEEE/RSJ International Conference on Intelligent Robots and Systems (IROS'02)*, Lausanne, Switzerland, Oct. 2002, pp. 2899–2904.

[7] I. Her, "Methodology for compliant mechanism design," Ph.D. dissertation, Purdue University, West Lafayette, IN, 1986.

[8] N. M. Sevak and C. W. McLarnan, "Optimal synthesis of flexible link mechanisms with large static deflection," *ASME paper No. 74-DET83*.

[9] I. Her and A. Midha, "A compliance number concept for compliant mechanism and type synthesis," *ASME Journal of Mechanisms, Transmissions and Automation in Design*, vol. 109, no. 3, pp. 348–355.

[10] S. Awtar, "Synthesis and analysis of parallel kinematic xy flexure mechanisms," Ph.D. dissertation, Department of Mechanical Engineering, Massachusetts Institute of Technology, Massachusetts, USA, Feb. 2004.

[11] H. H. Pham and I.-M. Chen, "Evaluation of resolution of flexure parallel mechanisms for ultraprecision manipulation," *Review of Scientific Instruments*, vol. 75, pp. 3016–3024, Sept. 2004.

[12] A. Menciassi, A. Eisinberg, G. Scalari, C. Anticoli, M. C. Carrozza, and P. Dario, "Force feedback-based microinstrument for measuring tissue properties and pulse in microsurgery," in *Proceedings of the IEEE International Conference on Robotics and Automation*, Seoul, Korea, May 2001, pp. 626– 631.

[13] K. Furutani, R. Kudoh, and N. Mohri, "Nano cutting machine employing parallel mechanism," in *Proceedings of 16th Annual Meeting of American Society for Precision Engineering*, Arlington, Virginia, USA, 2001, pp. 164–167.

[14] (1997) CSEM scientific report. [Online]. Available: http://www.csem.ch/detailed/pdf/e_211_CCM_CSEM_1997_Scientific_Report.pdf

[15] (2001) OFR Fiber-Optic Products. [Online]. Available: http://www.ofr.com/misc/OFR_2001_Fiber.pdf

[16] N. Lobontiu, *Compliant Mechanisms: Design of Flexure Hinges*. Florida, America: CRC Press LLC, 2003.

[17] L. L. Howell, *Compliant Mechanisms*. New York, USA: Wiley, 2001.

[18] S. T. Smith, *Flexures: Elements of Elastic Mechanisms*. Amsterdam, Netherlands: Gordon & Breach Science, 2000.

[19] J. M. Paros and L. Weisbord, "How to design flexure hinges," *Machine Design*, vol. 25, pp. 151–156, Nov. 1965.

[20] N. Lobontiu and J. Paine, "Design of circular cross-section corner-filled flexure hinges for three-dimensional compliant mehcnaisms," *Journal of Mechanical Design*, vol. 124, no. 3, pp. 479–484, Sept. 2002.

[21] M. Goldfrab and J. E. Speich, "A well-behaved revolute flexure joint for compliant mechanism design," *Journal of Mechanical Design*, vol. 121, no. 9, pp. 424–429, Sept. 1999.

[22] J. H. Kim, S. Y. Kim, and Y. K. Kwak, "Development and optimization of 3-D bridge-type hinge mechanisms," *Sensors and Actuators*, vol. 116, pp. 530–538, 2004.

[23] E. Ottaviano, G. Carbone, and M. Ceccarelli, "Workspace analysis and performance of a binary actuated parallel manipulator with flexural joints," *Journal of Mechanical Engineering Science*, vol. 217, pp. 313–330, 2003.

[24] N. D. Mankame and G. K. Ananthasuresh, "Contact aided compliant mechanisms: Concept and preliminaries," in *Proceedings of DETC 2002 ASME Design Engineering Technical Conferences*, Montreal, Canada, Sept. 2002, pp. 1–13.

[25] (1996) OIWA Laboratory Website. [Online]. Available: http://oiwa.eng.shizuoka.ac.jp/field/stewart/stewart_e.htm

[26] L. Zuo, M. Kartik, M. Prakazh, N. Landsiell, M. Culpepper, and A. Slocum, "Design of six-axis compliant mechanism for nano manipulator," *Technical report 2003, MIT*.

[27] M. L. Culpepper and G. Anderson, "Design of a low-cost nano-manipulator which utilizing a monolithic, spatial compliant mechanism," *Precision Engineering*, vol. 28, no. 4, pp. 469–482, Oct. 2004.

[28] B. J. Yi, G. B. Chung, H. Y. Na, W. K. Kim, and H. Suh, "Design and experiment of a 3-DOF parallel micromechanism utilizing flexure hinges," *IEEE Transactions on Robotics and Automation*, vol. 19, no. 4, pp. 604–612, Aug. 2003.

[29] W. J. Chen, W. Lin, K. H. Low, and G. L. Yang, "A 3-DOF flexure-based fixture for passive assembly of optical switches," in *Proceedings of the IEEE/RSJ International Conference on Advanced Intelligent Mechatronics*, California, USA, July 2005, pp. 618–623.

[30] K. S. Chen, D. L. Trumper, and S. T. Smith, "Design and control for an electromagnetically driven X-Y-θ stage," *Precision Engineering*, vol. 26, no. 4, pp. 355–369, Oct. 2002.

[31] P. Pham, Y. J. Regamey, M. Fracheboud, and R. Clavel, "Orion Minangle: A flexure-based, double-tilting parallel kinematics for ultra-high precision applications requiring high angles of rotation," in *3th International Symposium on Robotics*, Tokyo, Japan, Dec. 2005.

[32] J. J. Yu, S. S. Bi, G. H. Zong, and X. J. Liu, "On the design of compliant-based micro-motion manipulators with a nanometer range resolution," in *Proceedings of the IEEE/ASME International Conference on Advanced Intelligent Mechatronics*, Kobe, Japan, July 2003, pp. 149–154.

[33] Y. Koseki, T. Tanikawa, N. Koyachi, and T. Arai, "Kinematic analysis of translational 3-DOF micro parallel mechanism using matrix method," in *Proceedings of the IEEE/RSJ International Conference on Intelligent Robots and Systems*, Takamatsu, Japan, Oct. 2000, pp. 786–792.

[34] T. F. Niarisiry, N. Fazenda, and R. Clavel, "Study of the sources of inaccuracy of a 3 DOF flexure hinge-based parallel manipulator," in *Proceedings of the IEEE/RSJ International Conference on Robotics and Automation*, New Oriean, USA, Apr. 2004, pp. 4091–4096.

[35] F. Xu and L. Qu, "Some analytical problems of high performance flexure hinge and micro-motion stage design," in *Proceedings of the IEEE International Conference on Industrial Technology*, Shanghai, China, Dec. 1996, pp. 771–775.

[36] S. Henein, S. Bottinelli, and R. Clavel, "Parallel spring stages with flexures of micrometric cross-sections," in *SPIE Microrobotics and Microsystem Fabrication*, Pittsburgh, USA, 1998, pp. 209–220.

[37] B. P. Trease, Y. M. Moon, and S. Kota, "Design of large-displacement compliant joints," *Journal of Mechanical Design*, vol. 127, no. 4, pp. 788–798, July 2005.

[38] N. Lobontiu and E. Garcia, “Analytical model of displacement amplification and stiffness optimization for a class of flexure-based compliant mechanisms,” *Computers and Structures*, vol. 81, no. 32, p. 2797C2810, Dec. 2003.

[39] T. Arai, J. M. Herve, and T. Tanikawa, “Development of 3 DOF micro finger,” in *Proceedings of the IEEE/RSJ International Conference on Intelligent Robots and Systems*, Osaka, Japan, Nov. 1996, pp. 981–987.

[40] Z. Huang and Q. c. Li, “General methodology for type synthesis of symmetrical lower-mobility parallel manipulators and several novel manipulators,” *International Journal of Robotics Research*, vol. 21, no. 2, pp. 131–145, Feb. 2002.

[41] Y. Fang and L. W. Tsai, “Structure synthesis of a class of 4-DOF and 5-DOF parallel manipulators with identical limb structures,” *International Journal of Robotics Research*, vol. 21, no. 9, pp. 799 – 810, Sept. 2002.

[42] X. Kong and C. M. Gosselin, “Type synthesis of 3-DOF spherical parallel manipulators based on screw theory,” *ASME Journal of Mechanical Design*, vol. 126, no. 1, pp. 101–108, Jan. 2004.

[43] X. Kong and C. M. Gosselin, “Type synthesis of 3T1R 4-DOF parallel manipulators based on screw theory,” *IEEE Transactions on Robotics and Automation*, vol. 20, no. 2, pp. 181–190, Feb. 2004.

[44] Y. Fang and L. W. Tsai, “Structure synthesis of a class of 3-DOF rotational parallel manipulators,” *IEEE Transactions on Robotics and Automation*, vol. 20, no. 1, pp. 117–121, Jan. 2004.

[45] J. M. Herve, “The lie group of rigid body displacements, a fundamental tool for mechanism design,” *Mechanism and Machine Theory*, vol. 34, no. 8, pp. 719–730, Aug. 1991.

[46] J. M. Herve and F. Sparacino, “Structural synthesis of parallel robots generating spatial translation,” in *Proceedings of the IEEE/RSJ International Conference on Robotics and Automation*, Pisa, Italy, Apr. 1991, pp. 808–813.

[47] Q. Li, Z. Huang, and J. M. Herve, "Type synthesis of 3R2T 5-DOF parallel mechanisms using the Lie Group of displacements," *IEEE Transactions on Robotics and Automation*, vol. 20, no. 2, pp. 173–180, Feb. 2004.

[48] P. A. Liu and Q. Li, "Kinematics and dynamics of a general-purpose, parallel, compliant micromanipulator," *International Journal of Multi-Body Dynamics*, vol. 217, pp. 39–45, Apr. 2003.

[49] J. W. Ryu, D. G. Gweon, and K. S. Moon, "Optimal design of a flexure hinge based $XY\phi$ wafer stage," *Precision Engineering*, vol. 21, pp. 18–28, July 1997.

[50] D. Z. Liu, Y. H. Xu, and R. Y. Fei, "Study of an intelligent micro-manipulator," *Journal of Materials Processing Technology*, vol. 139, pp. 77–80, Aug. 2003.

[51] Y. Z. Wang, J. N. Tsay, and C. K. Sung, "Dynamic analysis of a bistable compliant micro-mechanism," in *Proceedings of the 11th World Congress in Mechanism and Machine Science*, Tianjin, China, Apr. 2004, pp. 1400–1404.

[52] A. J. Nielson and L. L. Howell, "Compliant pantographs via the pseudo-rigid-body model," in *Proceedings of the 25th Biennial Mechanisms and Robotics Conference at the 1998 ASME Design Engineering Technical Conferences*, Atlanta, USA, DETC98/MECH-5930.

[53] S. M. Lyon, P. A. Erickson, M. S. Evans, and L. L. Howell, "Prediction of the first modal frequency of compliant mechanisms using the pseudo-rigid-body model," *Journal of Mechanical Design*, vol. 121, pp. 309–313, Feb. 1999.

[54] J. J. Yu, S. S. Bi, and G. H. Zong, "The dynamic characteristic-based optimal design of a fully compliant mechanism," in *Proceedings of the 11th World Congress in Mechanism and Machine Science*, Tianjin, China, Apr. 2004, pp. 1416–1421.

[55] H. Du, M. K. Lim, and K. Liew, "A nonlinear finite element model for dynamics of flexible manipulators," *Mechanism and Machine Theory*, vol. 31, pp. 1109–1119, Nov. 1996.

[56] C. L. Chen and L. W. Chen, "Random response of a rotating composite blade with flexure-torsion coupling effect by the finite element method," *Composite Structures*, vol. 54, pp. 407–415, Dec. 2001.

[57] K. Maute and D. M. Frangopol, "Reliability-based design of MEMS mechanisms by topology optimization," *Computers & Structures*, vol. 81, pp. 813–824, May 2003.

[58] M. Farid and S. A. Lukasie, "Dynamic modeling of spatial manipulators with flexible links and joints," *Computers & Structures*, vol. 75, pp. 419–437, Apr. 2000.

[59] M. Jouaneh and G. E. Ping, "Modeling and control of a micro-positioning tower," *Mechatronics*, vol. 7, pp. 465–478, Aug. 1997.

[60] B. Friedland, *Control System Design*. New York, USA: McGraw-Hill, 1986.

[61] Y. Okazaki, "A micro-positioning tool post using a piezoelectric actuator for diamond turning machines," *Precision Engineering*, vol. 12, pp. 151–156, Dec. 1990.

[62] F. L. Lewis and A. Yesildirek, "Multilayer neural-network robot controller with guaranteed tracking performance," *IEEE Transactions on Neural Networks*, vol. 7, pp. 388 – 399, Mar. 1996.

[63] H. A. Talebi, K. Khorasani, and R. V. Patel, "Neural network based control schemes for flexible-link manipulators: Simulation and experiments," *IEEE Transactions on Neural Networks*, vol. 11, pp. 1357–1377, 2000.

[64] X. P. Cheng and R. V. Patel, "Neural network based tracking control of a flexible macro-micro manipulator system," *Neural Networks*, vol. 16, pp. 271–286, Mar. 2003.

[65] W. Perruquetti, *Sliding Mode Control in Engineering*. New York, USA: M. Dekker, 2002.

[66] S. K. Spurgeon and C. Edwards, *Sliding Mode Control*. London, UK: Taylor and Francis, 1998.

[67] A. Woronko, J. Huang, and Y.Altintas, "Piezoelectric tool actuator for precision machining on conventional CNC turning centers," *Precision Engineering*, vol. 27, pp. 335–345, Oct. 2003.

[68] K. Fite, "Position control of a compliant mechanism based micromanipulator," in *Proceedings of the IEEE International Conference on Robotics and Automation*, Detroit, USA, May 1999, pp. 2122–2127.

[69] K. M. Zhou and J. C. Doyle, *Essentials of Robust Control*. New Jersey, USA: Prentice Hall, 1998.

[70] V. A. Ugronovskii, A. V. Savkin, and I. R. Petersen, *Robust Control Design Using H_∞ Methods*. London, UK: Springer, 1998.

[71] M. Karkoub and K. Tamma, "Modeling and μ-synthesis control of flexible manipulators," *Computers and Structures*, vol. 79, pp. 543–551, Feb. 2001.

[72] I. N. Kar, T. Miyakura, and K. Seto, "Bending and torsional vibration control of a flexible plate structure using H_∞-based robust control law," *IEEE Transactions on Control Systems Technology*, vol. 8, pp. 545–553, May 2000.

[73] H.-C. Yu, Y.-H. Lin, and C.-L. Chu, "Robust modal vibration suppression of a flexible rotor," *Mechanical Systems and Signal Processing*, 2005.

[74] H. W. Park, H. S. Yang, Y. P. Park, and S. H. Kim, "Position and vibration control of a flexible robot manipualtor using hybrid controller," *Robotics and Autonomous Systems*, vol. 28, pp. 31–41, July 1999.

[75] Q. Jin and T. Yang, "Synthesis and analysis of a group of 3-degree-of freedom partially decoupled parallel manipulators," *Journal of Mechanical Design*, vol. 126, pp. 301–306, 2004.

[76] F. Gao, Z. Jin, and H. Zhao, "New kinematics structures for 2-, 3-, 4- and 5-DOF parallel manipulator designs," *Mechanism and Machine Theory*, vol. 37, pp. 1395–1411, 2002.

[77] A. Frisoli, D. Checcacci, F. Salsedo, and M. Berganasco, "Synthesis by screw algebra of translating in-parallel acutated mechanisms," in *International Symposium on Advances in Robot Kinematics*, Piran Portoroz, Slovenia, 2000, pp. 1–8.

[78] T. S. Zhao, J. S. Dai, and Z. Huang, "Geometric analysis of over constraint parallel manipulators with three and four degree of freedom," *JSME International Journal Series C*, vol. 45, pp. 730–740, 2002.

[79] X. Kong and C. M. Gosselin, "Type synthesis of 3-DOF translational parallel manipulators based on screw theory," *Mechanical Design*, vol. 126, pp. 83–92, 2004.

[80] X. Kong and C. M. Gosselin, "A class of 3-DOF translational parallel manipulators with linear input-output equations," in *Proceedings of the Workshop on Fundamental Issues and Future Research Directions for Parallel Mechanisms and Manipualtors*, Quebec, Canada, 2002, pp. 25–32.

[81] Y. Jin, I.-M. Chen, and G. L. Yang, "Mobility and singularity analysis of a selective actuated paralle mechanism," in *15th CISM-IFToMM Symposium on Robot Design, Dynamics and Control*, Montreal, Canada, 2004, pp. 25–32.

[82] Y. Jin, I.-M. Chen, and G. L. Yang, "Structure synthesis and singularity analysis of a parallel manipulator based on selective actuation," in *Proceedings of the IEEE International Conference on Robotics and Automation*, New Orleans, 2004, pp. 4534–4538.

[83] L. W. Tsai, *Robot Analysis: The Mechanics of Serial and Parallel Manipulators*. New York, USA: Wiley & Sons, 1999.

[84] F. Hao and M. McCarthy, "Condition for line-based singularities in spatial platform manipulators," *Journal of Robotics Systems*, vol. 15, pp. 43–55, Jan. 1998.

[85] H. H. Pham, "Selective-actuation micro-positioning systems based on flexure parallel mechanisms," Ph.D. dissertation, Nanyang Technological University, Singapore, 2005.

[86] A. Kareem and K. Gurley, "Damping in structures: Its evaluation and treatment of uncertainty," *Journal of Wind Engineering and Industrial Aerodynamics*, vol. 59, pp. 131–157, 1996.

[87] S. H. Crandall, "The role of damping in vibration theory," *Journal of Sound and Vibration*, vol. 11, pp. 3–18, 1970.

[88] D. G. I. Jones, *Applied Damping Treatments, in Shock and Vibration Handbook*. New York, USA: C. M. Harris, Ed., McGraw-Hill, 1996.

[89] H. H. Pham, H.-C. Yeh, and I.-M. Chen, "Micro-motion selective-actuation xyz flexure parallel mechanism: Design and modeling," *Journal of Micromechatronics*, vol. 3, pp. 51–73, Jan. 2005.

[90] W. Youm, S.-Q. Lee, and K. Park, "Optimal design and control of a voice coil motor driven flexure hinge for AFM actuator," in *Proceedings of the IEEE/ASME International Conference on Advanced Intelligent Mechatronics*, Monterey, USA, July 2005, pp. 325 – 328.

[91] W. Dong, Z. J. Du, and L. N. Sun, "Stiffness influence atlases of a novel flexure hinge-based parallel mechanism with large workspace," in *Proceedings of the IEEE/RSJ International Conference on Intelligent Robots and Systems*, Edmonton, Canada, Aug. 2005, pp. 856 – 861.

[92] S. T. Smith and D. G. Chetwynd, *Foundations of Ultraprecision Mechanism Design*. Switzerland: Gordon & Breach Science, 1992.

[93] L. Charles, *Handbook of Stress and Strength: Design and Material Applications*. London, UK: Macmillan, 1963.

[94] Piezoelectric Stack Actuators from US EuroTek, Inc. [Online]. Available: http://www.globalspec.com/FeaturedProducts/Detail/USEuroTek/Piezoelectric_Stack_Actuators/5649/0?fromSpotlight=1

[95] PI: Introduction to Piezo Motion/ Actuation/ Piezo Mechanic Actuators. [Online]. Available: http://www.physikinstrumente.com/en/products/piezo/index.php?VID=17efZA0TLJj8HHfL

[96] Model Group: Picomotor. [Online]. Available: http://www.newfocus.com/product/modelgroup.cfm?productlineid=6&modelgroupid=1106&app=photonics

[97] Trust Automation: Smart Solutions for Motion Control. [Online]. Available: http://www.trustautomation.com/

[98] ICPDAS. [Online]. Available: http://www.icpdas.com/index.htm

[99] TrustAutomation. [Online]. Available: http://www.trustautomation.com/

[100] Advanced Motion Control Drives-Servo Amplifiers-from Elmo Motion Control. [Online]. Available: http://www.trustautomation.com/

[101] MicroE Systems-Optical Encoders: Linear, Rotary, Incremental, and Absolute Encoders. [Online]. Available: http://www.microesys.com/

[102] J. M. Rieber and F. Allgower, "From H_∞ control to multiobjective control: an overview," *Automatisierungstechnik*, vol. 54(9), pp. 437–449, 2006.